MICRODOSIMETRY FOR A FAST NEUTRON THERAPY BEAM

P.J. BINNS

Thesis presented for the Degree of

DOCTOR OF PHILOSOPHY

Faculty of Medicine

UNIVERSITY OF CAPE TOWN

February 1993

MICRODOSIMETRY FOR A FAST NEUTRON THERAPY BEAM

Peter Justin Binns

National Accelerator Centre, P O Box 72, Faure 7131,
South Africa

Abstract

A thorough microdosimetric investigation of a p(66)/Be(40) neutron therapy beam has been performed with a tissue equivalent proportional counter. The measured lineal energy spectra and derived averages were observed to change for different irradiation conditions pertinent to therapy. Using the parameter y* as an indicator of radiation quality, variations in the potency of the beam were quantified with spatial position and field size in a water phantom, and in the dose build–up region measured in–air. To accommodate these quality changes in the prescription of absorbed dose, the concept of effective dose is invoked to show that if unaccounted for, the quality changes with depth alone would result in a 4% discrepancy between the prescribed and effective dose delivered to the tumour volume. The implications for optimum dose delivery in clinical practice are discussed in terms of these findings.

The timing characteristics of commercial Rossi–type proportional counters operating at low gas pressures were studied in a pulsed neutron beam of nominal energy 63 MeV. The correlation between electron drift and counter dimensions is demonstrated from TOF measurements performed in normal and helix modes. By identifying each registered pulse height event with its own time–of–flight, it is shown that the timing response is masked by amplitude walk derived in the time pick–off. The inherent response of the counter in helix mode (FWHM < 6 ns) is revealed after accounting for time slewing and compares favourably with that of an NE213 liquid scintillator (FWHM = 3.8 ns). Distinct structure associated with the incident energy spectrum is discernible and enables the unambiguous selection of energy deposition events resulting from neutrons of the nominal energy.

Time–correlated microdose spectra were measured with the tissue equivalent and carbon proportional counters in three different quasi–monoenergetic neutron fields with nominal peak energies of 26, 42 and 63 MeV. The time gated spectra are the first reported microdose distributions for truly monoenergetic neutrons in this energy range. The gas–to–wall dose conversion factor for the TE gas filled carbon counter was evaluated from the data so obtained and appeared to increase over the energy range investigated. Subsequently the kerma ratio of carbon to A–150 plastic was determined at each of the three energies and the results found to concur with other published data using different techniques.

Acknowledgements

I would like to express my gratitude to the management and staff of the NAC for their full co–operation during the completion of these investigations. In particular it is a pleasure to acknowledge those colleagues most closely associated with the work.

Dr J H Hough my acting supervisor for all his caring support and tireless assistance.

Prof G H Blekkenhorst (Department of Radiotherapy, Groote Schuur Hospital and University of Cape Town) who served as promoter and volunteered much appreciated advice in preparing this manuscript.

Dr A H Botha and the cyclotron operators for providing the charged particle beams to order.

Dr D T L Jones and Mr A N Schreuder for calibrating and operation of the neutron therapy unit. Mr A N Schreuder is also thanked for helping with the preparation of isodose curves and treatment plans.

Dr B R S Simpson who assisted with running the TOF experiments.

Dr J V Pilcher who wrote the initial data acquisition software needed in the TOF experiments.

Dr S V Förtsch for his general computing advice.

Mrs H J P Heyns for her patience and understanding in typing and retyping this manuscript.

Most importantly my wife, Riekie, for the many sacrifices she has made in sharing with me in both the best and worst of times.

TABLE OF CONTENTS

CHAPTER 1

INTRODUCTION

This thesis describes experimental investigations which provide qualitative and quantitative information relating to fast neutron beams. The dosimetry data described can be applied to neutron therapy beams to ensure that this new modality is used to the best possible advantage in the treatment of malignant disease. Prospective clinical trials are currently underway at Faure, South Africa to determine whether the radiobiological promise offered by fast neutrons can be realised in routine radiotherapy. This necessitates a direct comparison between the clinical effects of neutron and conventional photon treatments. To provide a valid comparison it is essential that the different modalities be similarly optimised in terms of both physical characteristics and accuracy of dosimetry.

History of neutron therapy

The first attempt at treating cancers with accelerator–produced beams of fast neutrons was initiated in 1938, only six years after James Chadwick's identification of the particle. At the time there was no scientific rationale for their use other than it was hoped that relative to their effects on normal tissues, neutrons would be more effective than X or γ–rays in controlling malignant tumour growth. This pioneering work was to end during the Second World War when the Berkeley cyclotron in California was needed for the war effort. Although a few of the patients were still alive some 30 years later, a great deal of harm was done because of excessive normal tissue damage. It was recommended by the principal investigator, Stone, in his Janeway lecture of 1947 (Stone, 1948) that there was no justification for the

continuance of neutron therapy. Not until 1966 was neutron therapy again attempted when the group at Hammersmith Hospital in Britain commenced their studies. In the intervening years a rationale for neutrons had formed on the basis of a number of radiobiological experiments. Appreciation was made of what were then considered the most important factors such as the decrease in the oxygen enhancement ratio (OER) when neutrons are used instead of X–rays, and changes in the relative biological efficiency (RBE) with fractionation and dose level. The Hammersmith group started to achieve encouraging results (Catterall, 1974a and b) which the medical community were all too ready to sieze upon. Based upon the Hammersmith findings, facilities throughout the world launched clinical programmes.

Of necessity these centres were often founded at already existing accelerators not designed for medical purposes and at sites which were not hospital based. The machines themselves produced only low energy ($\bar{E}_n < 10$ MeV) neutrons with poor penetrating power and inflexible beam delivery systems. The importance of these inadequacies were not fully appreciated at the time since it was believed the benefit in local control and long term survival would outweigh the physical disadvantages. Conflicting results started to emerge and serious doubts about the efficacy of fast neutrons compared to conventional modalities were again raised (Duncan *et al.*, 1984 and 1985). Gradually it was realised that the outcome of these early trials was being masked by the use of sub–optimal neutron beams and that a fair and proper comparison was still sought. Neutron therapy centres were needed which were similar in all aspects to isocentric megavoltage electron accelerators producing penetrating low scatter bremsstrahlung photon beams so that all physical differences could be eliminated. In this way the biological properties of the two modalities could be compared unequivocally. Such proposed facilities are technically advanced and costly. This placed reliance upon funds coming from national bodies with a natural reluctance for different countries to operate more than one neutron

therapy centre at a time. The result today is that only a few modern neutron therapy units have been constructed world–wide as shown in Table 1.1 which lists all the currently operational centres with their respective design attributes.

Table 1.1 *Operational neutron therapy facilities (Modified from Wambersie, 1990 and Budach, 1991)*

NEUTRON THERAPY FACILITIES		
Centre	Neutron Reaction	Comments
Europe		
Clatterbridge, UK	p(62)/Be	Isocentric Gantry Variable Collimator
Orleans, France	p(34)/Be	Vertical Beam
Nice, France	p(65)/Be	Vertical Beam Multileaf Collimator
Louvain–la–Neuve, Belgium	p(65)/Be	Vert. + Hor. Beam Multileaf Collimator
Hamburg, Fed.Rep.Germany	(d + T)	Isocentric Gantry
Heidelberg, Fed. Rep. Germany	(d + T)	Isocentric Gantry
Munster, Fed. Rep. Germany	(d + T)	Isocentric Gantry
Essen, Fed. Rep. Germany	d(14)/Be	Isocentric Gantry
USA		
Houston, Texas	p(42)/Be	Isocentric Gantry Variable Collimator
Seattle, Washington	p(50)/Be	Isocentric gantry Multileaf Collimator
Batavia, Illinois	p(66)/Be	Horizontal Beam
Detroit, Michigan	d(50)/Be	Isocentric Gantry Superconducting Cyclo–tron
Asia		
Chiba, Japan	d(30)/Be	Vertical Beam Multileaf Collimator
Tokyo, Japan	d(14)/Be	Horizontal Beam
Seoul, Korea	d(51)/Be	Isocentric Gantry
Riyadh, Saudi Arabia	p(26)/Be	Isocentric Gantry
Africa		
Faure, South Africa	p(66)/Be	Isocentric Gantry Variable Collimator

One such facility complying with all the envisaged requirements is the newly completed National Accelerator Centre (NAC) at Faure. Here a reliable source of high intensity fast neutrons is produced by 66 MeV protons impinging on a semi-thick (non–stopping) beryllium target (Jones *et al.*, 1988). Full isocentric capabilities and a variable collimator ensure flexible beam delivery. The facility has a small hospital attached with radiotherapists participating from two large teaching hospitals situated nearby. Reliable operation of the accelerator ensures the minimum of interruptions to treatment schedules and all physical conditions have been optimized. Under such circumstances direct comparisons between neutrons and photons can earnestly begin.

Variations in beam quality

Many sources of uncertainty exist in radiotherapy procedures (Svensson, 1984) and these need careful consideration so as not to jeopardise the final outcome of a proposed trial. Potentially significant are uncertainties arising in clinical dosimetry and in particular the expression of absorbed dose merits special attention. Ideally the purpose of defining a dose in radiation therapy is to provide a physical quantity that will ensure the desired clinical response in the irradiated tissue. In neutron dosimetry, however, the singular specification of absorbed dose cannot uniquely quantify the therapy beam since radiation of different types or of the same type but of different energies can, for equal absorbed doses, produce different degrees of damage as measured by a specific biological endpoint. In recognition of this phenomenon the term radiation quality is used to empirically quantify the effectiveness of different radiation types. Radiotherapists are acutely aware of the need for greater accuracy in the delivery of absorbed dose to the target volume in order to maximise tumour control with the minimum of complications to normal

tissue. To assist in arriving at the appropriate prescribed dose when treating the same tumour type at different therapy centres, cognizance is taken of differences in beam quality. Collective experience has led to the so–called Clinical Neutron Intercomparison Factor (CNIF) which converts the physical expression of dose into an effective or biological dose which is more relevant to clinical practice (Wambersie and Battermann, 1987). This approach is a necessary pragmatic solution to the very real problem of relating clinical experience in one neutron beam of a particular radiation quality to another so as to optimise treatment regimens. What these factors do not incorporate, however, is any allowance for potential variations in RBE within the patient.

To identify irradiation conditions which might bring about variations in neutron beam quality is very necessary and requires a systematic study. Experimental microdosimetry with tissue equivalent proportional counters (TEPCs) is highly suited for this purpose as it provides physical data that have previously proved a reliable indicator of quality changes between different neutron therapy beams (Menzel, 1984).

Absorbed dose determinations

As long as clinical experience in the treatment of a certain type of tumour remains restricted to a particular centre and to one radiation quality, only the reproducibility in the absorbed dose delivered to the patient during radiotherapy is pertinent. Prospective neutron trials by their very nature are, however, comparisons of different types of radiations usually involving a neutron centre and at least one other referral hospital. In this instance the overall uncertainty in the actual dose absorbed becomes important. For irradiation prescriptions to be equivalent and thus comparable, the

accuracy in the absorbed doses administered for each modality needs to be the same and within certain specified bounds. These limits were quantified in an earlier review (Mijnheer *et al.*, 1987a) and show that the overall uncertainty in the dose estimation for high energy neutrons is approximately 8%, nearly twice that of their conventional counterparts. The single largest contributor to this error derives from the determination of absorbed dose at a reference point in a phantom which is usually deduced from measurements performed with gas filled ionization chambers. To convert the charge produced within these chambers to absorbed dose in tissue requires knowledge of a number of energy dependent parameters. The two with the largest associated uncertainties are W, the mean energy required to create an ion pair in the gas filling and K_T/K_{A150}, the ratio of neutron kerma factors for tissue and A–150 plastic, the material from which the wall of the ionization chamber is made.

The neutron kerma factor for a particular material or element is the kerma per unit neutron fluence and values are needed that extend over the entire energy range now embraced by neutron therapy. Kerma factors require an assessment of kerma which for A–150 plastic can in principle be measured directly. This is not possible for tissue and instead the result has to be synthesised from data for the elemental constituents. Kerma factors can be readily estimated for energies below 20 MeV where microscopic cross section information for the elements of interest are well known (Caswell *et al.*, 1988). At higher energies however, calculations become unreliable due to uncertainties in the nuclear cross section data required as input. As energies increase the problem is exacerbated by the opening up of more reaction channels, the probabilities of which are unknown. The measurement of kerma factors in the energy range 20 – 65 MeV is to be preferred but to date very few results are available (Romero *et al.*, 1985; Schuhmacher *et al.*, 1992; Schrewe *et al.*, 1992a). Experimental determination of kerma for monoenergetic neutrons in this energy range is needed for better estimates of kerma factors.

Low pressure proportional counters have proved very successful in measuring the absorbed dose at the point of maximum build–up from which the kerma can be inferred. Previous measurements have been performed in almost pure monoenergetic neutron fields ($E_n < 20$ MeV) where there were few low energy contaminants. For energies above 20 MeV it is not possible to generate such monochromatic or "clean" beams as neutrons of the nominal energy are usually accompanied by a significant number of lower energy neutrons that result from nuclear excitation and break–up reactions with the target nuclei. Events from these low energy neutrons will be registered by the counter and an additional kerma not associated with neutrons of the nominal energy will be included in the measured response. This spurious kerma can constitute a large proportion of the measured kerma and corrections become necessary.

An alternative approach is to apply time–of–flight (TOF) techniques where event registration is dependent upon the neutron time of arrival at the detector. In this way it is possible to discriminate against the unwanted events due to slower, low energy neutrons. Unfortunately commercial proportional counters typically used in neutron dosimetry exhibit poor timing characteristics, making TOF determinations impractical because of the long flight paths and the intense radiation source that this would require. If the timing characteristics could be improved and reliable single event distributions obtained for neutrons of the nominal energy, then accurate kerma assessments in the energy range 20–65 MeV would be possible.

Present study

This work reports on experimental investigations into changes in radiation quality for a neutron therapy beam. In addition neutron kerma assessments in quasi-monoenergetic beams utilizing the TOF technique are presented. Commercially available low pressure proportional counters are used throughout.

Initially a brief outline of microdosimetry concepts and practice followed by a description of the irradiation facilities available at the National Accelerator Centre are given. In Chapter 4 a thorough survey of a p(66)/Be(40) therapy beam is presented and variations in beam quality identified using conventional microdosimetric techniques. To accommodate these quality changes in the prescription of absorbed dose, the concept of effective dose is invoked and elementary expressions are proposed to assess this quantity. The implications for optimum dose delivery in clinical practice are discussed in a separate chapter by incorporating the noted variations into a four field treatment plan.

Chapter 6 will focus on time–resolved microdosimetry in a high energy quasi–monoenergetic field of nominal neutron energy 63 MeV. Reliable microdose distributions are measured when restricting the size of the sensitive volume of the detector. By applying standard TOF techniques a greatly improved timing response is obtained which compares favourably with that of an NE213 liquid scintillator. Distinct structure associated with the incident energy spectrum is discernible and enables the unambiguous selection of energy deposition events resulting from neutrons of the nominal energy. This method is applied in Chapter 7 to directly assess the total kerma associated with neutrons of a particular energy and additional measurements were performed at two different energies (E_n = 25.5 and 42.0 MeV) with both A–150 plastic and carbon proportional counters. Comparison of monoenergetic microdose spectra facilitated evaluation of $r_{m,g}$, the gas–to–wall dose conversion factor for a TE gas filled carbon counter, and the kerma ratio of carbon to A–150 plastic. The work presented in the thesis is concluded with a summary.

CHAPTER 2

ENERGY DEPOSITION – CONCEPTS AND PRACTICE

Introduction

During neutron irradiation of tissue energy transfers occur via nuclear interactions with nuclei of the constituent atoms (i.e. hydrogen, carbon, nitrogen and oxygen) resulting in various species of charged particles being set in motion. Depending on the energy of the incident neutron, different interactions with varying probabilities take place influencing the character of the produced secondary charged particle spectrum and this determines the concentrations of energy deposition in the medium.

Although containing only 10.2% hydrogen by weight, the preponderance of hydrogen nuclei in tissue (approximate atomic composition $C_5H_{40}O_{18}N$) is significant in the energy transfer process. Elastic scattering off hydrogen is the dominant interaction as the incident particle (neutron) and target nucleus (proton) are of nearly equal mass enabling complete transfer of the incident kinetic energy in a head–on collision. Hydrogen also plays an important role in producing 2.2 MeV γ–rays by the capture of low energy neutrons that have attained thermal equilibrium with the irradiated tissue following successive collisions. This is one of the main sources of γ radiation in patients and phantoms irradiated with neutrons.

At higher neutron energies ($E_n > 10$ MeV) inelastic and non elastic reaction channels become possible and start contributing noticeably to the charged particle spectrum. These processes usually have energy thresholds in the range 4–12 MeV for the elements of interest with the reaction cross sections rising sharply as the threshold

energy is exceeded and levelling off at about 30 MeV. The relative kerma contributions for neutron energies up to 30 MeV are depicted in Figure 2.1 and a summary of the most important neutron interactions in tissue for energies up to approximately 100 MeV are listed in Table 2.1.

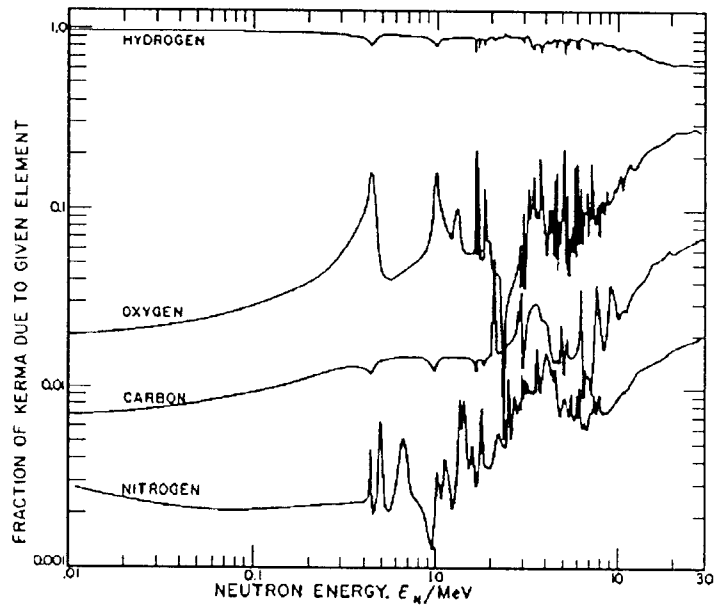

Figure 2.1 *Relative contributions to the total soft tissue kerma from interaction processes with different elements (from ICRU, 1977).*

Irrespective of the nature of these interaction processes, energy transfer to the medium is ultimately expressed in terms of excitation and ionization of the constituent atoms and should not be considered as a single occurrence but rather as a series of random interactions interspersed at different locations within the medium. The amount of energy deposited in tissue is termed the absorbed dose which, as a single parameter, fails to predict biological response. Attempts to comprehend mechanisms that cause the observed biological damage require instead that the initiator of the action be defined over an appropriate scale. Knowledge of the ionization track density and the energy concentrations resulting from the charged particle spectrum become essential because it is these that determine the ability

Table 2.1 *Summary of the most important neutron interactions in tissue for energies up to approximately 100 MeV (ICRU, 1977).*

Element	Interaction
Hydrogen	Elastic scattering Neutron capture
Carbon	Elastic scattering Inelastic scattering (n,n′3α), (n,α) and (n,p) reactions
Nitrogen	Elastic scattering Inelastic scattering (n,p), (n,d), (n,t), (n,α), (n,2α) and (n,2n) reactions
Oxygen	Elastic scattering Inelastic scattering (n,α) and (n,p) reactions

of a particular radiation to inflict irreparable cell damage. Microdosimetry is a study of the character of these energy distributions in volumes approaching the size of a mammalian cell.

Absorbed dose

The absorbed dose is defined as

$$D = \frac{\Delta E}{\Delta m} \qquad (Gy)$$

where ΔE is the mean energy imparted (in Joules) by ionizing radiation to matter in a volume element of mass Δm (kilograms). The singular specification of absorbed dose does not however, uniquely quantify the effectiveness of the radiation as measured by a specific biological end–point. Whilst the observed biological damage

represents the aggregate response of the many cells that comprise the irradiated sample, the random nature of the energy deposition process creates a non–uniform distribution of energies imparted to the cells. As the response of a particular cell is dependent upon the energy it actually receives, it is this quantity and not the macroscopic averaged absorbed dose for the sample that is pertinent for describing the effectiveness of the radiation.

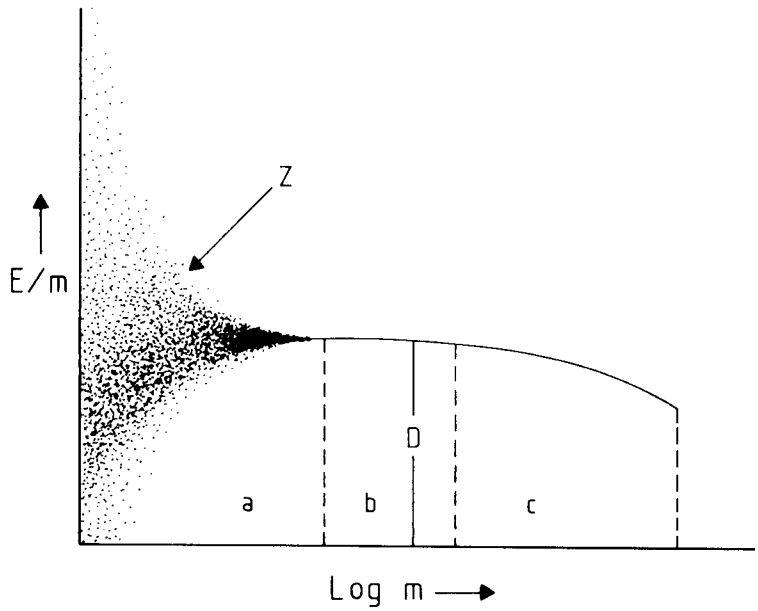

Figure 2.2 *Energy density as a function of varying mass (from Rossi, 1968).*

This is best illustrated by considering for a given exposure variations in the ratio of E/m for an energy deposition E as the mass m of material confined to a finite volume is varied (Figure 2.2). The diagram may be divided into three regions of m, where the highest value of log m is associated with the recognized density of the material.

In region c the fluence of secondary charged particles is non uniform and attenuation of the indirectly ionizing radiation is observed, i.e. E/m diminishes as m approaches its maximum value. In region b the particle fluence remains essentially uniform and conditions for Bragg–Gray cavity theory are satisfied, allowing for the macroscopic measurement of the absorbed dose D. By operating ionization chambers at ambient

gas pressures, the number of interactions is large enough to ensure that a statistically accurate value for the absorbed dose is estimated. If m is further reduced, the deposition of energy will depend on whether or not interactions occur with the material now sparsely dispersed throughout the volume (region a). Either no energy transfer occurs or a large amount of energy is transferred in a specific interaction or event, in which instance the ratio of E/m is termed the specific energy Z. Here energy is absorbed in an identifiable single event and the size of this event may vary over several orders of magnitude.

A radiation source is characterized by the unique frequency distribution of event sizes, which when summed together give the absorbed dose. Differences in the effectiveness or quality of various radiation types, that is differences in the biological response to equal absorbed doses, relate to differences in the frequency and magnitude of local energy depositions that occur within the sensitive tissue volumes. As the discrete or quantised nature of the energy depositon processes only becomes apparent at microscopic mass levels, this necessitates that the resulting energy transfers be physically assessed on a scale of at least similar dimensions.

Linear energy transfer

The first attempts at specifying radiation quality in terms of a physical parameter led to the definition of *linear energy transfer* (LET). The LET or collision stopping power is defined as $L = dE/dx$ where dE is the mean energy lost by a charged particle in collisions along an element dx of its trajectory. The LET takes into account all possible physical interaction processes and is applicable to all charged particles. The value of L depends upon the energy of the particle as shown in Figure

2.3. In the case of a mixed radiation field where there are particles of different charge, velocity and mass, a large range of L will be present.

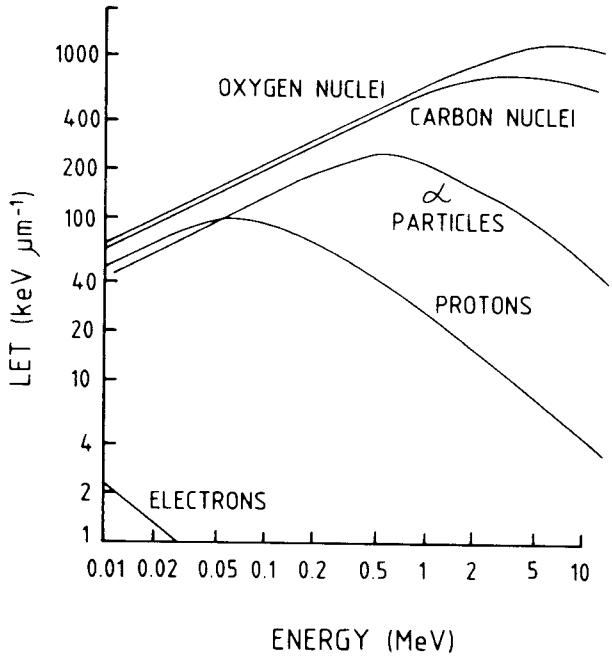

Figure 2.3 *Linear energy transfer for various secondary charged particles as a function of their energy (reproduced from Bewley, 1989).*

To characterise a radiation field possessing a distribution of LETs by a single parameter requires that a mean value be determined. The *frequency average* LET ($\bar{L}_F$) and the *absorbed dose average* LET ($\bar{L}_D$) can respectively be calculated as

$$\bar{L}_F = \int_0^\infty L\, f(L)\, dL \Big/ \int_0^\infty f(L)\, dL \qquad (\text{keV } \mu\text{m}^{-1})$$

and $$\bar{L}_D = \int_0^\infty L^2\, f(L)\, dL \Big/ \int_0^\infty L\, f(L)\, dL \qquad (\text{keV } \mu\text{m}^{-1})$$

where f(L) is the fraction of track lengths with LET between L and L + dL. These expectation values for the energy loss along linear tracks have been applied and proved adequate for selected phenomena, but were an over simplification of the fundamental processes as they did not recognise

(i) the finite range of charged particles

(ii) lateral extension of the tracks (energy dissipation by δ rays)

and (iii) energy loss straggling.

In the case of protons for example, there are a wide range of site sizes for which the above are of little consequence and the LET concept can be applied without reservation (Kellerer and Chmelevsky, 1975). These omissions cannot be ignored though for electrons where LET fails to properly describe the relevant microscopic properties of interest.

LET and RBE

In spite of these acknowledged shortcomings LET has been widely used as a physical description of radiation quality in biological systems. The relationship between the relative biological effectiveness (RBE) of a radiation source and the LET parameters that describe the radiation is, however, more complex than that of simple proportionality to either the frequency or dose averages. Experiments performed with tissue cultured mammalian cells yielded the non–linear LET vs. RBE relationship depicted in Figure 2.4 (Barendsen *et al.*, 1963). It is evident from this data that the application of averaged LET values could lead to misguided conclusions. If for example, the LET distribution for a particular radiation type possesses sizable components above and below the peak shown in the curve, a lower RBE will be observed than that for a similarly centered narrow peaked distribution having the same average LET.

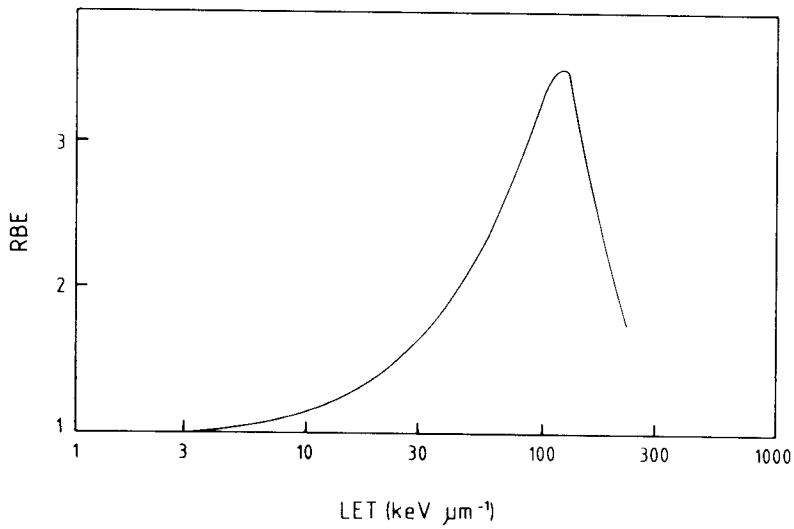

Figure 2.4 *RBE for 20% inactivation of cells in tissue culture as a function of LET (reproduced from Barendsen et al., 1963)*

In endeavouring to measure LET with low pressure proportional counters (Rossi and Rosenzweig, 1955a) it was realized the information from these detectors was superior to that originally sought, as it was the actual energy concentrations along the particle track rather than the finite energy loss of the particle that determined the noted biological effect. This led to new concepts and techniques which related energy absorption in low pressure proportional counters to energy depositions in subcellular volumes of micrometer dimensions.

Lineal energy

The concept of lineal energy measured for single events within the volume of a low pressure proportional counter provided a more relevant description of the energy imparted to matter. The *lineal energy* y is defined (ICRU, 1980) as

$$y = \frac{\epsilon}{\bar{\ell}} \qquad (\text{keV } \mu\text{m}^{-1})$$

where ϵ is the energy imparted by a single energy–deposition event within the

volume and $\bar{\ell}$ the mean chord length in that volume. The mean chord length is a geometrical parameter equivalent to the mean length of randomly orientated chords in the volume. For a convex body

$$\bar{\ell} = \frac{4V}{S}$$

where V is the volume and S the surface area of the body. In the case of an isotropically irradiated sphere of diameter d the mean chord length is $^2/_3$ d.

By definition lineal energy offers a method of evaluating the stochastic nature of multiple energy depositions. Two types of distributions account for the stochastic fluctuation in y; the probability distribution (or the *normalised frequency distribution*) which is the distribution of the fraction of the total number of events having event sizes between y and y+dy and is plotted as a function of y, and the normalised *absorbed dose distribution* which is the fraction of the total energy (dose) that is deposited for event sizes between y and y+dy, plotted against y. Both distributions have expectation values that are direct analogues to the LET averages given earlier. The *frequency mean* $\bar{y}_F$ reflects the average event size and under some restrictive conditions the *dose mean* $\bar{y}_D$ provides a qualitative indication of biological effectiveness. The ratio $\bar{y}_D/\bar{y}_F$ is a measure of the width or variance of the frequency distributions. These parameters refer only to energy depositions within a simulated site size of cellular dimensions and cannot be considered an adequate fundamental description of radiation quality. This is because they make no allowance for the other cells in the irradiated sample that receive no energy depositions at all but which also contribute to the aggregate biological response.

In recognition of the decrease in RBE observed for particles having an LET of more than about 100 keVμm^{-1}, an explanation involving excess energy concentrations in small site sizes was proposed. The assumption was made that on occasions of high local energy concentrations, more energy is deposited than required to produce the desired cellular effect and a saturation level is reached above which the deposition of additional energy produces no greater effect, and energy is consequently wasted. To accommodate this phenomenon the absorbed dose distribution is modified by an empirically derived weighting factor to provide the *saturation corrected dose mean lineal energy* y^* given by

$$y^* = \int_0^\infty y\, d_{sat}(y)\, dy \qquad (\text{keV } \mu m^{-1})$$

with

$$d_{sat}(y) = \frac{y_0^2}{y^2}\left[1 - \exp - (y/y_0)^2\right] d(y)$$

where y_0 is a biologically determined saturation parameter (Kellerer and Rossi, 1972).

Although lineal energy distributions and averages provide quantitative data for a specific radiation field, a fundamental understanding of interaction with living cells is limited because there is no explicit relationship between the derived quantities and biological effect. Whilst there does not exist as yet any proven physical parameter of radiation that correlates closely and fundamentally with biological effect, the measurement of lineal energy distributions does have practical applications in the assessment of radiation quality. This has been demonstrated in the domains of radiation protection and therapy through an approximate empirical correlation with biological effectiveness over limited regions of practical interest.

Volume simulation

Experimental microdosimetry using spherical proportional counters provides a means of assessing lineal energy probability distributions for simulated site sizes comparable to those of a mammalian cell i.e. 1–2 μm. These detectors have inherent signal amplification properties that enable the measurement of the full range of event sizes produced in the simulated volume and are sensitive enough to ensure good statistical accuracy for even small energy depositions. Technically it is not feasible to construct an energy spectrometer having dimensions of about 1 μm in condensed matter and instead a comparatively large volume detector is filled with a small mass of gas.

To achieve the quantitative simulation of energy depositions in a small tissue volume, the energy loss experienced by a charged particle of a specific type (i.e. protons) and energy passing through the counter volume must be the same as that for a corresponding trajectory through the tissue volume, i.e.

$$S_g \rho_g x_g = S_t \rho_t x_t$$

where S is the mass stopping power, ρ the density and x the path length, with subscripts g for the gas and t for tissue. If true tissue equivalence is achieved for the gas, then the mass stopping powers for gas and tissue are considered equal and the microdosimetric quantities measured in the gas–filled counter will be scaled with respect to those occurring in the biological structure by the inverse ratio of their respective densities.

Qualitatively the single event spectra measured with these counters are not identical to those in tissue due to differences in the elemental composition of A–150 plastic and

tissue and spurious phenomena termed wall effects (ICRU, 1983). The higher density of the counter walls can cause an increase in energy deposition within the gas cavity due to the inclusion of events which would otherwise occur in separate volumes in a medium of uniform density. The distortions introduced by wall effects are found to vary with the type and energy of the radiation (Kellerer, 1971).

Principles of counter operation

The geometry of a typical counter is either a spherical or cylindrical gas filled cavity with a sensitive volume that is delineated by a solid wall. A central wire electrically isolated from the wall material runs along the counter diameter or central axis. The counter wall is usually grounded. In traversing the cavity, the secondary charged particles ejected from the wall undergo energy losses through excitation and ionization of the gas filling and ion pairs are formed. If a voltage is applied between the conducting wall of the counter and the centre wire, the ion pairs are subjected to electric forces and a voltage change is induced at the centre wire or anode where the electrons are collected. The amount of charge collected is then a measure of the number of ion pairs produced in the counter gas and can be equated with the energy deposited in the cavity volume, provided the mean energy required to produce a single ion pair in the gas is known. This quantity, referred to as the W–value, is unique to the gas mixture and varies with the type and energy of the ionizing particle.

The size of the pulse appearing at the centre wire depends on the applied voltage. If the voltage is high enough so that each primary ion acquires enough energy to

produce second and higher generation ions through collisions with the gas molecules (Townsend avalanche), an amplified pulse proportional to the deposited energy is produced. When an ionization chamber operates in this mode it is called a proportional counter (Knoll, 1979). The amplification or gas gain in a proportional counter is governed principally by the electric field strength across the sensitive volume and the pressure of the gas filling. In the simple case of a cylindrical counter the field strength at a radius r is given by

$$E = \frac{V}{r \; \ell n \; (r_2/r_1)} \qquad (Vm^{-1})$$

where V is the applied voltage and r_1 and r_2 are the radii of the centre wire and cylindrical cathode respectively. Usually gas amplification is restricted to a very small region close to the collecting wire and under these conditions the gas multiplication is nearly independent of the position from where the primary ion was produced. At very low gas pressures this multiplication region can extend further into the counter volume and the gain will depend upon the position of the event in the counter, thereby destroying the proportionality between energy deposited and pulse height. This places a lower limit (approximately 0.3 μm) on the possible site sizes which may be simulated with conventionally sized counters.

Rossi–type proportional counter

All measurements were performed with commercial "LET–1/2" proportional counters manufactured by Far West Technology (Goleta, USA). The counter design (Oliver *et al.*, 1972) is based upon that of Rossi and Rosenzweig (1955a and b). The counter has a spherical shell of inner diameter 12.7 mm with wall thickness of either 1.3 mm or

2.5 mm. Various wall materials are available but for this work the choice was restricted to A–150 tissue equivalent (TE) plastic (Smathers *et al.*, 1977) and carbon (graphite). These are referred to as tissue equivalent (TEPC) and carbon (CPC) proportional counters respectively. The principle of operation is the same irrespective of wall material and the electrical characteristics of the two counters were found to be very similar.

When operating these counters conventionally the electrically conducting wall (cathode) was kept at ground potential whilst a positive voltage was applied to the centre wire (anode) stretching across the diameter of the spherical cavity. The spherical shape of the sensitive volume leads to a distortion of the electric field towards the ends of the anode (end effects). To overcome this asymmetry an ancillary electrode in the form of a helix is positioned concentrically around the anode. By applying an intermediate voltage to the helix with respect to the anode a cylindrically uniform field is produced along the entire length of the anode. A divider network of resistors installed in the connector box of the detector maintains the bias to the helix at 20% of that applied to the anode. The counter is encapsulated in a vacuum tight aluminium shell (0.0178 cm thick) at the end of an aluminium stem on which electrical connectors and a vacuum fitting for gas filling are mounted. This design enabled operation of the counter whilst immersed in a water phantom without the need for a continuous gas flow system.

Counting gas

The detectors were filled with a propane–based TE gas mixture the composition of which is given in Table 2.2. A propane rather than methane–based TE mixture was

chosen because of better gas gain characteristics (Srdoc, 1970). The larger signal to noise ratio obtained with the propane mixture is particularly advantageous in accelerator environments where electronic interference from the generated RF and

Table 2.2 *Elemental composition of propane–based tissue equivalent gas (Srdoc, 1970).*

Gas Mixture (partial pressures)	55.0 % C_3H_8, 39.6% CO_2, 5.4% N_2
Composition (% weight)	10.3% H, 56.9% C, 3.5% N, 29.2% O
Density (at 20° C, 100 kPa)	1.798 $kg.m^{-3}$
Average atomic weight	$\bar{A}$ = 5.871
Average atomic number	$\bar{Z}$ = 3.235

the many power supplies located along the beam line can distort the radiation related spectrum measured by the counters. A 2 μm diameter sphere of unit density tissue was simulated by filling the counters to a pressure of 8.7 kPa. After filling, gas gain instabilities were observed for a number of hours and as a consequence the counters were always charged at least 24 hours prior to use.

The pressure of the filling determined the maximum applied bias and the onset of electrical discharge or arcing inside the counter was monitored by viewing the output signals on an oscilloscope. A positive potential of 600V provided sufficient gas amplification to register small event sizes that would otherwise be lost in the general electronic noise of the system and measured lineal energy spectra extended down to approximately 0.2 keV μm^{-1}.

Electronics

The range of event sizes resulting from exposure to a fast neutron field varies over five orders of magnitude and it is necessary to record the magnitude and frequency of all such events. To ensure suitable pulse height resolution, the counter output pulses were amplified utilizing standard nuclear instrumentation modules (NIM electronics). A schematic diagram of the experimental set up is shown in Figure 2.5. The output signal from the proportional counter is fed into a charge sensitive pre–amplifier where an integrated output voltage proportional to the accumulated charge is produced. The nominal voltage gain was set such that a charge of 0.7 pC would produce a 1 volt pulse. Thereafter the pulse is shaped and amplified further by a linear spectroscopy amplifier which produces unipolar and bipolar signals with preselected timing characteristics. Amplitudes ranged from 0 to 10 V and a time constant of 2 μs was chosen to minimise pulse pile–up. This also provided adequate sampling time for the analogue to digital converter (ADC) which required a minimum pulse width of 0.5 μs. The pole/zero trim on the amplifier was set to minimize over– or under-shooting for the unipolar output pulse.

To accommodate the large range of pulse heights, three linear amplifiers with relative gain settings of X10, X100 and X1000 were employed. These settings were adjusted using a reference pulser as source for the test input to the pre–amplifier. The simultaneous acquisition of all three pulse height spectra ensured that each segment was recorded under identical beam conditions and minimized the beam time required for a measurement. Each amplifier output (unipolar) was fed to a Wilkinson type ADC (100 MHz clock rate) operating in the pulse height analysis (PHA) mode. The ADC gain was set to provide a resolution of 1024 channels of equal width for the 0 –

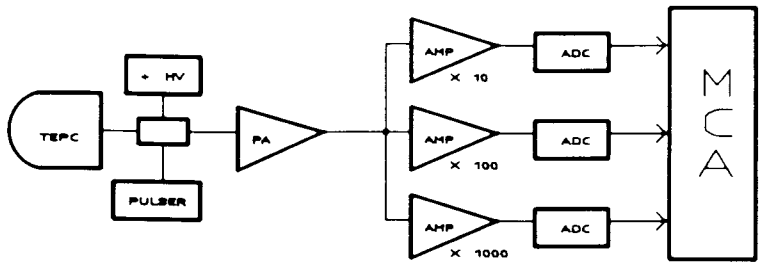

Figure 2.5 *Block diagram of the electronic system used for pulse processing and data acquisition. Index: ADC = analogue to digital converter, AMP = linear spectroscopy amplifier; HV = high voltage supply, MCA = multichannel analyser; PA = preamplifier; PULSER = reference pulse generator; TEPC = tissue equivalent proportional counter.*

10 V range of input pulses. The zero intercept of the ADC was set using a precision pulser. During irradiation the count rates of the amplifier outputs were monitored by a scaler and the beam intensity adjusted so that rates did not exceed 3000 cps in the high gain amplifier. Each ADC recorded its own live and true times in channels zero and one respectively. The difference between the two was due to the processing or dead time of the ADC for a particular count rate. Dead times were negligible for both the low and medium gains but would typically be 2% and at worst 5% for the high gain stage. The ADCs were equipped with an adjustable lower level discriminator which was set at approximately 0.1V for each stage. The ADCs were fed through a router module to a multichannel analyser (MCA) where individual pulse height spectra were displayed. Control of the data acquisition process was through the MCA which could start or stop the three ADCs simultaneously. Upon completion of a measurement the pulse height data for each amplification stage were transferred from the MCA to a microcomputer via the standard RS232 interface and serial ports where the data were stored on disc for subsequent analysis.

Pulse height calibration

All counters were equipped with internally mounted ^{244}Cm sources to provide pulse height calibration in terms of a specific energy loss. Whilst use of the α–source gave a good constancy check on the performance (gas gain) of the counter during a series of measurements, calibration of the data was performed utilizing the less error prone proton edge method (Waker, 1985; Pihet *et al.*, 1992a). When simulating a 2 μm diameter sphere of unit density tissue, a value of 180 keV was calculated for the maximum energy loss suffered by a proton crossing the diameter of the cavity. Here the stopping power data of Andersen and Ziegler (1977) were used. An uncertainty of between 5 and 10% is associated with this energy loss but more recent findings estimate uncertainties of only about 2% (Waibel and Willems, 1987). A position on the lineal energy scale of 135 keV μm^{-1} for the bottom of the proton edge was obtained by dividing the maximum energy loss by the mean chord length for the simulated spherical cavity ($\bar{\ell} = 4/3$ μm). The finite width of each lineal energy bin was also observed to contribute to the overall uncertainty when positioning the proton edge. This source of error was quantified by moving the edge of a spectrum by one lineal energy bin which induced a change of 5.6% in the evaluated absorbed dose.

Data reduction

Data reduction was performed on an IBM compatible microcomputer following the conclusion of a measurement which included performing a background run by collecting data in the high gain amplifier with the beam off. The background run was scaled to the beam measurement by the ratio of the respective live times and data subtracted prior to matching the subspectra. Composite frequency and dose

distributions of the three measured subspectra were then normalised to unit area. To enhance the clarity of data display a logarithmic event size scale was needed. In converting the experimental spectrum from a linear to logarithmic scale it was important to preserve proportionality between the area under the curve delineated by two values of event size and the fraction of the number of events (or dose delivered) in that event size interval. This was maintained by constructing plots of yf(y) and yd(y) [= $y^2f(y)$], both as a function of y after normalization as follows

$$\int_{y_1}^{y_2} f(y)\, dy = \int_{y_1}^{y_2} y\, f(y) d\, \ell n\, y = 1$$

and similarly

$$\int_{y_1}^{y_2} d(y)\, dy = \int_{y_1}^{y_2} yd(y)\, d\, \ell n\, y = 1$$

To produce these plots the raw pulse height data from each of the subspectra were rebinned into a logarithmic lineal energy scale of 40 equal intervals per decade. The amplifier gains were set to ensure regions of overlap between adjacent subspectra. Each higher gain subspectra was joined to its lower gain neighbour with a normalisation factor determined from the ratio of the data in the corresponding overlap region. Moving bin by bin through the overlap region an average ratio was calculated for ten consecutive bins at a time. The average which agreed best with the ratio of the live times for the two subspectra being joined, determined the matching region and the normalization factor. The normalization factor seldom differed by more than 2% from the ratio of the live times. Low gain data below and high gain data above the matching interval were discarded.

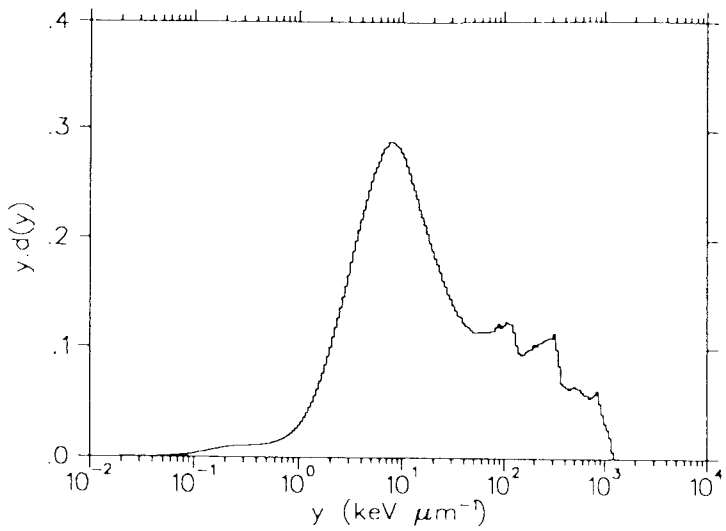

Figure 2.6 *Measured dose distribution represented as yd(y) versus log y. The data was obtained in the p(66)/Be(40) neutron beam at the NAC therapy facility*

Figure 2.6 shows a typical plot of a dose distribution measured in the NAC therapy beam. The event size scale was calibrated by positioning the bottom of the proton edge at 135 keVμm^{-1}. This value is an invariant with neutron energy and changes only with the volume simulated by the counter.

Employing the expressions for the averaged parameters defined in ICRU, (1983) the frequency mean $\bar{y}_F$, the dose mean $\bar{y}_D$ and the dose mean corrected for saturation y* values were calculated for the binned data as follows

$$\bar{y}_F = \sum_{i=1}^{240} y_i \, f(y_i) \Big/ \sum_{i=1}^{240} f(y_i) \qquad (\text{keV}\mu\text{m}^{-1})$$

$$\bar{y}_D = \sum_{i=1}^{240} y_i^2 \, f(y_i) \Big/ \sum_{i=1}^{240} y_i \, f(y_i) \qquad (\text{keV}\mu\text{m}^{-1})$$

and

$$y^* = \sum_{i=1}^{240} y_o^2 \left[1 - e^{-(y_i / y_o)^2}\right] f(y_i) \Big/ \sum_{i=1}^{240} y_i \, f(y_i) \qquad (\text{keV}\mu\text{m}^{-1})$$

where i is the bin identification for a particular lineal energy and y_0 = 123.75 keVμm^{-1} (Kellerer and Rossi,1972).

Evaluation of absorbed dose

The determination of absorbed dose by means of a low pressure proportional counter is based upon Bragg–Gray cavity theory and requires that

1. the presence of the gas cavity does not perturb the charged particle fluence and that the charged particles lose only a small fraction of their energy in traversing the cavity

and for a wall material and gas filling of different compositions

2. the absorbed dose in the cavity is deposited entirely by charged particles traversing the cavity, i.e. crossers (ICRU, 1983).

Under these conditions the absorbed dose in the wall D_m is related to the absorbed dose in the gas D_g by

$$D_m = \frac{\overline{W}_N}{W_C} \cdot r_{m,g} \cdot D_g$$

where $r_{m,g}$ is the gas–to–wall dose conversion factor and $\overline{W}_N/W_C$ the average energy required to create an ion pair in the gas by neutron induced secondaries relative to that for the calibrating radiation. If secondary charged particle equilibrium is established in the wall then D_m is also equivalent to the total kerma. The absorbed dose to the gas D_g is evaluated by summation of the measured frequency distribution

$$D_g = \frac{C}{m}\,\bar{\ell}\sum_{i=1}^{240} y_i\, f(y_i) \qquad (Gy)$$

where m is the mass of gas in the counter cavity, C the energy conversion factor (keV to Joules) and $\bar{\ell}$ (μm) the mean chord length.

The parameter $r_{m,g}$ is the ratio of the average mass collision stopping powers for the wall and gas. In the case of a homogeneous detector with walls and gas of the same atomic composition, density corrections to the stopping powers are neglected and a value of $r_{m,g} = 1.00 \pm 0.02$ is assumed (ICRU, 1989). When the walls and gas differ in composition however, $r_{m,g}$ has to be evaluated. In a high energy neutron beam (E_n>20 MeV) this is problematic as the secondary charged particle spectra produced in the wall material are not well known. The TEPC with TE gas filling used in these studies was considered a homogeneous detector (i.e. $r_{m,g} = 1$) and the CPC/TE gas mixture an inhomogeneous system for which $r_{m,g}$ values were empirically determined.

The W–value or energy required to produce an ion pair in the gas filling varies between the different species of charged particles produced by the neutron interactions in the wall material, tending to increase with decreasing particle energy (velocity) as more energy is expended in non–ionizing processes. This has been demonstrated in propane–based TE gas for different ions in the energy range 25–375 keV (Posny *et al.*, 1987). Recent estimates for propane based TE gas show no significant differences in the W–values for 100 keV protons (i.e. those used in the proton edge calibration method) and 700 keV alpha particles (Pihet *et al.*, 1992a) and a value of unity was adopted for $\overline{W}_N/W_C$. A different W–value was considered

necessary in the evaluation of the photon dose fraction where the secondary charged particle spectrum only contains electrons. A ratio for $W_e/\overline{W}_N$ of 0.94 was adopted (Goodman and Coyne, 1980).

Uncertainties of measurements

When using low pressure proportional counters, uncertainties in the measured absorbed dose to the counter wall are attributed largely to the conversion of ionization yield to an energy deposition spectrum and in calibration of the pulse height data. Converting the ionization yield measurements to energy deposition spectra also necessitates approximations as unique W–values cannot be associated with each pulse height because different secondaries with different W–values can give rise to events of identical pulse heights. Counting statistics are another source of uncertainty but were minimised by ensuring that the counters received a dose of between 1 and 5 cGy during an irradiation. The principal sources of uncertainty are itemized in Table 2.3 and together totalled 8.2% when added in quadrature and expressed as one standard deviation. This estimate is believed realistic and compares with the 7.2% uncertainty quoted for a CPC measurement in a 42 MeV neutron field after a thorough error analysis. (Schrewe *et al.*, 1992a).

In quoting values for the average microdosimetric parameters overall uncertainties of 10% and 6% have been associated with $\bar{y}_F$ and $\bar{y}_D$ respectively (Waker, 1985). However, systematic errors such as calibration uncertainties are less important in studies of comparative changes as utilized in this work and instead the statistical

Table 2.3 *Principal sources of uncertainty in the determination of absorbed dose to the counter wall.*

Source	Reference	Error %
Proton edge position	(This work)	5.6
Stopping power data for protons	(Andersen and Ziegler, 1977)	5
Constant W–value approximation	(Pihet *et al.*, 1922a)	3
Counting statistics	(Menzel *et al.*, 1984)	<1

uncertainty for a single measurement is more pertinent. Experience of repeated measurements over an extended period realised standard deviations better than 6%, 2% and 1% respectively for $\bar{y}_F$, $\bar{y}_D$ and y^* (Binns and Hough, 1988).

Spectral characteristics

Dose distributions in lineal energy measured in neutron fields exhibit features that can be ascribed to identifiable physical processes. Figure 2.7 shows a dose distribution measured in a d(14) + Be neutron therapy beam with a Rossi–type proportional counter simulating a unit density sphere of tissue 2 μm in diameter (Fidorra *et al.*, 1980). Separate contributions to the total absorbed dose from different components making up the secondary charged particle spectrum can be recognised. Prominent is the proton recoil peak centered near 10 keV μm^{-1} and the slow recoil protons at approximately 70 keV μm^{-1}. The right hand edge of the proton peak corresponds to the maximum energy loss that a proton can undergo inside the counter. Energy depositions by α–particles and heavy recoil nuclei are evident above the proton edge whilst events extending down to 0.1 keV μm^{-1} are attributed to recoil electrons following Compton scattering of photons.

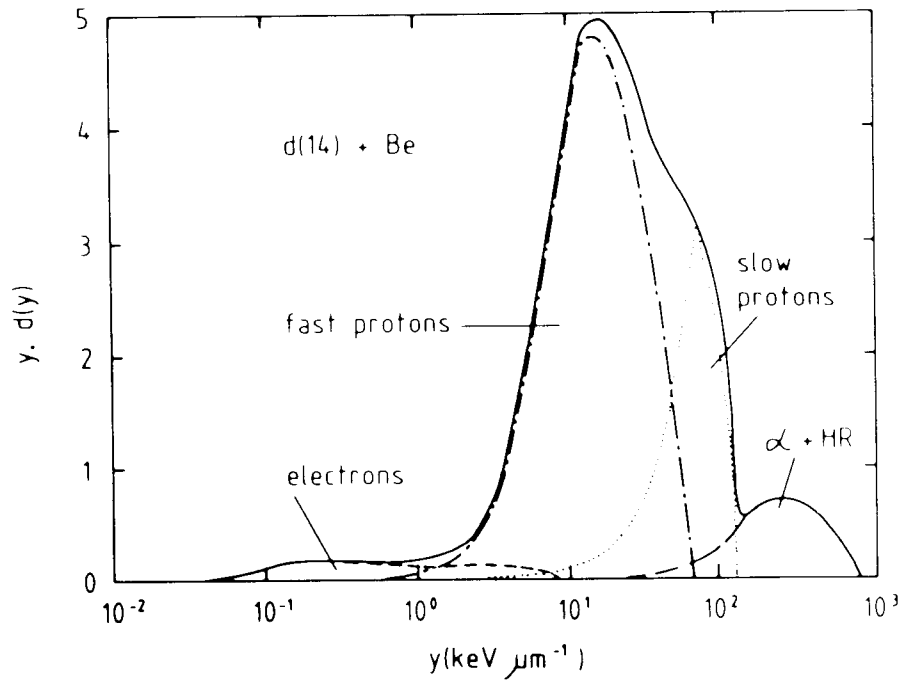

Figure 2.7 *Dose distribution measured in a d(14)+Be neutron therapy beam separated into the four radiation components: gamma rays (fast electrons), fast recoil protons, slow recoil protons, alpha and heavier recoil ions (reproduced from Fidorra et al., 1980).*

Photon dose evaluation

The presence of photons in a neutron therapy beam is unavoidable as they are produced at the neutron source and in the collimator as well as within the patient. The amount of contamination is expressed as the photon dose fraction (PDF) and is given by the quotient of the photon dose by the total dose measured at a particular point. The PDF is usually provided as additional information in therapy protocols. Assessment of the PDF with a TEPC is relatively straightforward and is considered more reliable than with the twin ionization chamber method (Weaver *et al.*, 1977) where the neutron sensitivity of the supposedly neutron insensitive detector continues to be a limitation for accurate evaluations.

The TEPC technique utilizes the fact that the electrons set in motion by photons

have lower LETs and hence smaller y values than the proton and heavy recoils produced by neutron interactions. Although the exact nature of the photon energy spectrum for the p(66)/Be(40) therapy beam is unknown, measurements in a hydrogenous phantom can be expected to comprise largely of photons with energies 2.2 MeV resulting from neutron capture reactions (Menzel and Waker, 1976). Consequently the dose distribution for a pure ^{24}Na source (E_γ=2.75 MeV) was considered representative of the photon component and a single event spectra for this source was measured for all event sizes greater than 0.1 keVμm^{-1}. This lower threshold was achieved by performing the measurement in a laboratory distant to the therapy vault where the electronic noise level was much reduced. Below the measurement threshold the frequency distribution was extended to lower event sizes by applying a zero slope extrapolation to the data (Stinchomb *et al.*, 1980). All dose distributions obtained in neutron fields were extended to lineal energies below 0.25 keVμm^{-1} by fitting the ^{24}Na spectrum to the measured single event spectra. Using normalised dose distributions the pure photon spectrum was scaled to that of the neutron measurement in the region of 0.25 – 0.4 keVμm^{-1}. This interval was chosen to minimise errors due to the intrusion of the fast proton tail observed in high energy neutron beams. The scaling factor gives the ratio of the photon to total dose that is measured with the TEPC assuming $W_N = W_e$. The factor was then multiplied by the ratio of $W_e/\overline{W}_N$ (i.e. 0.94) to yield the PDF measured in the mixed n/γ radiation field.

CHAPTER 3

NATIONAL ACCELERATOR CENTRE

Introduction

The National Accelerator Centre (NAC) at Faure, South Africa, is a multi-disciplinary research institute established in 1977. Experimental facilities and particle beams are provided for radiotherapy, the routine production of medical radioisotopes, and nuclear physics research. A layout of the main facility is shown in Figure 3.1. Two small solid–pole cyclotrons serve as injectors or pre–accelerators for the much larger separated–sector cyclotron (SSC) (Botha *et al.*, 1991). The first injector (SPC1) is equipped with an internal ion source to produce the intense beams of light ions necessary for particle radiotherapy and radioisotope production (Du Toit *et al.*, 1987). The second injector (SPC2) is still under construction and will provide heavy ion and polarised light ion beams. SPC1 can accelerate protons up to an energy of 8 MeV for injection into the first orbit of the SSC. The SSC is a variable energy machine designed to accelerate protons to a maximum energy of 200 MeV. Once the acceleration process is complete, particles having reached the required energy are ready for extraction, and are then transported along the various beam lines to a designated irradiation area.

Beam time for neutron therapy is available for three working days a week, Tuesdays, Wednesdays and Thursdays. Patients are accrued countrywide by referral to the radiotherapy departments of either Groote Schuur or Tygerberg which are the main teaching hospitals for the area. NAC is conveniently situated between these two hospitals, and patients are either admitted daily as out–patients or accommodated in

the 30 bed hospital on–site. The most recent figures available show that 419 patients have been treated up to the end of 1992.

A brief description of the therapy and other irradiation facilities used in this work follows.

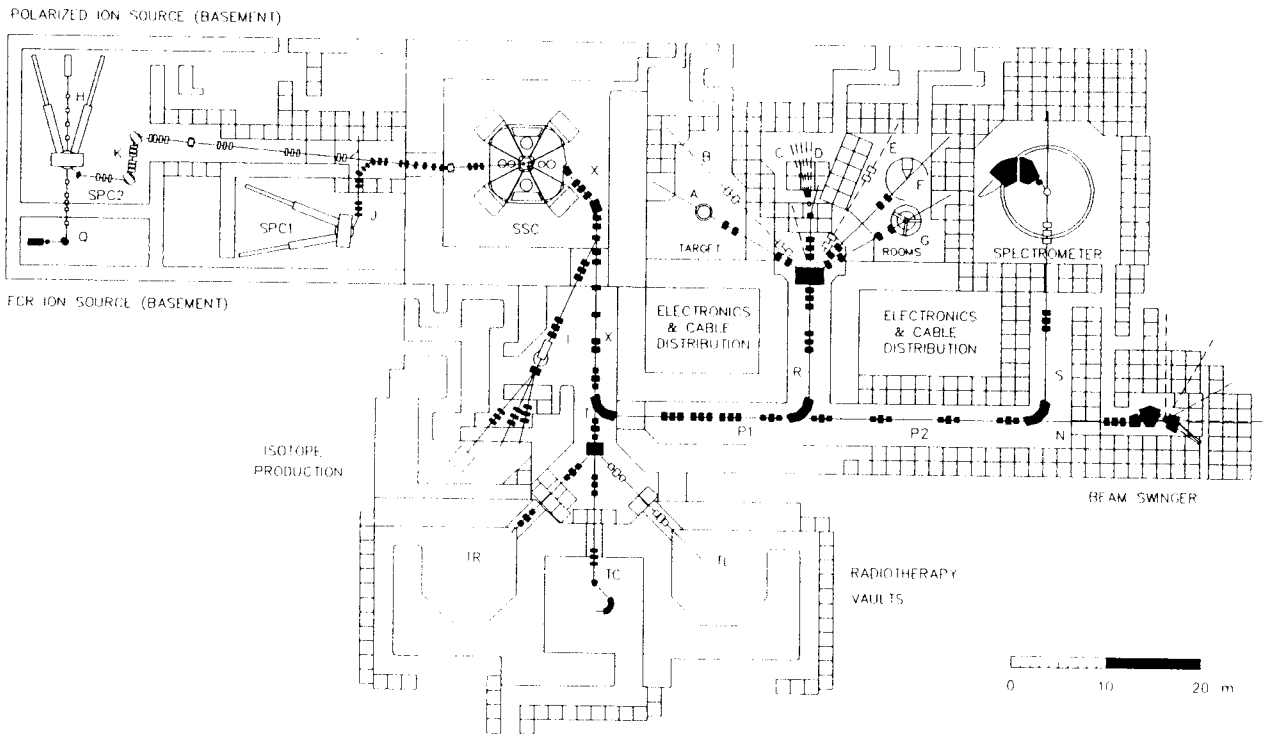

Figure 3.1 *Layout of the NAC cyclotron facility.*

Neutron therapy facility

At the radiotherapy facility the neutron producing target is housed inside an isocentric gantry located at the end of the beamline in vault TC (Figure 3.1). Figure 3.2 shows a schematic of the gantry which is capable of ± 185° rotation and

includes a collimator with a continuously variable aperture providing field sizes from 5.5 × 5.5 cm^2 to 30 × 30 cm^2 at a source–to–axis distance of 150 cm. The beamline components in the gantry include a number of magnets which bend, focus and steer the proton beam onto the target. A separate insulated annulus upstream of the beam scanner and the scanner itself provide diagnostic information for centering the beam inside the beamline. Heat dissipation in the target limits maximum proton beam intensities to 30 μA.

Neutrons are produced by impinging 66 MeV protons onto a 19.6 mm thick beryllium target (Jones *et al.*, 1988). Only 40 MeV of the incident beam energy is dissipated in the target which is encapsulated in a 0.55 mm thick cylindrical copper jacket. A 2 mm air gap at the far side of the jacket allows for possible heat expansion of the beryllium. The protons are finally brought to rest in a 1 mm copper plate which is cooled on both front and back surfaces by 1 mm of flowing water. The end of the copper target assembly is 3 mm thick. The beam is pre–collimated by 13 cm of steel before passing through a drawer containing both the hardening and flattening filters and an X–ray tube. Thereafter the beam passes through twin transmission ionization chambers, a wedge filter carousel and is finally shaped by the collimator. Although not initially included, the incorporation of a hardening filter was deemed necessary during preclinical calibrations following radiobiological and microdosimetric investigations (Slabbert *et al.*, 1989). The hardening filter is permanently mounted in the beam and consists of a polyethylene sheet 2.5 cm thick. This thickness was chosen as a compromise between reducing observed variations in beam potency without substantially decreasing the dose rate as target design specifications limit the maximum proton beam intensities to 30 μA. The flattening filter assembly contains two iron filters. One is permanently in the beam and used for fields with linear dimensions less than 16 cm, while both are used for fields with linear dimensions greater than 16 cm.

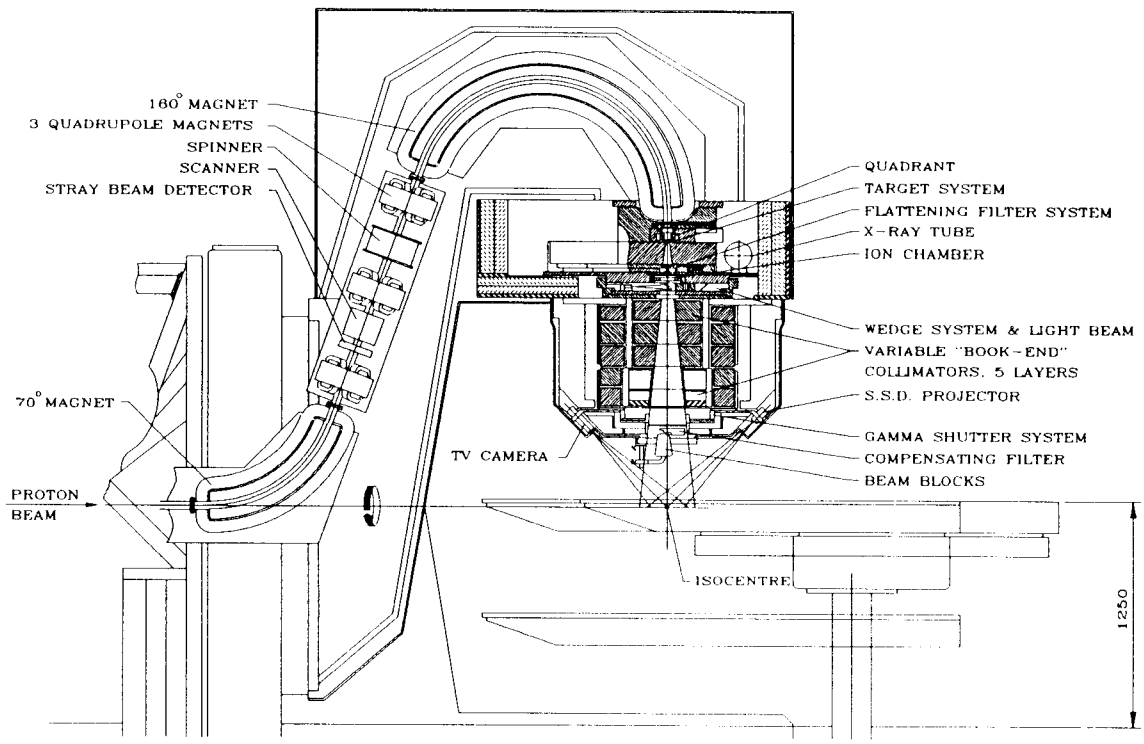

Figure 3.2 *Cross–section of the isocentric gantry used for beam delivery in the neutron therapy vault at the NAC.*

The "book–end" collimator consists of five layers of four interlocking blocks, geared to provide a tapered aperture. The three blocks closest to the target are made of pure iron while the distant two layers are made of borated polyethylene. The outerblock is covered by a 2 cm thick layer of lead on the outside to absorb gamma rays resulting from neutron activation of the inner blocks. When there is no beam on target, a lead glass shutter 5 cm thick automatically covers the collimator opening. The collimator is rotatable through 360° and provides rectangular fields symmetric about the central axis.

Neutron time–of–flight facility

Measurements utilizing neutron TOF over flight paths of up to 12 m are possible in the experimental area marked D in Figure 3.1 (Cornell *et al.*, 1991). A more detailed schematic diagram is given in Figure 3.3. Quasi mono–energetic neutron beams are generated by bombarding a relatively thin target with protons of a particular energy

up to a maximum of 200 MeV. The chosen nominal proton energies for this work were 30, 45 and 66 MeV. In each instance a 1.1 mm thick beryllium disc served as the neutron producing target. The target is fitted into a holder forming part of a ladder assembly which provides for a number of such discs and can be pneumatically driven. Heat dissipation in the beryllium limited the maximum permissible beam intensities to 5 μA. Focusing of the proton beam at the target position was ensured by observing the spot size illuminated on a beryllium oxide plate which was substituted for the neutron producing target. The plate is mounted at 45° to the beam direction and viewed through a system of mirrors and a TV camera. During this diagnostic procedure the beam intensity was reduced to below 100 nA by closing slits on the transfer beamline between SPC1 and the SSC.

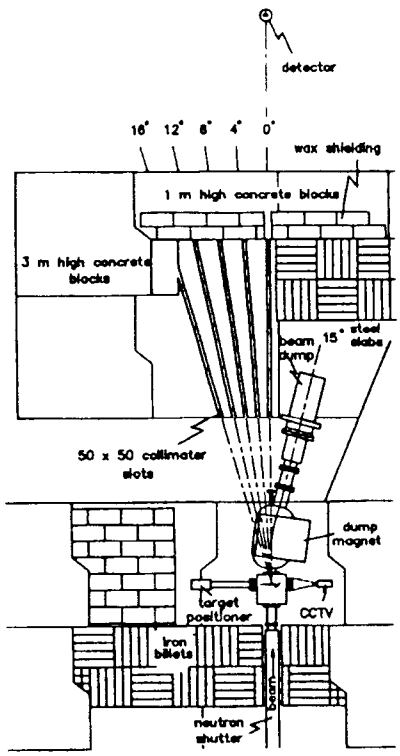

Figure 3.3 *Plan of the neutron TOF facility showing the detector set up on the 0° neutron beam. Collimators at other angles are blocked with square stainless steel rods.*

High energy protons lose only a fraction of their kinetic energy in traversing the 1.1 mm thick Be target. To prevent the emergent protons from reaching the point of

neutron detection, a dipole magnet is positioned immediately after the target assembly. The magnet sweeps away the protons into a Faraday cup at 15° off the beam axis. The Faraday cup acts as a beam dump and is well shielded by layers of concrete and iron to minimise any stray neutrons which may be produced. Integral beam current readings from the Faraday cup served as the principal beam monitor. The target and beam dump are situated behind a thick wall of steel and concrete which divides the experimental area. The wall screens the irradiation area from the target. Collimation of the neutron beam is provided by a 50 × 50 mm square steel collimator 1.7 m long with the exit face 4 m from the target. The collimator has several ports at angles to the incident proton beam direction ranging from 0° to 16° in increments of four degrees. Irradiations were performed in line with the 0° port whilst the other apertures were blocked off by insertion of stainless steel rods.

The time reference signal required for TOF work was derived from the RF cycle of the injector cyclotron. This operates at a frequency of 16.373 MHz for proton acceleration by the SSC up to 66 MeV. To further increase the time interval between successive proton beam bursts a pulse selector is installed on the transfer beamline linking the injector and main cyclotron (Kritzinger *et al.*, 1991). Electrostatic deflection of unwanted pulses was possible so that only every fifth pulse was injected into the SSC. The resulting frequency was then reduced to 3.275 MHz thereby increasing the time separation between beam bursts to 305 ns. The pulse width was less than 2 ns.

Van de Graaff accelerator

The Van de Graaff facility is situated on the same site as the main cyclotron complex but housed in a separate building. The accelerator operates at a terminal voltage of

6 MV and routinely delivers beams of light (H^+, H_2^+, D^+ and He^+) and heavy (O^+ and Ar^+) ions for use in nuclear physics research, ion implantation and PIXE analysis.

Uncollimated monoenergetic neutrons of 2.3 MeV were generated via the $T(p,n)^3He$ reaction. Protons of incident energy 3.1 MeV bombarded a stainless steel cell containing tritium gas which was maintained at a pressure of approximately 80 kPa. The tritium (50 Ci) is stored for convenience and reuse as uranium tritide in a separate furnace connected to the gas cell. The system is evacuated and sealed before tritium is released into the gas cell by heating the furnace to approximately 400° C. Once filled to the required pressure the gas cell is isolated from the storage system and the uranium powder ($\sim$ 5g) allowed to cool. At the end of use the tritium is returned to the furnace and reabsorbed by the uranium. When not in use care is taken to keep the storage system under vacuum to prevent oxidation of the powder. The proton beam was pre–collimated by a tantalum annulus positioned 1 m upstream from the cell. This produced a beam spot of 5 mm diameter on the entrance window (Havar foil 2.5 μm thick) to the cylindrical cell (diameter 12 mm, length 30 mm) where the protons experience an energy loss of 0.13 MeV. Subsequent energy loss and heat dissipation in the air cooled cell restricted beam intensities to 1 μA. After traversing the length of the target the protons are eventually stopped in a platinum backing. The integrated current from the target served as beam monitor for the irradiations.

CHAPTER 4

CHARACTERISATION OF THE FAURE THERAPY BEAM

Introduction

It has been suggested by Mijnheer *et al.* (1987a) that after clinical and radiobiological considerations have been taken into account the error in the absorbed dose delivered to the target volume should be no greater than ±3.5%, expressed as one relative standard deviation. This figure is applicable to both photons and neutrons and the uncertainty in the determination of absorbed dose should include the specification of radiation quality within the beam. The term radiation quality usually refers to differences in the effectiveness of radiation of different modalities or energies and varies little if at all for conventional or low LET sources such as ^{60}Co photons and high energy X–rays. In contrast for a fast neutron beam the specification of radiation quality is complicated by the presence of different types of recoil particles where each species spans a separate range of energies and LETs.

Initially only the relative biological effectiveness (RBE) between neutrons and photons was considered to be of relevance in clinical practice. Historically this was thought to be the most important factor because the RBE of fractionated neutrons relative to fractionated photons was found to be approximately 3. This was investigated by means of radiobiological assessments using various biological endpoints relevant to therapy (early and late effects in normal tissue). Due to the increasing number of neutron therapy centres and the widely differing energies used, the need arose to assess the neutron RBE between different neutron therapy beams

with the object of comparing clinical results and therapeutic protocols of different centres (Wambersie *et al.*, 1990). To this end several studies have been performed involving systematic radiobiological (Hall *et al.*, 1979; Beauduin *et al.*, 1989) and microdosimetric (Hartmann *et al.*, 1981; Pihet *et al.*, 1990) intercomparisons. Lastly it has become apparent that for a particular neutron beam, variations in radiation quality with respect to different irradiation conditions needed consideration.

The early generation of neutron therapy beams mostly exploited the Be(d,n) reaction as a radiation source and successful treatments were essentially limited to superficial tumours. The variation of radiation quality in the absorbing medium was examined and no marked changes in the quality of the neutron component could be found (Zeitz *et al.*, 1975; Hogeweg *et al.*, 1978). Nevertheless, because of the comparatively large RBE of neutrons relative to gamma rays, it was deemed necessary to account for the accompanying photon component which could vary significantly with depth within the primary beam. The advent of the new generation of dedicated accelerators with isocentric delivery systems saw high energy protons impinging on a semi–thick Be target serve as the principal source of fast neutrons. The neutron energy distribution for the (p,n) reaction is characterized by a significant low energy component which is radiobiologically more effective. Radiobiological and physical measurements have demonstrated that unless modified by means of a hydrogenous filter, or a thinner target, these neutrons are preferentially scattered out of the beam as it penetrates the absorbing medium. As a result of the "hardening" of the neutron spectrum the effectiveness of the beam is reduced at greater depths and a variation in the RBE is observed (Hall *et al.*, 1982; Hornsey *et al.*, 1988). As more facilities of this type are commissioned, the weight of experimental evidence grows concerning the variation of beam quality with spatial position inside a water phantom (Hill *et al.*, 1991).

The nature and magnitude of these variations depend upon certain design features, for example projectile type and energy, target thickness, beam filtration, collimation and shielding, all of which make each therapy facility unique. To systematically identify irradiation conditions that bring about variations in beam quality in a homogeneous tissue–like medium, required that a comprehensive survey of the p(66)/Be(40) therapy beam at the NAC be undertaken. If quality variations can be reliably quantified and prove to be of clinical significance, then a discrepancy between the prescribed dose at the point of measurement and the effective dose delivered at that point must be recognised.

Materials and Methods

Radiobiological assays do not readily lend themselves to systematic surveys of radiation fields because they are usually time consuming and yield quantities that have inherently large uncertainties. An alternative approach is to identify a physical parameter that is easily determined and correlates with measured variations in RBE. Whilst no biophysical model exists which adequately describes radiobiological findings relevant to therapy, the measurement of microdosimetric spectra can provide comprehensive and detailed information on radiation quality (Menzel *et al.*, 1990). The parameter y^*, the dose mean lineal energy corrected for saturation, obtained by applying a biological weighting function to the measured dose distribution in lineal energy has been shown to correlate well with observed changes in RBE for some biological endpoints (Stinchcomb *et al.*, 1986; Pihet *et al.*, 1988). Although a more clinically relevant function has been devised for comparing different therapy beams (Menzel *et al.*, 1990) earlier studies in the NAC therapy beam where beam filtration was examined have shown the practical value of utilizing y^* measurements to

demonstrate radiobiologically significant changes in beam quality (Slabbert *et al.*, 1989). Moreover, previous studies have shown the sensitivity of single event spectra to subtle changes in physical beam characteristics for p(66) type beams (Binns and Hough, 1988; Pihet, 1989; Taylor *et al.*, 1990). A thorough microdosimetric study was therefore considered judicious to fully assess the character of the Faure therapy beam and obtain reliable data that could be incorporated into treatment planning schedules.

Microdosimetry measurements were performed with the TEPC and experimental system described in Chapter 2. Irradiations were carried out both in–air and in–phantom with the detector orientated vertically and perpendicular to the incident beam. Horizontal beams were used throughout and all observations made under therapy conditions with both the hardening and the appropriate flattening filters in position. In–phantom studies were routinely conducted in a 60 × 60 × 60 cm^3 water filled tank positioned at an SSD (source surface distance) of 150 cm. The walls of the phantom were made of Perspex 1 cm thick. Beam quality as a function of spatial position inside the phantom was examined as was the effect of changing field size. In addition other conditions relevant to radiation therapy were assessed for quality variations. These included the effect of flattening filters and wedges on the beam profile and changes in the volume of the irradiated phantom. A separate in–air study was made in the dose build–up region using custom made caps of different thicknesses.

Results

Depth dose

Measurements were performed at different depths on central axis to assess the effectiveness of the 2.5 cm thick polyethylene hardening filter. Data were obtained in a 10 × 10 cm^2 field for depths ranging from 2.5 cm to 25 cm, as measured from the front face of the phantom to the centre of the detector volume. Normalised dose distributions for three different depths are illustrated in Figure 4.1. Qualitatively a slight but distinct trend is apparent in the spectra. The dose component associated with slow protons in the beam ($14<y<140$ keV μm^{-1}) is reduced with depth as the

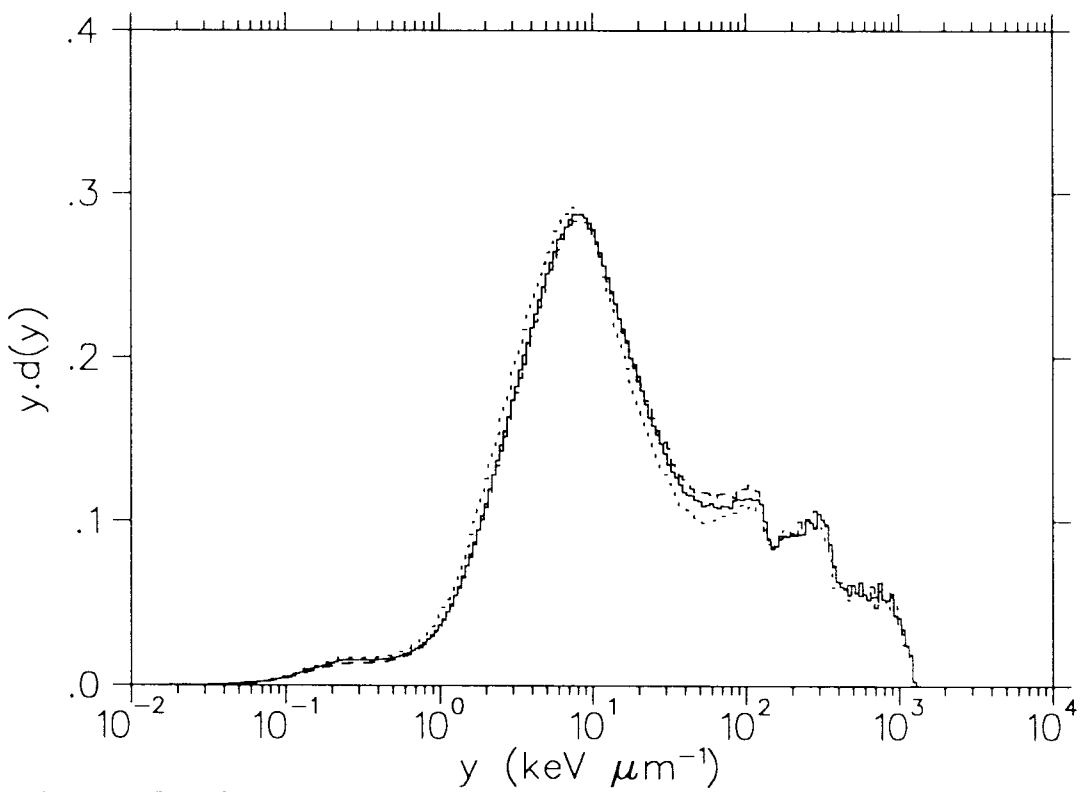

Figure 4.1 *In-phantom microdose spectra measured for a 10 × 10 cm^2 field on central axis at different depths of 2.5 (- - -), 10 (——) and 25 cm (· · ·) with the permanent 2.5 cm thick polyethylene filter installed.*

fast proton peak ($1<y<14$ keVμm^{-1}) migrates to slightly lower lineal energies. These observations are consistent with a progressive hardening of the neutron beam with depth. Similar trends have been noted in other unfiltered p(62)/Be and partially

filtered (2 cm polythene) p(65)/Be therapy beams (Taylor *et al.*, 1990; Pihet, 1989).

Values for the parameters $\bar{y}_F$ and $\bar{y}_D$ are presented together with the photon dose fractions in Table 4.1. Slight decreases in the $\bar{y}_F$ and $\bar{y}_D$ values are indicated as the beam hardens and the gamma component increases with depth.

More relevant to possible variations in beam quality however are changes in y*. These are shown in Figure 4.2 for the total beam (neutrons + gammas) and neutrons only. A decrease of 6% is noted between depths of 2.5 and 20 cm for both curves, indicating that the photon component has an insignificant influence on the variation in y*. Microdosimetric studies in other therapy beams generated with high energy protons have shown more marked changes. In a filtered p(42)/Be beam a reduction

Table 4.1 *Depth dose for different field sizes.*

	Depth (cm)					
	2.5	5.0	10.0	15.0	20.0	25.0
Field size (cm^2)			$\bar{y}_F$ (keVμm^{-1})			
5.5 × 5.5	–	4.16	–	3.83	–	3.51
10 × 10	3.59	3.85	3.59	3.49	3.31	3.28
20 × 20	–	3.27	3.06	3.02	–	2.82
			$\bar{y}_D$ (keVμm^{-1})			
5.5 × 5.5	–	84.8	–	83.6	–	80.8
10 × 10	83.5	82.1	83.5	83.2	79.4	80.3
20 × 20	–	82.3	80.3	81.9	–	78.1
			γ (% of total dose)			
5.5 × 5.5	–	3.6	–	4.1	–	4.6
10 × 10	4.3	4.4	5.0	5.2	5.5	5.5
20 × 20	–	6.1	6.9	7.4	–	7.5

in y* of 15% was observed between depths of 2 and 30 cm (Kliauga *et al.*, 1989) whilst in the p(65)/Be beam at Louvain–la–Neuve estimated quality variations of 5 – 10% were seen when moving from about 2 cm to 15 cm depth (Pihet *et al.*, 1988).

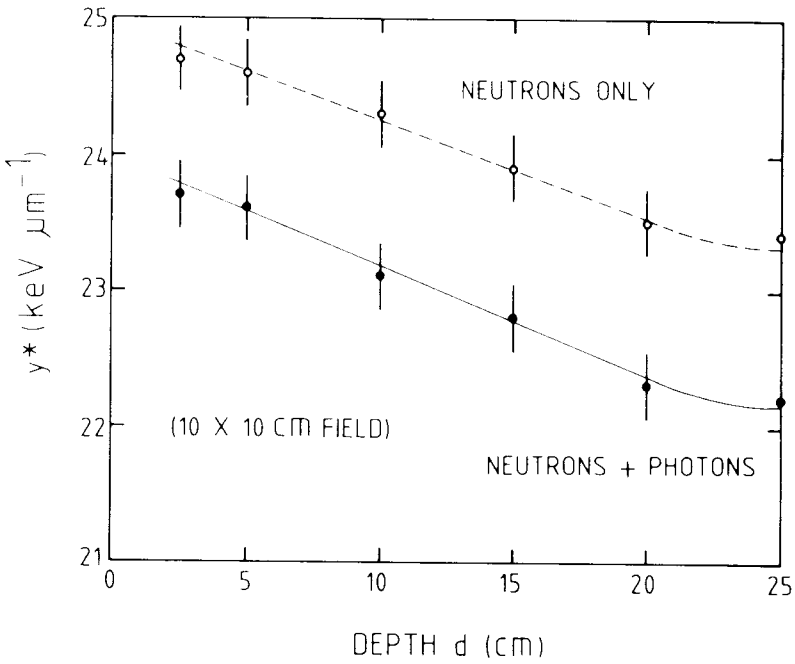

Figure 4.2 *y* –values measured for a 10 × 10 cm² field on central axis at different depths in a 60 × 60 × 60 cm water phantom.*

Field size

In radiation therapy the magnitude of the measured dose in the absorbing medium is a function of the dimensions of the radiation field. This effect is attributed primarily to scattering in the collimator and to a lesser extent in the medium. This is true for both photon and neutron fields and the appropriate output factors required for clinical application are needed for both modalities. An important difference, however, between photons and neutrons is that for the latter the radiation quality is affected by the scattering process. To evaluate these changes in beam quality,

single–event spectra were measured for different field sizes and at different depths.

The effect of changing from a 5.5 × 5.5 cm^2 to a 20 × 20 cm^2 field size at a depth of 15 cm on central axis is depicted in Figure 4.3. As the field size is increased the slow and fast proton components are respectively enhanced and reduced. This is due to scattering of the primary neutrons within the collimator as the aperture enlarges with field size. Similar findings have been reported (Taylor *et al.*, 1990) where the effect is attributed to in–scattering of lower energy neutrons from the expanding beam periphery.

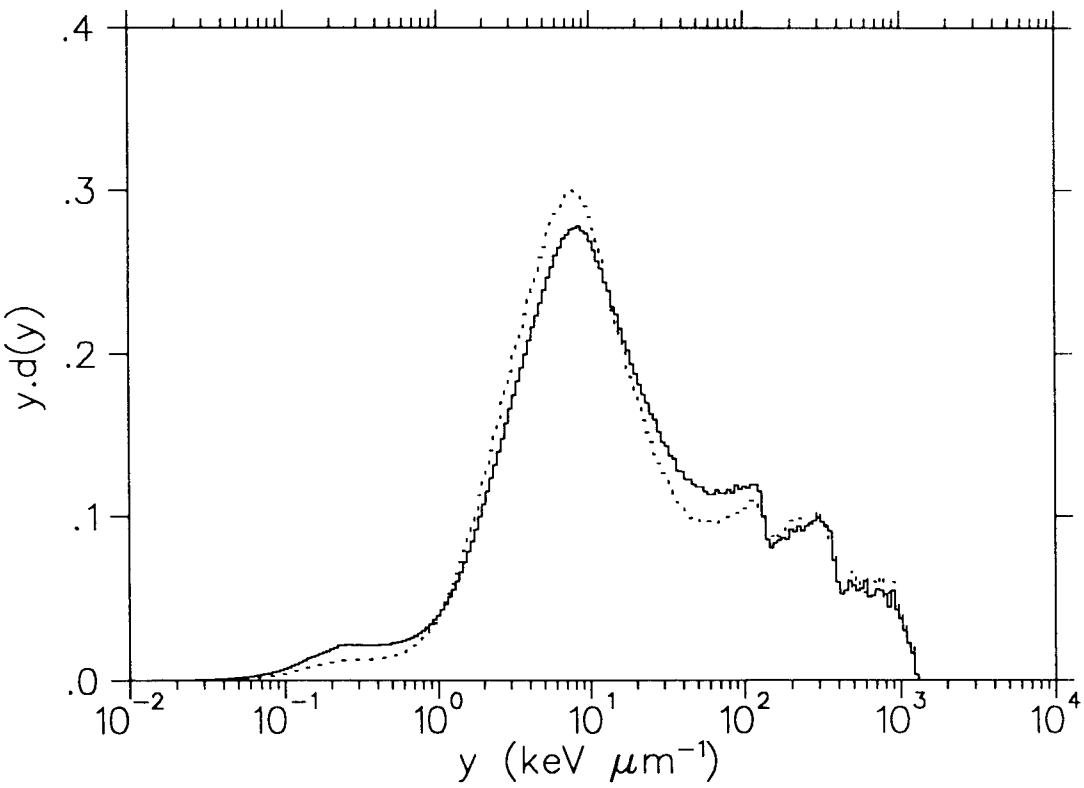

Figure 4.3 *Single event spectra measured on central axis and at a depth of 15 cm for a 5.5 × 5.5 cm^2 (· · ·) and 20 × 20 cm^2 (——) field.*

Measured y*–values as a function of field size and depth (5, 15 and 25 cm) are shown in figure 4.4 for square fields 30 to 400 cm^2. The average changes, denoted by $\bar{\Delta}y^*$, were 1.4 and 0.7 keVμm^{-1} respectively for neutrons only and the total beam (neutron plus photons). The smaller increases noted for the total beam are attributed to the

varying γ–component which is shown in Figure 4.5 to increase with both field size and depth. From figure 4.4 it is also apparent that the variation of y* between depths of 5 and 25 cm is the same for all field sizes investigated, i.e. 6 to 7%.

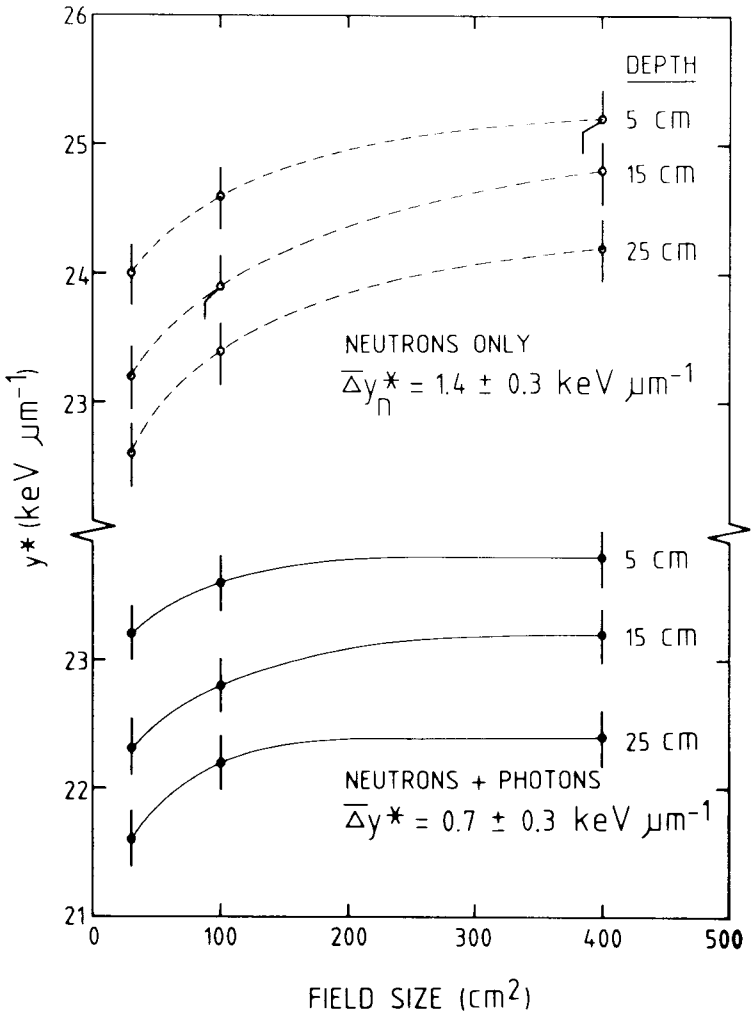

Figure 4.4 *y*–values measured on central axis at different depths as a function of field size. The averaged variation for each of the data sets is appropriately stated.*

Penumbra

At the edge of a neutron field confined to a tissue–like medium the overall quality of the beam is affected by two competing processes, a degradation of the primary beam due to scattering and a sharp increase in the photon component following interactions in the medium, principally from neutron capture in hydrogen, nitrogen and chlorine (Bewley, 1989). Measurements were performed in the penumbra to assess the nature and magnitude of quality changes in this region.

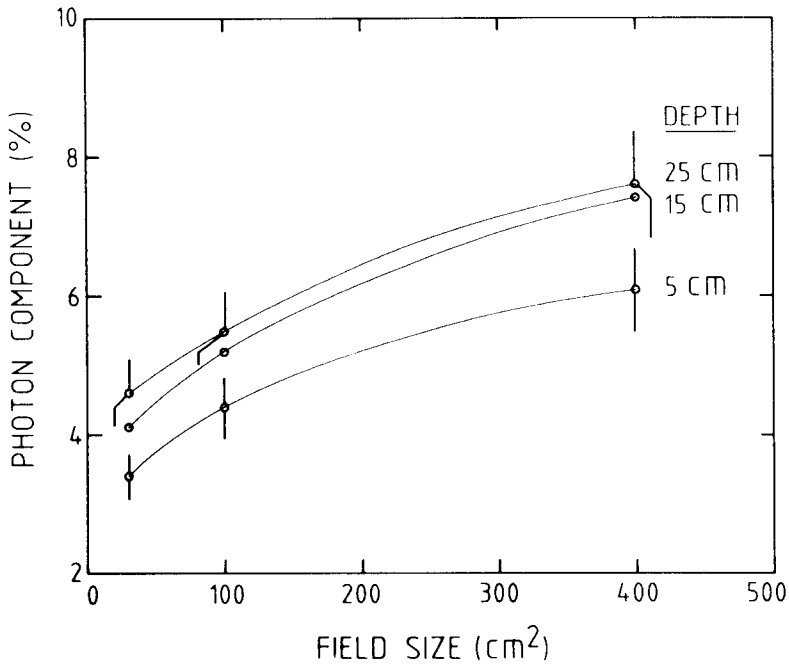

Figure 4.5 *The photon dose component in the therapy beam measured on central axis at different depths and for different field sizes.*

Experimental data were obtained in a 10 × 10 cm² field at a depth of 10 cm on central axis and for a range of lateral displacements. The quality variations were assumed to be symmetric about the central axis. Single event spectra measured at displacements of 5.5 and 8 cm from central axis are shown in Figure 4.6. These positions correspond to absorbed dose levels of respectively 40% and 10% of that on central axis. Marked changes are apparent at the edge of the field. The measurement at 5.5 cm off axis cannot be distinguished from the measured central axis spectrum whereas that obtained 8 cm from central axis shows a relative enhancement in the number of slow recoil protons accompanied by a decrease in the fast proton component. This is consistent with neutrons undergoing greater scattering in the penumbra and consequently suffering larger energy losses. Concomitant with this is a decrease of the alpha and heavy recoil components in the dose distribution. As the neutron energies are reduced there are fewer neutrons possessing the required threshold energy for interactions which lead to alpha and heavy ion production. Further, the photon

dose fraction is seen to increase substantially, primarily through neutron capture reactions. These trends have been reported for other collimated beams generated with either high energy protons (Stafford *et al.*, 1987; Pihet, 1990) or low energy deuterons (Fidorra and Booz, 1981; Hough and Binns, 1990) bombarding beryllium targets.

A radiation quality profile together with the corresponding photon contributions for the Faure therapy beam are presented in Figure 4.7. The pronounced increase in y_n^* between displacements of 5 and 10 cm suggests a far more effective neutron component, exemplifying energy degradation due to scattering. This enhancement in effectiveness is tempered by the rapidly increasing photon component and a 7% increase in y* is noted before the potency of the beam beyond the penumbra is reduced. Qualitatively the data are in good agreement with the transport calculations

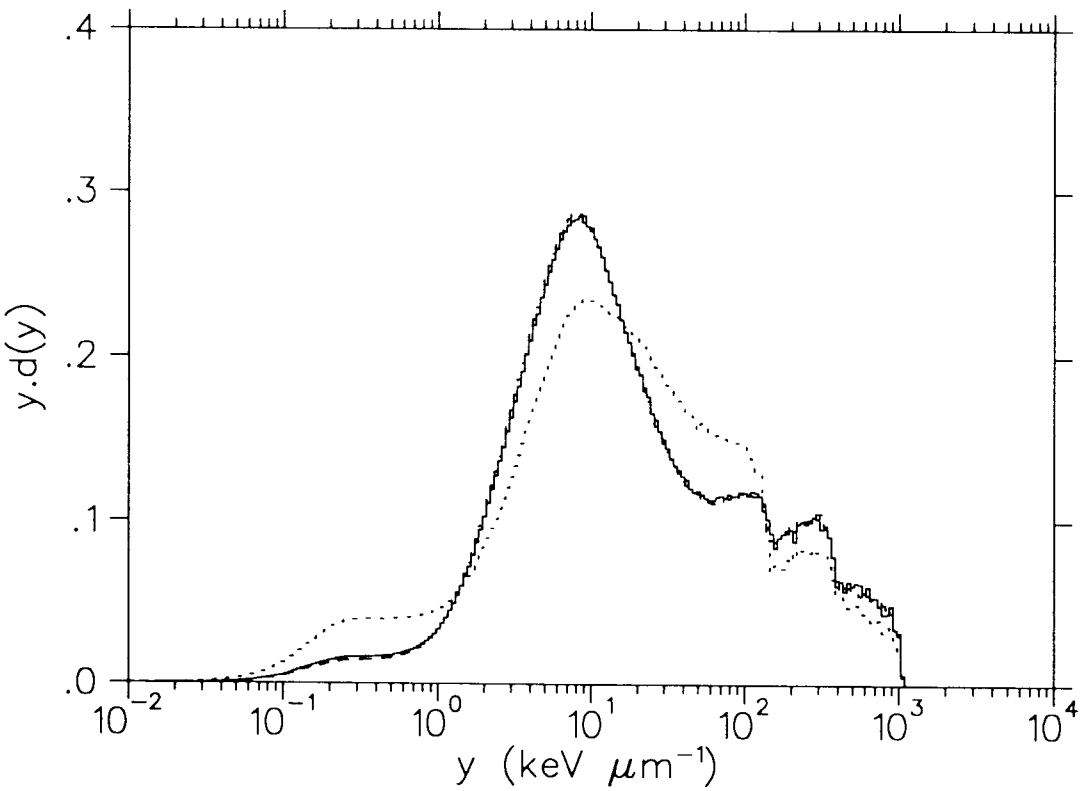

Figure 4.6 *Lineal energy spectra measured for a 10 × 10 cm field at a depth of 10 cm on central axis (– – –) and at displacements of 5.5 (——) and 8.0 cm (· · ·).*

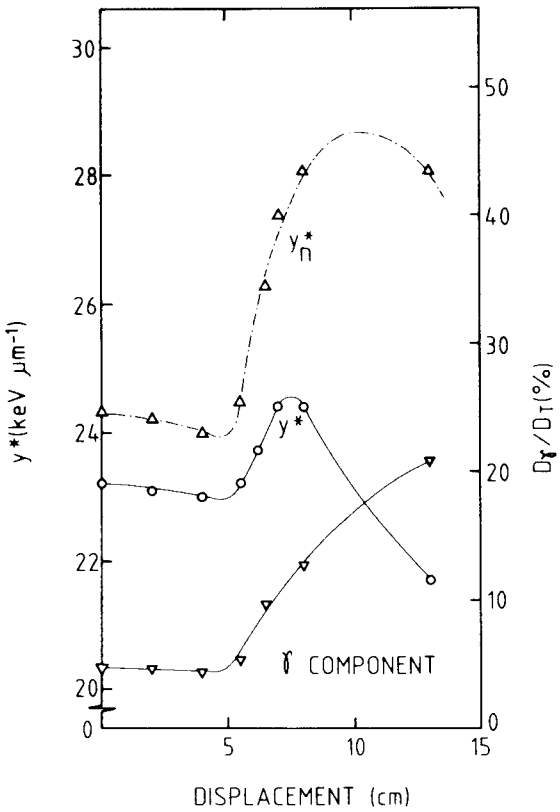

Figure 4.7 *Beam characteristics (y^* –values and Dγ) measured in the lateral plane at a depth of 10 cm and for a 10× 10 cm² field.*

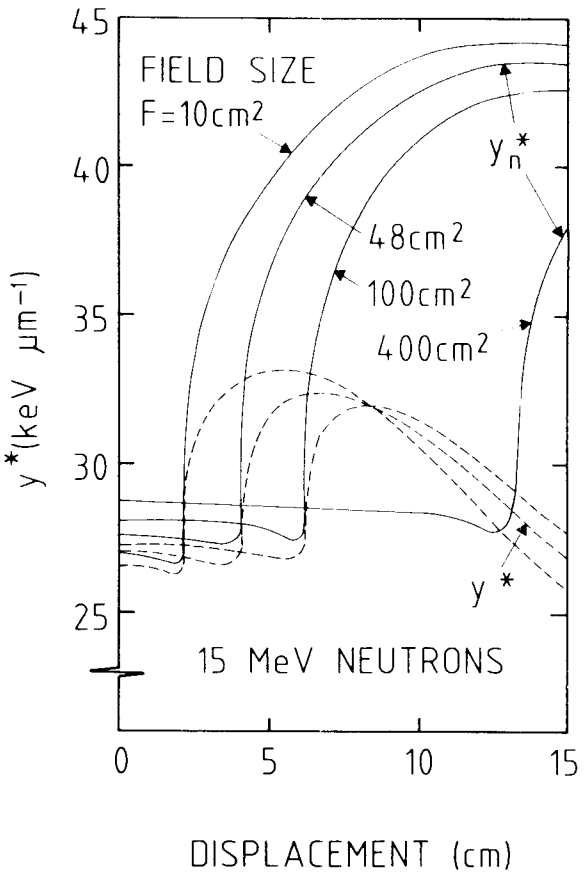

Figure 4.8 *y^*–values determined from transport calculations for a 15 MeV neutron beam and an ideal aperture (reproduced from Burger et al., 1978)*

performed for 15 MeV neutrons assuming an ideal aperture (Burger *et al.*, 1978). These are shown in Figure 4.8 where the magnitude of the calculated variations appear much greater for the lower energy beam than for p(66)/Be(40) neutrons.

Wedge filter

Measurements were performed at 2.5 cm depth inside a solid nylon phantom 20 × 20 × 20 cm³ which was positioned with its front face at an SSD of 150 cm. This phantom size was considered appropriate because wedge filters are often used in instances of extreme body curvature such as irradiations of the head and neck to correct for the

angle of oblique beam incidence. Uniformity of beam quality was examined across a 45° skewed lateral profile. This is the most slanted isodose distribution used in treatments at the NAC. A wedged shaped tungsten block, 4 cm at its thickest, was mounted transversely to the beam on a carousel in the treatment head. Uniformity in beam quality was examined across the lateral profile of a 16 × 16 cm^2 field which is the largest field size accommodated by the 45° shaping wedge. The results of measurements performed on central axis and at 5 cm on either side are presented in Table 4.2. These positions were chosen as they spanned a large portion of the field width but were distant from the penumbra. No discernible differences across the face of the wedge are apparent. Spectra measured at 5 cm either side of central axis are shown in Figure 4.9. The spectra appear indistinguishable from each other except in the region of the proton edge where the measurement at the thicker end of the wedge

Table 4.2 *Average parameters for measurements at different lateral positions in a 45° wedge field (16 × 16 cm^2). Negative displacement is towards the thin end of the wedge.*

Displacement (cm)	−5	0	+5
$\bar{y}_F$ (keV μm^{-1})	3.67	3.63	3.61
$\bar{y}_D$ (keV μm^{-1})	68.6	69.9	67.6
y^* (keV μm^{-1})	23.3	23.3	23.3
γ (%)	4.5	4.6	4.6

appears to have a perceptively larger slow proton component. This may result from a slight energy degradation due to neutron scattering in the tungsten but is not considered significant.

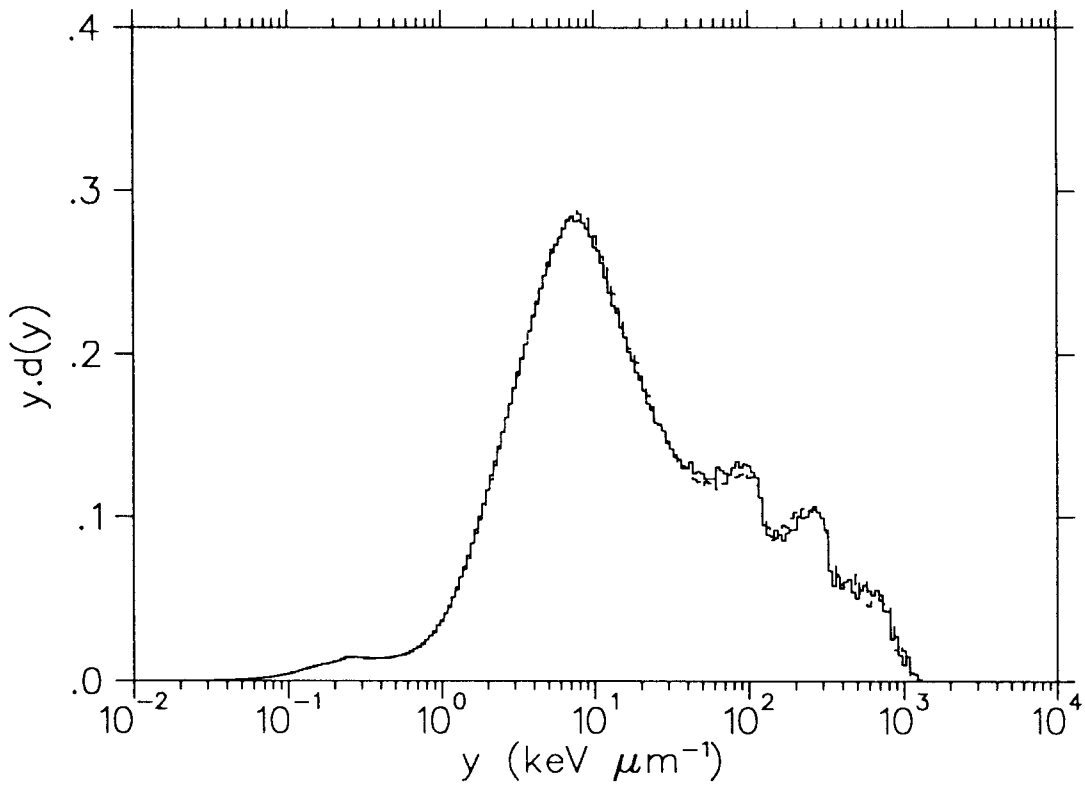

Figure 4.9 *Microdose spectra measured 5 cm either side of central axis for a 16 × 16 cm² field accommodating a 45° shaping wedge. The solid curve was obtained at +5 cm which was towards the thicker end of the wedge.*

Flattening filter

Steel flattening filters are positioned in the beam close to the target to produce a more uniform or flat isodose distributions at a selected depth. The use of these filters give rise to dose enhancements or "horns" at the surface and at depths extending to 10 cm (Figure 4.10).

Measurements were performed for a 30 × 30 cm² field, the largest in clinical use at the NAC. Only in–air data were obtained with additional build–up provided by a 16 mm thick cap of A–150 plastic. Irradiations were performed with the detector at an SAD of 150 cm and 10 cm off axis, the displacement corresponding to the point of

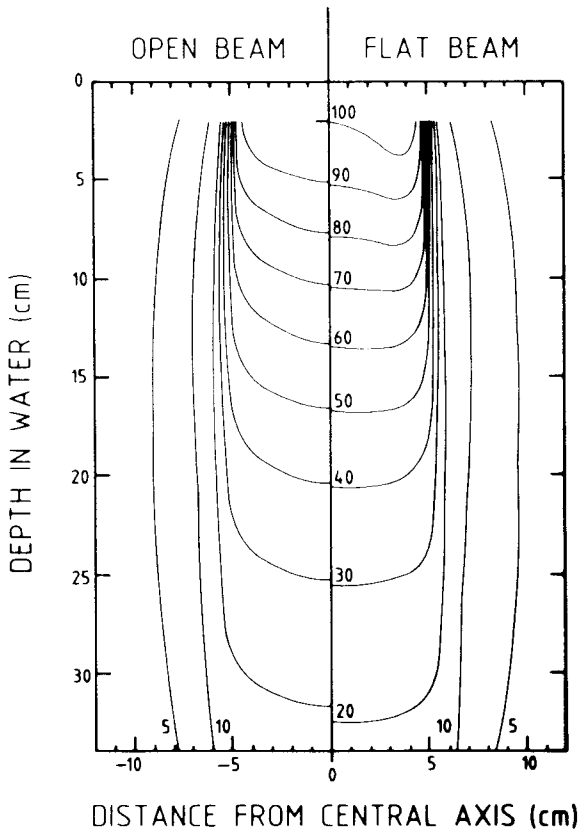

Figure 4.10 *Comparison of longitudinal isodose distributions for unflattened and flattened beams for a 10 × 10 cm² field in a water phantom.*

maximum surface dose enhancement. Both flattening filters were incorporated in the beam, as clinically appropriate for this field size. Employing the transmission chamber in the collimator head assembly as dose monitor, nearly identical spectra and data were obtained (Figure 4.11 and Table 4.3). The measured dose enhancement at 10 cm displacement was 1.09 and is consistent with earlier dosimetry data for this field size (Jones and Yudelev, 1988).

Phantom size

To assess the influence of phantom size on the noted quality variations with depth, measurements were performed for a 10 × 10 cm² field in a solid nylon phantom

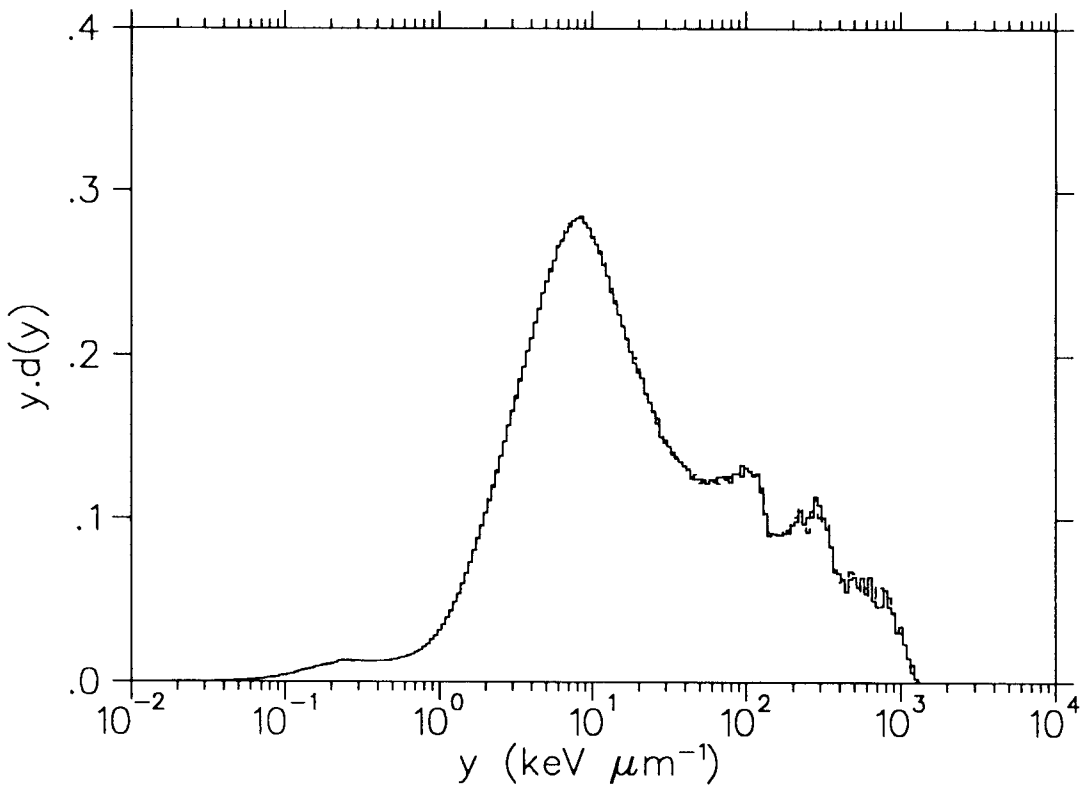

Figure 4.11 *Dose normalised lineal energy spectra measured in–air for a 30 × 30 cm field at an SAD of 150 cm on central axis (—) and 10 cm (- - -) off axis. The displacement corresponded to the point of maximum surface dose enhancement.*

Table 4.3 *Average parameters for flattening filter assessment. In–air measurements performed for 30 × 30 cm² field on central axis and at position of maximum surface dose enhancement (10 cm off axis).*

Displacement (cm)	0	10
$\bar{y}_F$ (keV μm^{-1})	4.06	4.11
$\bar{y}_D$ (keV μm^{-1})	80.9	80.6
y^* (keV μm^{-1})	24.4	24.3
γ (%)	4.14	4.02
Relative dose	1.00	1.09

10 × 10 × 20 cm^3 positioned with the front face at an SSD of 150 cm. This phantom size was chosen to minimise scattering within the medium outside the field periphery but was extended enough to allow for an adequate range of depth dose measurements. A variation of approximately 6% in y* was again observed when moving, in 5 cm increments, from 2.5 to 17.5 cm. This is in agreement with the earlier findings in a 60 × 60 × 60 cm^3 water phantom. Further measurements were performed varying the phantom size whilst at a constant depth of 2.5 cm. Positioning the detector in two solid nylon phantoms of sizes 10 × 10 × 10 cm^3 and 20 × 20 × 20 cm^3 revealed no spectral changes and yielded average parameters that were not statistically different (Table 4.4).

Table 4.4 *Assessment of phantom size for a measurement at 2.5 cm depth in a 10 × 10 cm^2 field.*

Phantom size (cm^3)	10×10×10	20×20×20
$\bar{y}_F$ (keV μm^{-1})	3.73	3.53
$\bar{y}_D$ (keV μm^{-1})	67.8	67.5
y* (keV μm^{-1})	22.8	22.8
γ (%)	4.4	4.2

Build–up

The secondary charged particles produced following neutron interactions in tissue are projected predominantly in the forward direction and consequently a transition zone exists in the absorbing medium in which secondary charged particle equilibrium is

established. In a fast neutron beam the extent of this zone is determined by the recoil protons which have the longest range. As the composition of the recoil spectrum in the build–up region alters, the quality of the radiation will change (Broerse *et al.*, 1968; Bewley *et al.*, 1974).

In the Faure therapy beam secondary charged particle equilibrium (i.e. full build–up) is established at a depth of 17 mm in A–150 plastic (Jones *et al.*, 1988). To simulate different positions in the build–up region a series of caps having various wall thicknesses were manufactured to fit over the aluminium housing of the TEPC. No special electrical properties were required of the material from which the caps were to be made and the possibility of using more freely available hydrocarbons as substitutes for A–150 was examined. For this study caps of wall thickness 16 mm were manufactured from A–150 plastic, nylon (type 6) and polyethylene. This thickness, combined with the inherent wall thickness of the detector (1.3 mm) was sufficient to provide full build–up. Irradiations were performed in–air for a 10 × 10 cm^2 field with the centre of the detector positioned at an SAD of 150 cm. Using the transmission chamber as fluence monitor, the different detector/build–up cap combinations were exposed to the beam and the absorbed doses evaluated. Figure 4.12 shows the three fluence normalised spectra. Whereas no significant differences were observed between measurements performed with the A–150 plastic and nylon caps, a clear difference was manifest when polyethylene was used. The enhanced fast proton component and the associated higher dose recorded for the same exposure are quantified together with microdosimetric parameters in Table 4.5. The larger proton recoil component measured with the polyethylene cap is due to the higher hydrogen content and accounts for the enhanced dose.

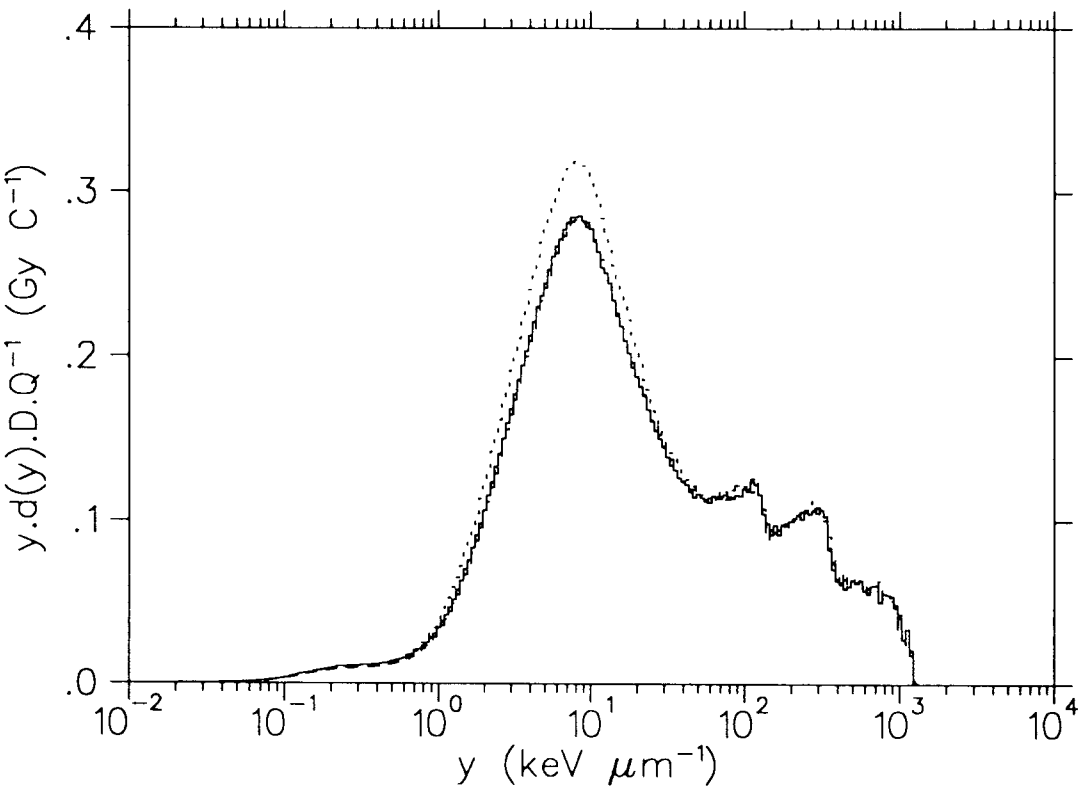

Figure 4.12 *Fluence normalised microdose spectra obtained in the p(66)/Be(40) therapy beam. In–air measurements were performed with different build–up caps of similar thickness placed over the TEPC manufactured from polyethylene (···), A–150 plastic (——) and nylon (- - -).*

Satisfied that nylon (type 6) was a suitable build–up substitute for A–150 plastic in the p(66)/Be(40) neutron beam, additional nylon caps were made with 2, 4 and 8 mm thick walls and irradiations performed under the same conditions as above. Single event spectra obtained with no build–up cap and with caps of wall thickness 2 and 16 mm are shown in Figure 4.13. The distributions are again normalised to unit neutron fluence and not unit absorbed dose. The increasing wall thickness has no apparent influence on the spectrum for either the alpha particle or heavy recoil components, as seen for lineal energies above the proton edge (y> 140 keV μm^{-1}). The intrinsic wall thickness of the counter is 1300 μm and ensures charged particle equilibrium for α–particles that are produced in a p(66)/Be(40) beam (ICRU, 1977).

Table 4.5 *Microdosimetric parameters determined from single–event spectra measured using different build–up caps. Dose fractions were calculated for two lineal energy regions; $y<140$ and $y \geq 140$ keV μm^{-1} and expressed as a ratio.*

	Hydrogen (% weight)	$\bar{y}_F$ (keV μm^{-1})	$\bar{y}_D$	y*	Dose fractions (y<140)/(y≥140)	Relative dose
A–150 plastic	10.2	4.22	86.5	24.0	5.15	1.00
Nylon (type 6)	9.8	4.55	86.6	24.3	5.11	0.99
Polyethylene	14.4	4.31	81.7	23.1	5.56	1.08

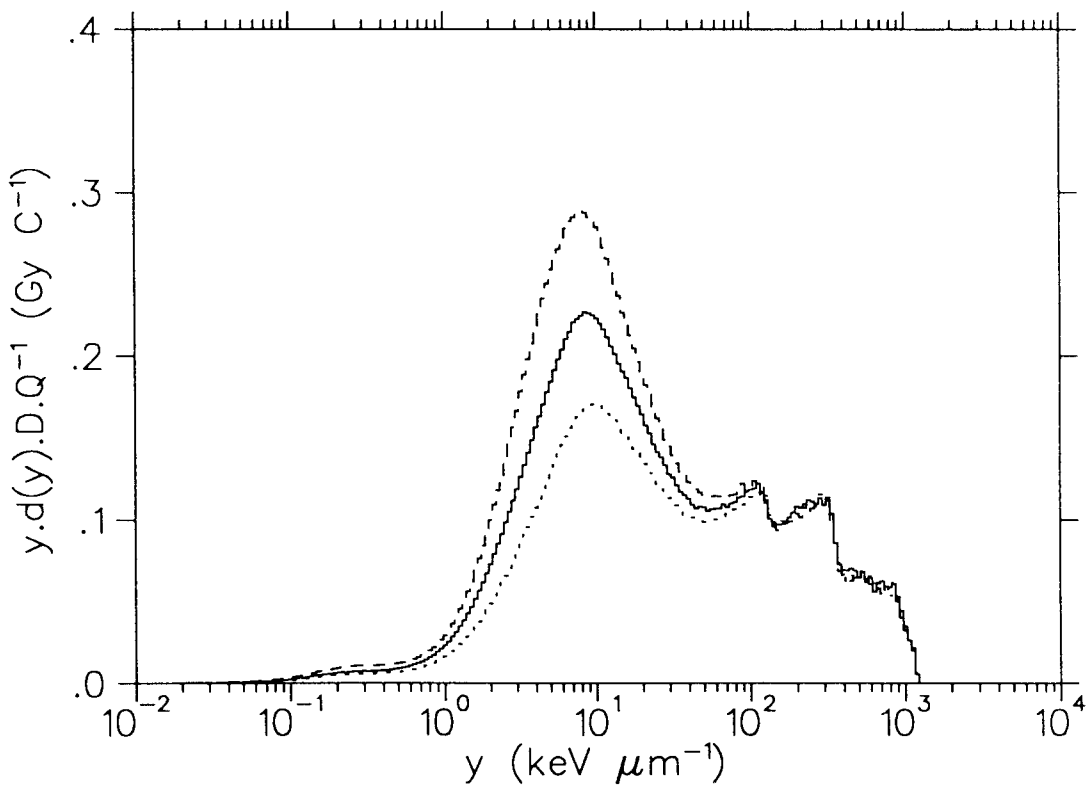

Figure 4.13 *Fluence normalised microdose spectra measured in the p(66)/Be(40) therapy beam using a bare TEPC(···) and with nylon build–up caps of 2 (——) and 16 mm (- - -) wall thickness.*

In contrast, the peak in the dose distribution centered at approximately 10 keVμm^{-1} and associated with the fast proton component is significantly enhanced with increasing build–up. Similar findings have been reported for measurements performed in a 60.3 MeV quasi–monoenergetic beam (Menzel *et al.*, 1988) where the build–up region extended over greater thicknesses due to the higher average energy of their beam. In Figure 4.14 a curve depicting the dose build–up in A–150 plastic has been fitted to data points obtained from extrapolation chamber measurements (Jones *et al.*, 1988). Values for the TEPC measurements are also plotted and indicate good agreement with the extrapolation chamber measurements. Evaluated data for each position on the curve are summarised in Table 4.6.

The decrease in y* (and hence beam effectiveness) with increasing build–up correlates with the increasing fast proton recoil component. This trend is also reflected in the ratio of the dose fractions above and below the proton edge listed in the table. The small but increasing photon dose fraction is not considered significant. An increase of 24% in y* between positions corresponding to full build–up and 71% of dose

Table 4.6 *Microdosimetric parameters evaluated from single–event spectra using nylon build–up caps of different thicknesses. The dose distributions were fluence normalized to determine the dose relative to that at full build–up (last column).*

Thickness cap (mm)	Build–up (g cm^{-2})	$\bar{y}_F$	$\bar{y}_D$	y* (keV μm^{-1})	D_γ (%)	Dose fractions (y≥140)/(y<140)	Relative dose (%)
0	0.143*	5.87	116.9	29.9	2.5	0.309	71.0
2	0.368	5.16	100.5	26.9	2.7	0.247	85.1
4	0.593	4.94	93.3	25.8	2.8	0.224	91.1
8	1.043	4.67	88.2	24.7	3.0	0.205	97.0
16	1.943	4.47	84.6	24.2	3.2	0.193	100.0

* Counter wall thickness, no build–up cap

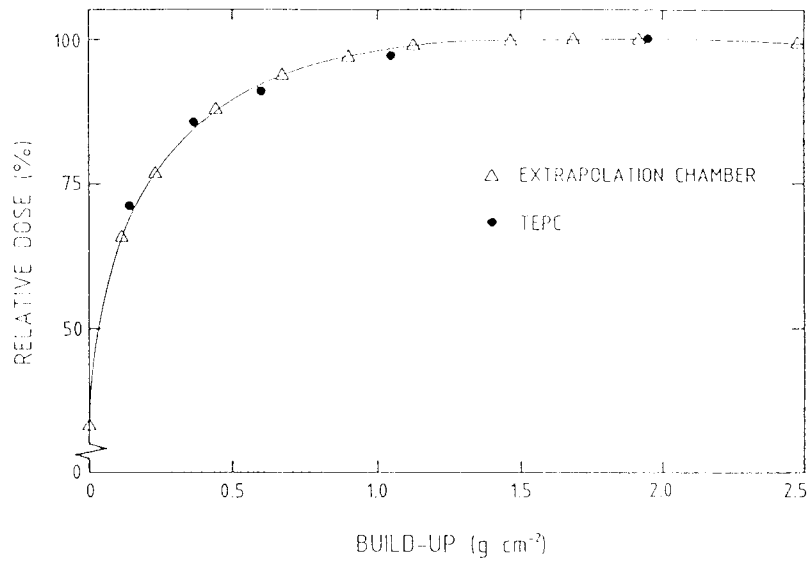

Figure 4.14 *Dose build–up curves measured in the p(66)/Be(40) therapy beam using an extrapolation chamber (Δ) (Jones et al., 1988) and a TEPC (•).*

maximum is noted. As yet unpublished data with the CHO–K1 cell line indicates an increase in RBE of 73% between a depth of 17 mm and the surface (Slabbert *et al.*, 1991). Radiobiological results from other p(42) and p(66) therapy beams have shown 20 to 30% increases in the effectiveness of the beam when moving from the maximum build–up position to 1 mm depth (Hall *et al.*, 1992).

To complement these studies, the effect of using a 16 mm thick A–150 build–up cap inside a water phantom was investigated. Data were obtained in a 10 × 10 cm^2 field with the detector at a depth of 17.5 cm inside a 30 × 30 × 30 cm^3 water phantom. Dose distributions measured with and without a cap are shown in Figure 4.15. Within the limits of experimental error, no discernible differences are apparent and all average parameters agree as do the registered absorbed doses per unit neutron fluence as monitored by the transmission ionization chamber (Table 4.7).

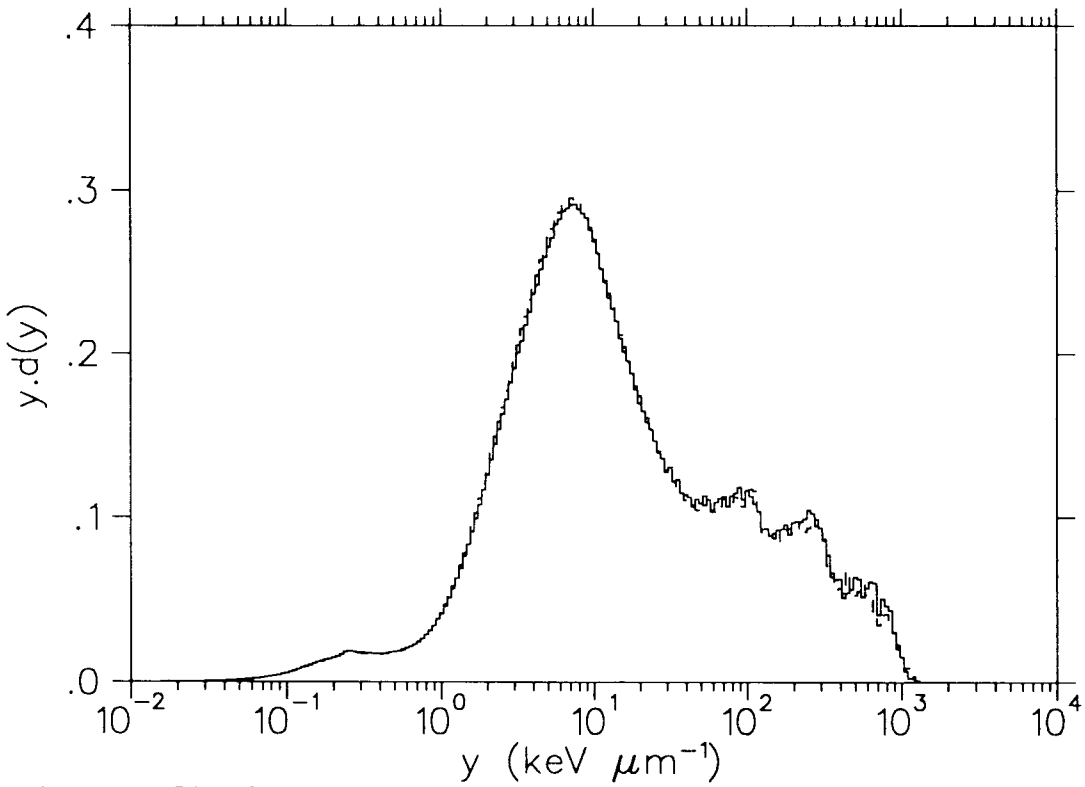

Figure 4.15 *Lineal energy spectra measured on central axis at a depth of 17.5 cm in a water phantom with (—) and without (– – –) a 16 mm thick A–150 build–up cap placed over the TEPC.*

The findings are at variance with Taylor *et al.*, (1990) where differences compatible with a variation in depth in an unfiltered p(62)/Be beam were reported when using a cap. Their observed increase in the height of the proton edge when using the cap was attributed to (n,p) scattering from carbon in the A–150 plastic. To substantiate this supposition would, however, require that the spectra be normalised to unit neutron fluence.

Table 4.7 *Comparison of average parameters for in phantom measurements with and without a TE cap.*

Parameter	Cap	No Cap
$\bar{y}_F$ (keV μm^{-1})	3.27	3.29
$\bar{y}_D$ (keV μm^{-1})	71.5	68.6
y^* (keV μm^{-1})	22.5	22.1
γ (%)	5.6	5.4
Dose (Gy)	3.07	3.07

Discussion

When irradiation conditions are altered, changes are observed in the shape and derived averages for the measured lineal energy spectra. These variations can be ascribed to quality changes in the neutron component or to a combination of changes in both the character of the neutron component of the beam and quantitative variations in the photon dose fraction. These changes can be understood in terms of neutron scattering within the phantom and also the collimator when the aperture is altered to define different field sizes. Whilst no meaningful deduction can be made about $\bar{y}_F$ and $\bar{y}_D$, the parameter y^* appears to provide a reliable and sensitive indicator of subtle variations in the physical characteristics of the field.

Depth dose studies between 2.5 cm and 20 cm show that y^* decreases by 6%, irrespective of field and phantom size. Variations in y_n^* with increasing depth demonstrate that the reduction in beam effectiveness is due to changes in the character of the high LET recoils. Progressive hardening occurs as low energy neutrons are preferentially scattered out of the beam as it penetrates the medium. As these neutrons are radiobiologically more effective their removal from the beam leads to an overall decrease in beam potency. The slight increase in the photon dose fraction does not play a role in the observed changes.

Changes in field size cause a 3% variation in beam quality, irrespective of depth. This is primarily due to an increase in the number of collimator scattered neutrons and is mostly evident when altering the field size from 30 cm^2 to 200 cm^2. This effect is tempered for all field sizes by a growing in–phantom photon component.

Moving across the lateral plane of the field reveals a uniformity in beam quality until

the periphery of the collimated field is reached. A maximum increase in y* of 7% is noted in the penumbral region where two competing processes occur. A dramatic increase in the effectiveness of the neutron component due to multiple scattering is countered by the sharply rising photon component. At shallow depths where the lateral dose profile is marked by "horns", the inclusion of a field flattening filter produces no untoward effects as regards beam quality. Incorporating a field shaping wedge also appears to have no appreciable effect on beam quality.

Studies in the build–up region demonstrate the value of being able to identify the individual components which contribute to the total absorbed dose. Whilst the neutron energy spectrum for the Faure therapy beam might be expected to change little in the first few millimetres of depth in tissue, changes are easily perceived in the measured lineal energy distributions. Smaller doses in the build–up region result from a reduced proton dose component and dramatic changes in y* are evident as the high LET dose contribution ($y > 140$ keVμm^{-1}) increases accordingly. Relative to the effectiveness observed in A–150 at full build–up, the beam is 24% more potent at a depth of 1.3 mm.

Variations in beam quality have now been quantified for different irradiation conditions in a p(66)/Be(40) therapy beam and suggest that variations in RBE do occur within the patient. In terms of dose to the tumour and surrounding tissue, these findings are important and should be further considered in clinical applications.

CHAPTER 5

TREATMENT PLANNING

Introduction

In radiation therapy the required accuracy for the delivery of absorbed dose to the target volume is determined by the steepness and separation of the dose response curves for local tumour control and normal tissue complications. Examples of dose–effect curves following neutron and photon patient treatments are shown in Figure 5.1 where it can be seen that the steepness of the curves for normal tissue complications are similar for the two radiation types (Wambersie and Gueulette, 1984). This implies that the same level of accuracy is required for each modality and that any variation in the delivered dose will modify tumour control and possibly affect the complication rate.

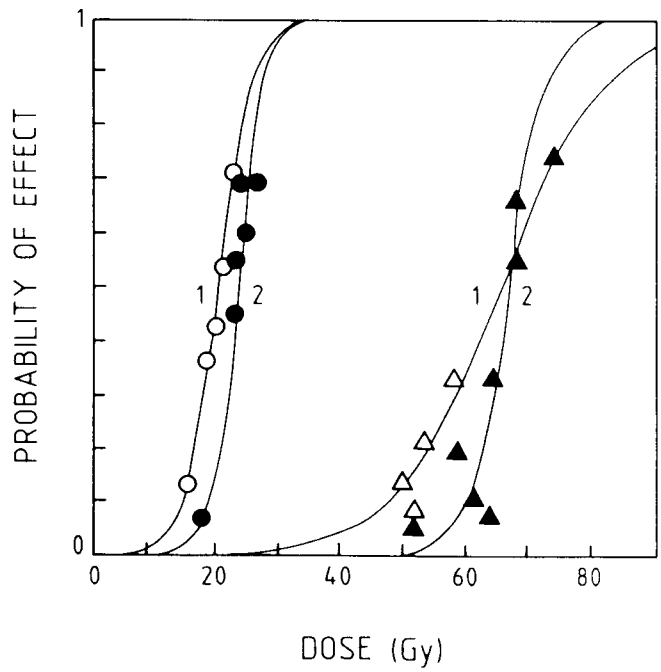

Figure 5.1 *Dose–effect relationships for tumour control (1) (open symbols) and for skin and intestinal damage (2) (closed symbols) after neutron (o) and photon (Δ) irradiation of T4B bladder tumours. The curves for skin and intestinal damage are almost identical and only one curve is shown (reproduced from Wambersie and Gueulette, 1984).*

Evidence of a relatively steeper dose–response curve for normal tissue complications illustrates the dilemma confronting radiotherapists as in practice it is often this restriction that governs the permissible dose to the tumour. There exist widely differing clinical situations where some complications are totally unacceptable (e.g. spinal cord necrosis) and others where an incidence of varying severity is acceptable if high tumour control is demanded (e.g. apical lung fibrosis). A review of clinical data for photon treatments suggests that the probability for normal tissue reactions rises from 25 to 50% for a relative dose increase of between only 4 and 10% (Mijnheer *et al.*, 1987a). It was further concluded that changes of 10% in the target absorbed dose could be detected in clinical practice.

Subtle variations in beam quality will undoubtedly undermine attempts at achieving the desired accuracy for the physical dose delivered to the tumour volume. Cognizance should therefore be taken of any possible changes and if significant, these must be accommodated in the dose prescription.

Effective dose

The observed variations in relative quality of the Faure beam with depth, field size and lateral displacement have been demonstrated in the preceding chapter. The effect with depth resulting from inadequate filtration of the primary beam has been observed in two independent radiobiological assays using V79 fibroblasts and crypt cell regeneration in mice (Slabbert *et al.*, 1989; Böhm *et al.*, 1990). The latter *in vivo* study assumes particular importance because of its sensitivity and wide acceptance as a biological model appropriate for beam calibrations. Compared with its effectiveness at a depth of 2.5 cm in water, the potency of the beam is significantly reduced at

20 cm depth, so that the same dose delivered at both positions would not result in the same effect. To obtain the same biological response at the greater depth, a 6% larger dose would be required.

A decrease in beam effectiveness is correlated with a reduced slow proton component ($14 \leq y < 140$ keVμm^{-1}) and a concomitant increase in dose contributions from the fast protons ($1 \leq y < 14$ keVμm^{-1}) and alpha and heavy ions ($y \geq 140$ keVμm^{-1}). The relative proportions per unit dose of these components (i.e. dose fractions) are given in Table 5.1 where qualitative changes in the measured microdose distributions are quantified for different irradiation conditions. The variations evident in the dose fractions when altering the square field size from 30 cm^2 to 400 cm^2 are similar to those observed with and without a beam hardening filter. The changes in the microdose spectra for different field sizes are then analogous to those obtained in the depth dose study where varying filtration conditions pertain. Similarly changes to the single event spectra measured in the penumbra and beyond (Figure 4.6) also exhibit the same trend of y* increasing due to an enhanced slow proton component. Confidence is therefore given to the assertion that for the irradiation conditions observed the measured changes in y* reflect actual variations in beam quality.

Table 5.1 *Dose fractions determined at 15 cm depth for different field sizes. Indicated in brackets are those fractions measured in the beam with no filtration and with a polyethylene filter of thickness 7 cm (Slabbert et al., 1989). Variations in the dose fractions are also stated.*

Field size (cm^2)	$1 \leq y < 14$ (keV μm^{-1})	$14 \leq y$ 140 (keV μm^{-1})	$y \geq 140$ (keV μm^{-1})	Filter thickness (cm)
400	0.501 [0.463]	0.342 [0.392]	0.157 [0.145]	0
30	0.534 [0.500]	0.304 [0.350]	0.162 [0.150]	7
ΔD (%)	+6.6 [+8.0]	−11.1 [−10.7]	+3.2 [+3.4]	

It is not within the scope of this work to discuss the complex problems of relevant RBE values for clinical use nor the influence of dose rate and dose fractionation on this RBE. The aim is rather to demonstrate that the relative changes noted in beam quality pose a hitherto unaccounted for source of error that can be eliminated.

Previously for the low energy neutron facilities the high–LET component was seen to remain constant throughout and differences in overall beam quality were attributed solely to variations in the magnitude of the accompanying photon component (Booz and Fidorra, 1981; Beach and Milavickas, 1982). Attempts have been made to obtain an effective total dose for such beams by weighting the photon dose fraction by the inverse of a derived RBE for the neutrons in the beam relative to the photons (Kellerer and Rassow, 1980; Field and Joiner, 1990; Rassow *et al.*, 1990). This approach is inadequate for p(66)/Be type beams where actual changes in the neutron component itself occur which have a more marked effect on the resultant beam quality, and hence the effective dose, than the varying photon dose fraction (Wambersie and Mijnheer, 1990). Whilst investigations in a d(14)+Be beam were of little consequence due to an absence of any real variations in neutron beam quality (Schmidt and Hess, 1988), no such study has yet been performed for a p(66)/Be beam where larger differences can be expected. In this study microdosimetric spectra are utilized to derive relative effective doses in a neutron therapy beam.

To examine the influence of these changes in the Faure beam and to estimate any discrepancies that may result in the effective dose to the tumour and surrounding healthy tissue, it is proposed that the measured y*–values be employed to derive a range of weighting factors. These weighting factors can then be applied to modify the conventional dosimetry input data to a treatment plan schedule, as measured with tissue equivalent ionization chambers, and differences quantified between the physical prescribed dose and the resultant effective dose to the tumour volume.

In the Faure beam secondary charged particle equilibrium is attained at a depth of 17 mm and this point was adopted as reference position. The conventionally measured total doses D_t were then weighted accordingly and an effective or biologically equivalent depth dose curve calculated for depths ranging from 1.7 to 20 cm as follows (Binns and Hough, 1992)

$$D_{eff} = D_t \left[(C_1 C_{sf} d + y^*_{ref}) / y^*_{ref} \right] \qquad (1)$$

where d is the depth past the point of maximum build–up and varies from 0 to 18.3 and y^*_{ref} (=28.1 keVμm^{-1}) is the y*–value at maximum build–up. Beyond 20 cm depth (i.e. d = 18.3) y* ceases to change. C_{sf} represents a sensitivity factor assessed by clinicians from clinical and radiobiological data. C_1 (= –0.0805) is obtained from a linear fit to the (neutron + photon) data of y* versus depth shown in Figure 4.2 using commercial software[+]. In the build–up region a constant y*–value equal to y^*_{ref} was applied as this study was only concerned with examining the effective doses to deep seated tumours and the surrounding healthy tissue.

An increase in effectiveness is noted with increasing square field size irrespective of depth and if normalised to a 100 cm^2 field size, y* decreases by 2% and increases by 1% when going to smaller and larger field sizes respectively. Field size related variations in the effective dose can be quantified using the following expression:

$$D'_{eff} = D_{t,100} \left[C_2 (A/100)^{100/A} + C_3 \right] \qquad (2)$$

[+] Sigmaplot Computer Graphics System
Jandel Scientific, Corte Madera, California 94925, USA

where $D_{t,100}$ is the total dose for a 10 × 10 cm² field at that depth and A the field size in cm². C_2 (= 0.01194) and C_3 (=0.9806) are averaged constants derived from the data for the lower set of curves in Figure 4.4. Fits to the data points were obtained with a non–linear least squares procedure (Marquardt, 1963) using Simplot.

Moving across a 10 × 10 cm² field yields only a minimal variation in radiation quality (Figure 4.7) but beyond 5 cm displacements more dramatic changes are noted. To determine the relevance of measurements in the lateral plane, a modified dose profile was constructed using the appropriate weighting factors as follows:

$$D'_{eff} = D_t \, (y^*_\ell \, / \, y^*_{ca}) \qquad (3)$$

Here D_t is the measured total dose as before, y^*_ℓ those values measured in the lateral plane and y^*_{ca} the y*–value on central axis, all measured at the same depth. Figure 5.2 depicts the modified dose profile, constructed from data obtained at 10 cm depth in a 10 × 10 cm² field. Only a slight broadening of the profile at the outer edges of the penumbra is apparent. The discrepancy between D'_{eff} and D_t at these displacements is of little clinical consequence and quality change in the penumbra were thus not considered further.

Neutron treatment planning

Although the interaction mechanisms of photons and neutrons with tissue differ, the isodose distributions for the Faure therapy beam are very similar to those for 8 MV photons as regards depth dose and the shape of the build–up curve (Jones *et al.*, 1988). This permits the use of algorithms normally used in photon therapy planning for the calculation of two dimensional neutron isodose distributions (Vynckier *et al.*,

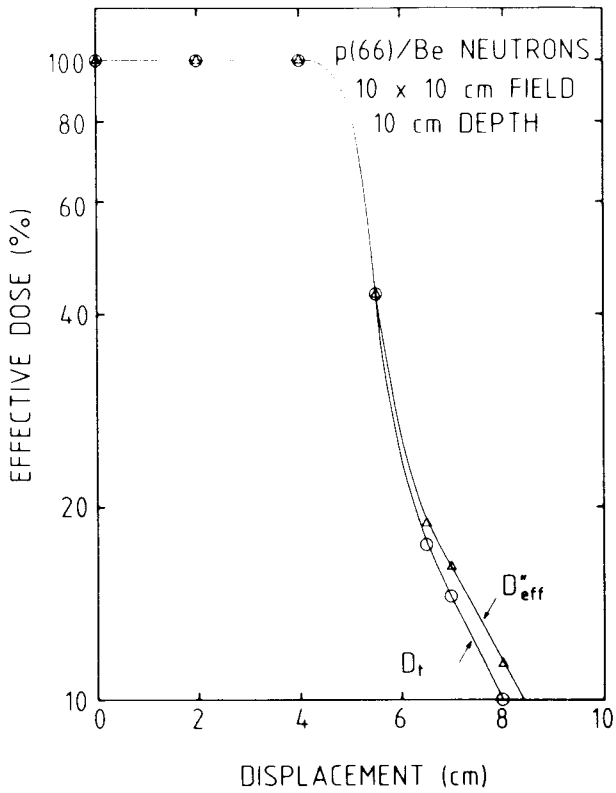

Figure 5.2 *Physical $D_t(o)$ and modified effective dose D^*_{eff} (Δ) profiles obtained for the p(66)/Be(40) therapy beam in a 10 × 10 cm² field at 10 cm depth in–phantom.*

1988). The computer planning system utilized at the NAC is the International General Electric Medical Systems, (Target 1) and employs the Bentley–Milan model for storage and data manipulation (Milan and Bentley, 1974) . The model requires 17 equally spaced central axis (cax) depth dose points, starting at the depth of maximum dose (d_{max}). Profile data at 5 equally spaced depths, with the first profile at d_{max}, are also needed. These data are stored in fan line matrices with widths chosen to enclose the 5% isodose lines at a depth of 10 cm. Cax and profile data are required for different field sizes as well as for different wedge and flattening filter combinations. These have been measured with tissue equivalent ionization chambers (Jones *et al.*, 1988) and stored in a data file. In addition, output factors for the various square field sizes and wedge combinations are provided. Linear interpolation between measured data points is used to obtain cax and profile data for intermediate depths and field sizes. The planning system employs a third order power function to calculate relative doses in the build–up region and requires the surface dose value and

the dose at d_{max}. This method is satisfactory for the build–up region in most photon beams but not for the Faure neutron beam. Using a surface dose of 75% instead of the actual value (30%) gives good agreement between calculated and measured data, except for the first 5 mm of tissue where the physical dose is lower. This discrepancy does not usually present a problem as the dose gradient in the interval is too steep for the isodose lines to be resolved and only quality changes beyond D_{max} are considered here.

Treatment plan calculation

Various parameters relevant to treatment planning have been investigated to identify those variables that give rise to significant variations in radiation quality. The depth dose and field size evaluations indicated a necessity to modify the total dose D_t by means of empirically derived expressions. As an illustration, the relationship given by equation 1 was applied to calculate a modified isodose distribution. Figure 5.3a depicts isodose curves generated for a single 10 × 10 cm^2 field using depth dose curves determined with unmodified values (D_t) and adjusted values (D_{eff}). As expected, discrepancies become more pronounced at greater depths. For two opposing fields (Figure 5.3b) larger differences are apparent at shallower depths.

The overall effect that significant changes in beam quality will have upon external beam therapy is further illustrated by calculating the integral dose to a tumour volume. A 4–field plan to irradiate a symmetrically located 10 x 10 x 10 cm^3 tumour in the pelvic region was prepared (Figure 5.4). Total doses were used throughout as input data to the computer planning system to produce an optimized treatment plan. The maximum dose (hot spot) and the mean (prescribed) dose to the tumour volume,

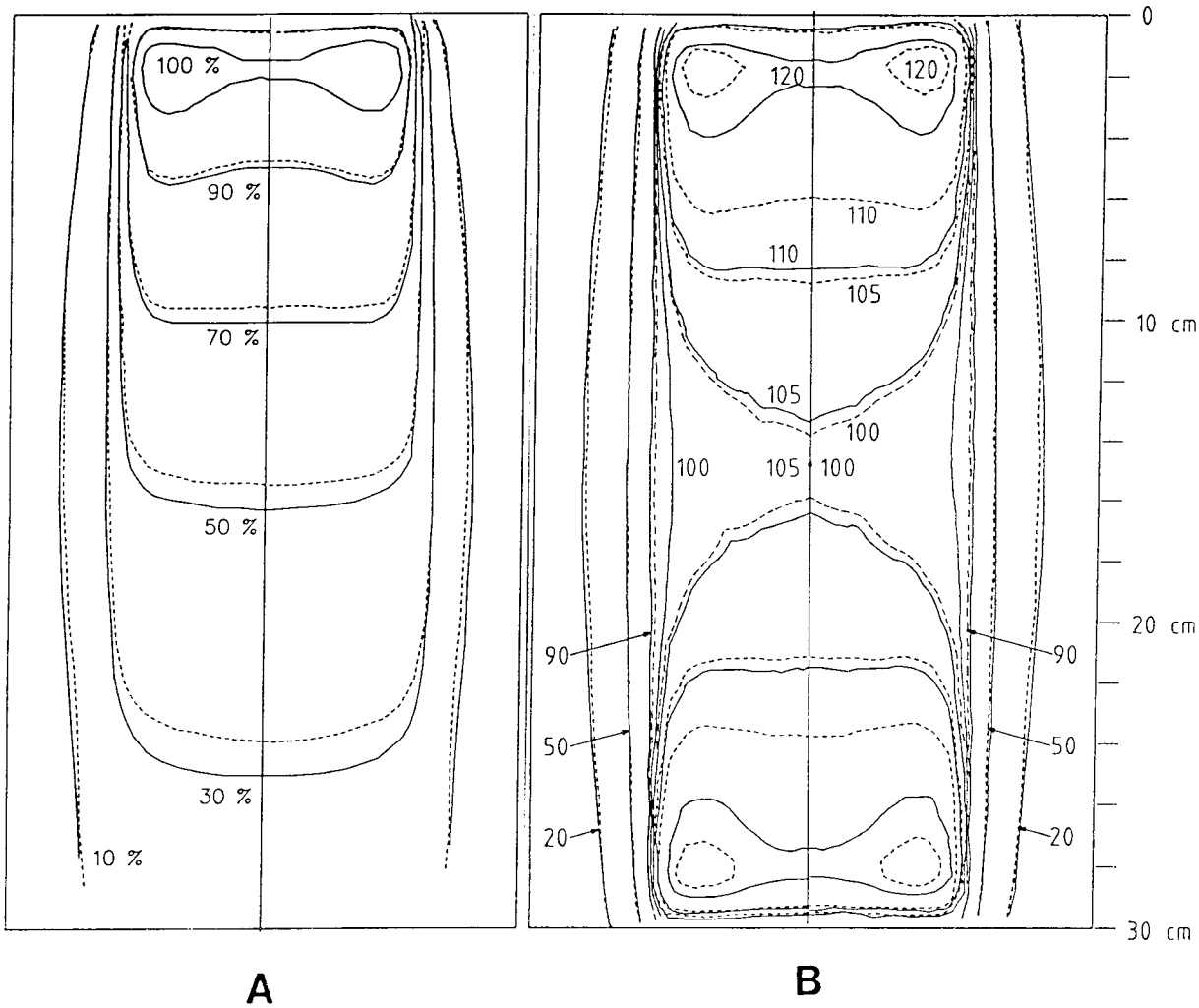

Figure 5.3 *(A)Isodose distribution generated for a 10 × 10 cm² field using an unmodified depth dose curve (solid lines) and a y*−weighted depth dose curve (broken lines). (B) Isodose contours generated for two opposing 10 × 10 cm² fields using an unmodified depth dose curve (solid lines) and a y*−weighted depth dose curve (broken lines). The unmodified isodose levels are indicated on the left−hand side of the diagram and the modified levels on the right−hand side.*

both expressed as a percentage, were calculated as 107 and 103, respectively. Modified depth dose data were then introduced using expression 1 and the plan recalculated. A value of unity was assumed for C_{sf} . The modified plan yielded a maximum dose of 103% and a mean (effective) dose of 99%, the latter indicating a difference of 4% between prescribed dose and the effective dose delivered to the

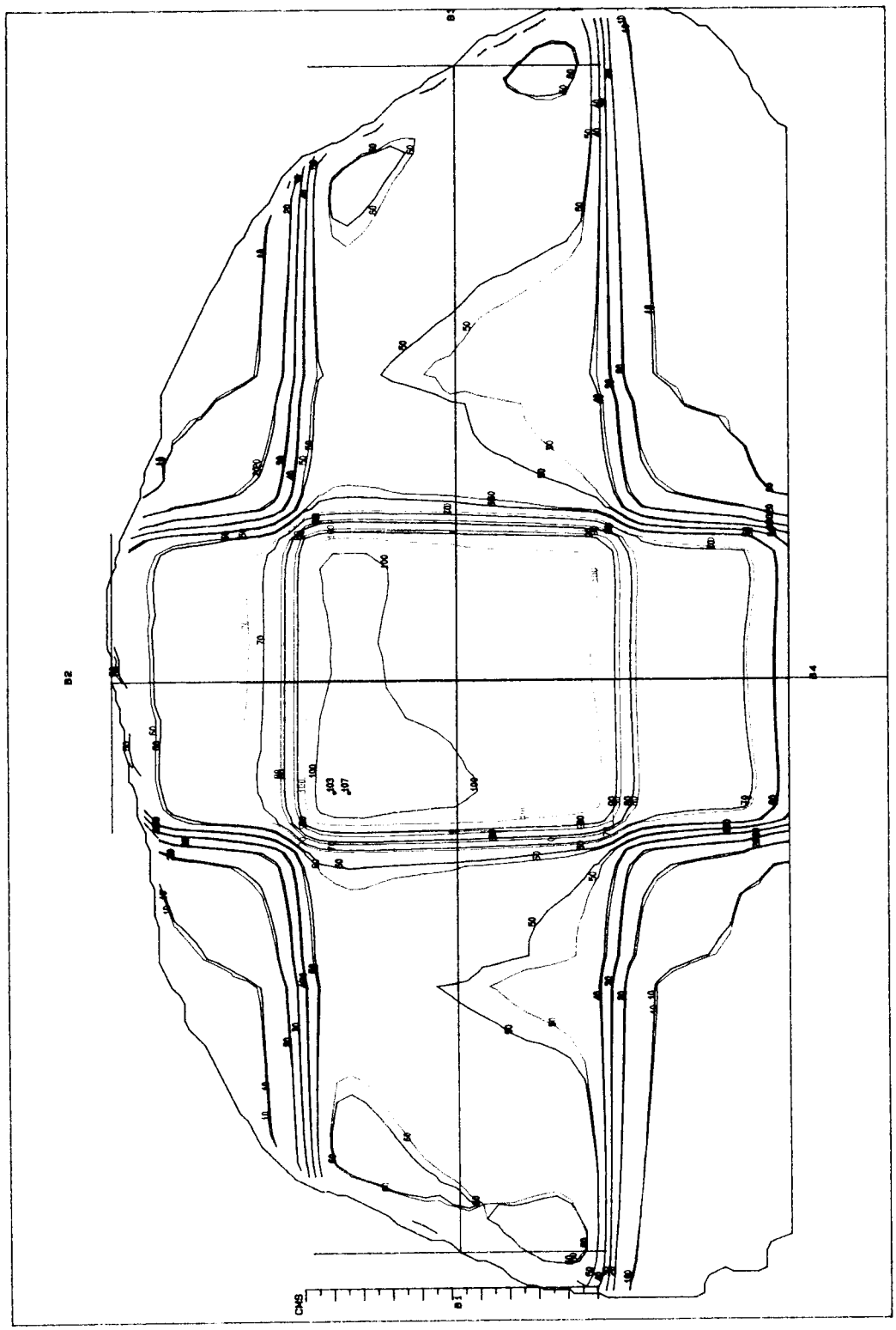

Figure 5.4 *Optimal 4–field treatment plan to irradiate a symmetrically located 10 × 10 × 10 cm³ tumour in the pelvic region. Using physical doses as input data (black lines) yields a maximum and mean dose to the tumour of 107% and 103% respectively. The plan was recalculated introducing modified effective doses (red lines) and a maximum dose of 103% and a mean dose of 99% were then obtained.*

tumour volume. In instances where expression 2 is applied, slightly larger discrepancies are to be expected.

Discussion

In the application of neutrons to radiation therapy three aspects concerning radiation quality should be addressed. Firstly, the potency of the incident beam must be assessed by physical and radiobiological means. Secondly, intercomparison studies are required to establish a Clinical Neutron Intercomparison Factor (CNIF) which converts the physical expression of dose into an effective or biological dose so that local clinical findings can be related to those observed at other centers (Wambersie and Battermann, 1987). Finally, where necessary, the spatial character of the beam within an irradiated phantom or patient needs to be evaluated. Here only the latter is examined. It has been shown that the effective dose along the central axis varies by 6% over the depth range 2.5 cm to 20 cm and that the 4–field example indicates an ensuing 4% reduction in the dose to the tumour volume. The proposal for a comprehensive quality evaluation is only justified if it can be argued that these changes, which in this case are attributed to the neutron component in the beam, are of clinical significance. It is evident from the crypt cell assay of Böhm *et al.* (1990) that a change of at least 7% in the relative effectiveness of the beam will be manifest between 2.5 and 20 cm depths. For the crypt cells this indicates a C_{sf}–value > 1 in Equation 1. In the clinical situation where fractionated doses are delivered, the 4% discrepancy in the effective dose to the tumour volume can therefore be considered a conservative estimate.

A report published by the ICRU in 1978 focused on two aspects of external beam therapy, namely the definition of the appropriate terminology and concepts, and

recommendations for reporting irradiations. This report is presently being revised to take account of new developments and changes that have occurred over the past decade. In a preview of the general trend followed in this revision the question of dose specification is addressed. The mean dose to the cancer cell population is identified as having greater bearing on tumour response than either the absorbed dose at a specified point or dose homogeneity throughout the tumour volume (Wambersie, 1990). The present study shows that by disregarding quality changes in the irradiated volume, an error of at least 4% is introduced where considerations for optimum therapy are the most critical. The quality evaluation demonstrates that the 3.5% accuracy goal set by Mijnheer *et al.* (1987a) for the dose at a specified point in the patient is exceeded by a factor of almost two over the depth range 2 to 20 cm.

It is not suggested here that doses to the tumour volume be increased in all instances where effective doses at depth are significantly less than the prescribed physical dose. The investigation does, however, show that when CNIFs are determined, quality evaluations within a phantom could be of assistance in arriving at an optimum dose to the tumour. Dosimetric and radiobiological data acquired in two p/Be beams generated at similar proton energies but characterized by different soft neutron components, must be treated with caution when performing dose–finding studies for tumour control and normal tissue tolerance at depth.

Compared to absorbed dose measurements with ionization chambers, TEPC observations demand a more sophisticated data acquisition system and data analysis is more complex. For this reason microdosimetric techniques are not part of the conventional instrumentation employed at neutron facilities for dose assessments. Single event spectra have, however, been measured at several centers (Pihet *et al.*, 1989) and although these surveys may not be fully comprehensive, sufficient data

exist for a reassessment of the depth dose information at selected centers. Moreover, much radiobiological data has been acquired at many of these centers. Where such data are available, the sensitivity factor C_{sf} can be estimated with greater accuracy. Clearly the product $C_1 C_{sf}$ is central to the argument for quality changes along central axis and would render the depth dose expression superfluous should it approach zero.

This work has shown that for a p(66)/Be(40) therapy beam the product $C_1 C_{sf}$ is large enough to warrant the recalculation of selected treatment plans. The need to account for quality variations associated with different field sizes between 30 cm^2 and 200 cm^2 is also apparent. In each instance simple expressions have been formulated to modify total dose values that have been measured by conventional means, that is with a TE ionization chamber. Unless indicated to the contrary, these expressions could in principle, find general application to similarly generated p/Be neutron beams. The significance of single event spectra is further enhanced when TEPC measurements are applied to intercomparison studies (Menzel *et al.*, 1990; Pihet *et al.*, 1990b) in which the problem of non–uniformity between different neutron beams is addressed and a method proposed to minimize the error associated with CNIF–values. The uncertainties surrounding neutron kerma in the 20–65 MeV energy range have yet to be resolved and could well prove to be larger than the dose discrepancies indicated in this study. Kerma factor uncertainties do not, however, detract from the findings of this work nor that of Menzel *et al.* (1990) and Pihet *et al.* (1990b). For the new generation of neutron beams, consideration should be given to beam quality within the patient. This could contribute to the optimization of the dose to the tumour volume and thereby enhance the efficacy of fast neutron therapy.

CHAPTER 6

TIME–RESOLVED MICRODOSIMETRY

Introduction

In the application of fast neutrons to radiation therapy there is a growing awareness of the need for more comprehensive nuclear data. This is highlighted by the requirement to accurately measure absorbed doses in neutron therapy beams which have a broad energy spectrum extending up to 65 MeV. Prospective clinical trials are currently underway at a number of neutron facilities and comparisons with conventional photon modalities are demanded. In these instances the overall uncertainty in the measured absorbed dose becomes important. For irradiation prescriptions to be equivalent and thus comparable, the accuracy in the absorbed doses administered for each modality needs to be similar and within certain specified bounds. These limits have been quantified in an earlier review (Mijnheer *et al.*, 1987a) and the overall uncertainty in the dose for high energy neutrons was estimated to be approximately 8%, nearly twice that of their photon counterparts.

In neutron absorbed dose measurements the single largest source of error derives from the lack of tissue equivalence for the wall material used in the construction of neutron dosimeters. The walls of these ionization chambers are made from Shonka A–150 plastic which was originally designed to be tissue equivalent for photons. Table 6.1 compares the elemental composition of tissue with that of A–150 plastic and shows how the proportions of carbon and oxygen in tissue are approximately reversed in A–150 plastic. The carbon content makes the plastic electrically conducting and suitable for use in the construction of ionization chambers where a potential gradient needs to be maintained between the anode (collecting electrode) and cathode (wall).

A solid conductor with the proper amounts of hydrogen and oxygen matching those of tissue has not been found.

Table 6.1 *Elemental composition of tissue and Shonka A–150 plastic in percentages by weight (ICRU, 1983).*

	H	C	O	N	Ca	F
ICRU tissue	10.2	12.3	72.9	3.5	0.007	–
A–150 plastic	10.1	77.6	5.2	3.5	1.8	1.7

To account for any dose discrepancies that may occur due to differences in the elemental composition of tissue and A–150 plastic a correction factor is applied. This factor is given by the ratio of the neutron kerma factors, that is, the kerma per unit neutron fluence for the respective materials. Kerma factors vary with energy and values spanning the entire energy range of the therapy beams in question are therefore needed. Below 20 MeV kerma factors for A–150 plastic and its main constituents hydrogen and carbon are well known as the relevant nuclear cross section data are available and direct integral measurements have been performed (DeLuca *et al.* 1984; Menzel *et al.*, 1984; DeLuca *et al.*, 1986; Pihet *et al.*, 1992b). At higher neutron energies however, the nuclear data required for kerma factor evaluations are scarce and nuclear model calculations do not provide reliable predictions. As energies increase the problem is exacerbated as more reaction channels become possible, the probabilities of which are unknown.

Kerma

A pragmatic approach is to measure the kerma factors directly and for this the kerma at a particular energy is required. Kerma can in principle be measured for A–150 plastic but not for tissue, where instead the result needs to be synthesised from data

for each of the elemental constituents. At energies below 20 MeV direct assessment of kerma is possible in specially generated monoenergetic neutron fields using spherical proportional counters with walls manufactured from the material of interest (DeLuca *et al.*, 1984; Menzel *et al.*, 1984; Bühler *et al.*, 1986; Wuu and Milavickas, 1987; Pihet *et al.*, 1992b). At higher energies pure monoenergetic fields cannot be produced and only quasi–monoenergetic fields are available where the principal energy peak is accompanied by a large low energy tail. Events from these low energy neutrons will be registered by a proportional counter and an additional kerma not associated with neutrons of the nominal energy will be included in the measured response. This spurious kerma can constitute a large proportion of the measured kerma (typically 40–50%) and independent measurements are then necessary to try and quantify the additional contribution (Schuhmacher *et al.*, 1992).

Time–of–flight

An alternative approach is to apply time–of–flight (TOF) techniques where event registration is related to the neutron time of arrival at the detector. In this way it is possible to discriminate against the unwanted events due to slower, low energy neutrons. The timing response of proportional counters operating at low gas pressures is however poor and not suited to TOF because the signal pulses produced have large variations in shape (rise time) and height (magnitude). Measurements with a 1/2–inch spherical TEPC have been performed in monoenergetic beams of low neutron energy (E_n = 50 keV) where it proved impossible to obtain a simple separation of the photon–neutron fraction by defining a linear gate on the TOF spectrum (Schrewe *et al.*, 1988a). The inferior timing characteristics observed with these counters are due to both inherent and extrinsic effects. Of particular

importance are the drift times required by free electrons to travel from the site of the original ionization in the cavity to the anode. Significant also is the problem of amplitude walk, which derives from the manner in which the timing pick–off device accommodates the large dynamic range of pulse heights associated with energy depositions inside the counter.

Recently the phenomenon of electron drift times was investigated and improvements made by changing to an isobutane–based TE gas mixture (Schrewe *et al.*, 1989) and reducing the effective volume of the counter by operating it in the so–called "helix" mode. This is achieved by applying a negative bias to the helical wire surrounding the anode and thereby restricting the sensitive volume of the counter to a small cylinder concentric with the anode (Schrewe *et al.*, 1990). This arrangement demonstrated an apparent timing response of 20 ns (FWHM) but would still be inadequate when detecting 63 MeV neutrons over a 6 m flight path. During the 20 ns time interval neutrons with energies extending down to 33 MeV would have arrived at the counter. No helix mode single event distributions were presented by the authors and it is not clear if the quoted timing response is that for the full dynamic range of pulse heights encountered in the fast neutron microdose distribution. A better timing response of 14 ns has been reported by Randers–Pehrson *et al.* (1983) where microdose distributions are shown. However, their results were obtained not using a commercial TEPC but with a custom built, small cylindrical counter of wall–less design where difficulty was experienced in calibrating the pulse height data. In neither of these studies was sufficient consideration given to the deleterious effects of amplitude walk on the observed timing response of the TEPC.

Present study

The purpose of this investigation is to demonstrate that TOF spectrometry in a high energy neutron field is possible with a commercial Rossi counter operating in helix mode. This necessitated a study of the intrinsic performance of the counter and other external factors associated with time pick–off. To optimise both pulse height and timing resolutions over the full range of event sizes contributing to the microdose distribution, suitable voltages for the anode and helix were required. Reliable dose distributions with discernible detail were successfully obtained in helix mode (Binns *et al.*, 1992) and the reduced sensitive volume determined by exposing the counter to a known neutron dose. The improved timing characteristics exhibited by this detector geometry were examined as a function of pulse height to reveal the inherent timing capabilities of the detector.

Materials and Methods

Pulse height resolution was studied by collecting single parameter event size distributions using the conventional data acquisition system described in Chapter 2. A 1/2–inch spherical Rossi–type TEPC with a wall thickness of 2.5 mm was filled with the isobutane based TE gas mixture (partial pressures of 51.4% C_4H_{10}, 42.3% CO_2 and 6.3% N_2) proposed by Schrewe *et al.* (1989). The elemental composition of this mixture is very similar to that of the propane based TE gas (Srdoc, 1970) and is given in Table 6.2. Filling the counter to a pressure of 7.6 kPa simulated a 2μm diameter sphere of unit density tissue when operating in normal mode with the conventional voltage configuration.

Table 6.2 *Elemental composition of tissue equivalent gas mixtures in percentages by weight.*

TE Mixture	H	C	N	O
Propane based (Srdoc, 1970)	10.3	56.9	3.5	29.3
Isobutane based (Schrewe et al., 1989)	10.3	59.2	3.5	26.9

Microdose distributions were obtained by operating the TEPC in both normal and helix modes in two well defined neutron fields of widely differing energies. As a test of pulse height resolution over a broad range of lineal energies, in–air measurements were performed in the p(66)/Be(40) neutron therapy beam of the NAC at an SAD of 150 cm and in a 10 × 10 cm^2 field. The 2.5 mm thick walled TEPC was irradiated with and without additional build–up provided by a TE cap of wall thickness 16 mm placed over the aluminium housing of the detector. Integrated charge from a transmission chamber located downstream from the target in the collimator head assembly served as beam monitor.

To determine the sensitive volume associated with the helix geometry the TEPC was exposed to monoenergetic neutrons of energy 2.3 MeV as the microdose distribution for this source exhibits a pronounced and easily discernible proton edge. The neutrons were generated via the $T(p,n)^3He$ reaction with 3.1 MeV protons from the Van de Graaff accelerator. Exposures were made in a scatter–free area with the counter positioned in–air at 0° and at a distance of 20 cm from the geometric centre of the tritium gas cell. During these measurements the integrated charge on the

target was used as a beam monitor for the exposures.

The timing characteristics of the commercial proportional counters were studied in a pulsed neutron beam at the neutron time–of–flight facility described in Chapter 3. A quasi–monoenergetic neutron field with a principal peak energy of 62.6 ±0.85 MeV was produced by bombarding a 1.1 mm thick Be target with protons of energy 65.3 ±0.2 MeV. The Q–value for the $^{9}Be(p,n)^{9}B$ reaction is –1.85 MeV (Ajzenberg-Selove, 1984) and a maximum energy loss of 1.70 MeV was calculated for the incident protons using the stopping power data of Andersen and Ziegler (1977). Separate measurements using the TEPC and CPC were performed with the detectors irradiated free in–air. In each instance full secondary charged particle equilibrium was ensured by placing customized build–up caps of the appropriate material and thickness over the aluminium housing of the detectors. Wall thicknesses of the TE and carbon (graphite) caps were 32 and 16 mm respectively. The CPC was similarly filled with the isobutane–based TE gas mixture at a pressure of 7.6 kPa. The detectors were positioned at a distance of 6 m from the target and orientated with the anode perpendicular to the incident beam direction. The spread in the neutron TOF at this distance was characterised with a neutron spectrometry system utilizing a 5 cm x 5 cm NE213 liquid scintillator that has been described previously (Binns and Hough, 1987).

Electronic System

To enable investigation of the timing response of the proportional counters data were acquired in multi–parameter mode. Each pulse height event registered by the counter is chronicled by its own TOF relative to the cyclotron RF. A schematic diagram of the electronic system used for pulse processing and data acquisition is

shown in Figure 6.1. The electronics for the three linear legs that convey the single event pulse height information are the same as previously described (Chapter 2) except that a delay module and a linear gate and stretcher (LGS) are inserted between each linear amplifier and the fast ADC (450 MHz clock rate). In addition there is a fast timing circuit that generates a start signal for the time–to–amplitude converter (TAC). To optimize time pick–off, an amplitude and rise time compensated timing unit (ARC) was employed. The ARC timer is designed to extract timing information from detectors that generate a wide range of pulse rise times. This is achieved by basing the timing signal on a fixed fraction of the initial portion of the pulse, negating the effect of any shape changes that may occur at a later time in the waveform (Chase, 1968). Otherwise the module works similarly to a constant fraction discriminator using a zero crossing technique of a synthesised pulse

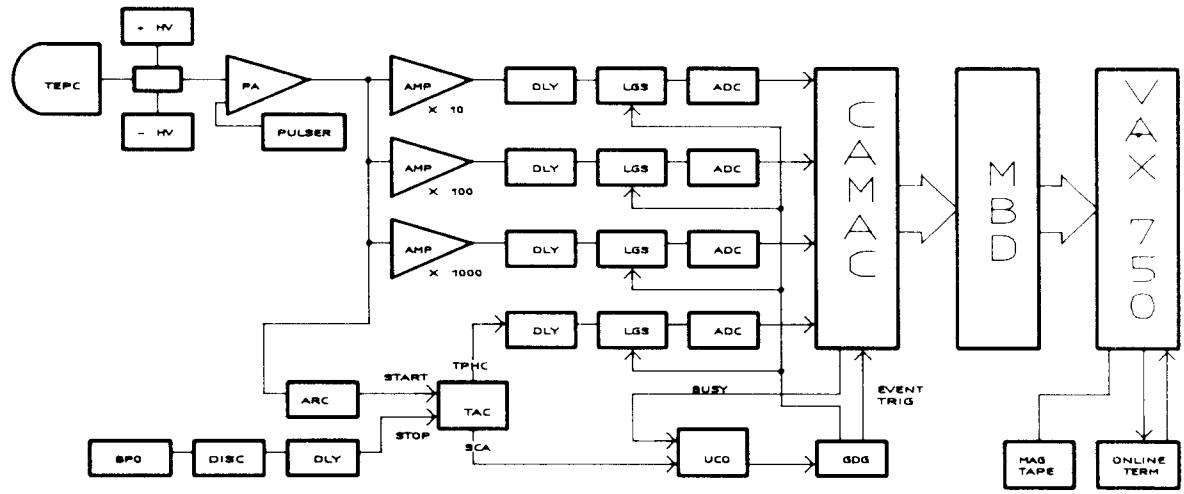

Figure 6.1 *Block diagram of the electronic system used for pulse processing and multi–parameter data acquisition. Index: ADC = analogue to digital converter; AMP = spectroscopy amplifier; ARC = amplitude and rise time compensated timing module; BPO = beam pick–off; DISC = 100 MHz discriminator; DLY = delay; GDG = gate and delay generator; HV = high voltage supply; LGS = linear gate and stretcher; MAG TAPE = magnetic tape drive; MBD = microprogrammed branch driver; ONLINE TERM = on–line terminal; PA = preamplifier; PULSER = pulse generator; TAC = time–to–amplitude converter; TEPC = tissue equivalent proportional counter; UCO = universal coincidence.*

to minimise timing errors caused by large fluctuations in the pulse height of the detector signals. The stop pulse for the TAC is provided by a delayed beam pick–off

(BPO) from the pulse selector of the cyclotron. The sequence of start/stop signals helps to minimise electronic dead time and results in a time reversal of the TOF spectrum.

Two outputs are furnished by the TAC. The time to pulse height conversion (TPHC) signal is an analogue output pulse proportional to the measured time interval between successive start and stop inputs and represents the TOF spectrum of all events registered from the detector. This is recorded as a separate pulse height parameter. The built–in single channel analyser (SCA) generates a logic output which is used to gate the four analogue signals of interest and provides the event trigger. The latter is a signal that indicates to the data acquisition system that an event has occurred and that the ADCs should be read out. The circuitry providing the event trigger and computer busy signals are shown separately in Figure 6.2 for clarity. The event trigger signal is sent to the CAMAC event trigger module which then initiates the event read–out cycle of the data acquisition process. During the read–out cycle a computer busy signal is generated (duration ~40 μs) that inhibits the gates on the LGS modules. The event rate was low (30 cps) and the overall electronic and computer dead times were considered negligible.

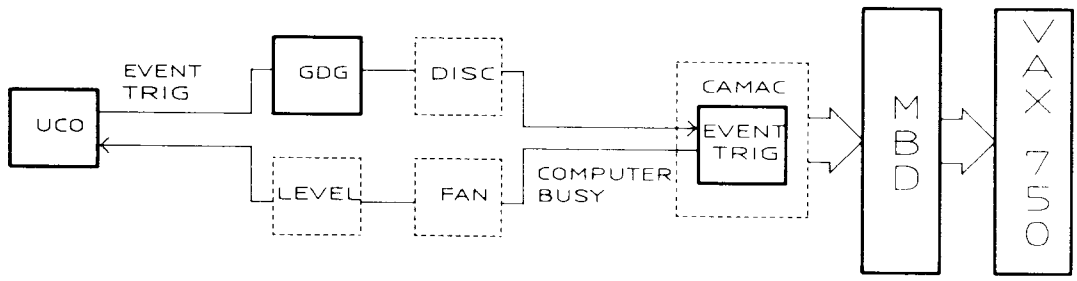

Figure 6.2 *Block diagram of the event trigger and computer busy signals omitted from Figure 6.1. Index: DISC = quad discriminator; EVENT TRIG = event trigger module; FAN = logic fan–in/fan–out; GDG = gate and delay generator; LEVEL = level adaptor; MBD = microprogrammed branch driver; UCO = universal coincidence.*

The proton beam current on the Faraday cup located in the beam dump was measured using a Brookhaven Instruments current integrator (BIC model 1000C). This instrument generates digital output pulses (5 μs width) with a frequency proportional to the accumulated charge. The various parameter settings are fed to the CAMAC current integrator module which in turn are recorded by the data acquisition system. The proton beam current was monitored throughout.

Computer interface

The electronic signal processing equipment is interfaced to the data acquisition computer by means of CAMAC (Computer Automated Measurements and Control). The digitised output from each of the ADCs is fed to a CAMAC interface module of in–house design. This module ensures complete control (enable, disable and clear) and the digitised data is read over the CAMAC dataway as a 16–bit word. The four ADC interface modules were slotted into a CAMAC crate containing a LeCroy 2551 CAMAC 12–fold scaler, CAMAC event trigger module and the current integrator status read–out module.

Data acquisition

The computer facility serving the experimental data room where the electronic modules are configured consists of two computers, namely a VAX–11/730 dedicated to on–line data acquisition and a VAX–11/750 used for off–line data analysis and general computing tasks. The computers are linked to one another via an Ethernet network and supplemented with magnetic tape drives. The interface between the VAX–11/730 and the CAMAC crate is a Bi–Ra microprogrammed branch driver (MBD–11). A full description of the computer hardware is given by Pilcher (1989).

During a run all events are recorded on magnetic tape (6250 bpi) on an event–by-event basis. This permits the experiment to be replayed and allows for timing corrections and the imposition of any software generated gates that may be desired in the off–line analysis. An on–line graphics terminal provided colour screen monitoring of recorded spectra.

Computer software

Data acquisition and subsequent off–line analysis were performed using the software package XSYS, the origins and structure of which are described elsewhere (Pilcher, 1989). Prior to the commencement of data acquisition the computer software is set up in three stages as follows: XSYS is initialised, followed by an allocation of computer memory to hold the required number of histograms (spectra) and gates. Thereafter the Data Acquisition Program is implemented and the Event Analysis Language (EVAL) code loaded.

Memory allocation

Global memory of 4800 pages (1 page = 512 bytes) was required for each experimental run (and replay) and a list of the histograms and gates used during data acquisition is given in Table 6.3. Data areas of 1024 channels were allocated to each of the three pulse height spectra (single event frequency distributions). The TOF parameter for all output events from the detector were recorded in a fourth one–dimensional data area of 512 channels. Three two–dimensional data areas of TOF (256 channels) versus pulse height (512 channels) were created to study the TOF spectra for each amplification stage. One–dimensional projections (512 channels) onto the TOF axis of data bound by linear gates set at different pulse heights were also possible. All data areas could be viewed on–line.

Table 6.3 *List of histograms and gates for data acquisition.*

Number of histograms	Size of histograms (channels)	Contents
3	1024	Histograms of pulse height events
1	512	Histogram of TOF spectrum
3	512	1–D projections of time spectra for gated pulse heights
3	512 x 256	2–D TOF vs pulse height
3	–	1–D gates for pulse height data

Data Acquisition Program (DAP)

The actual data acquisition was controlled by a sorting subprocess of XSYS called XSORT which reads both the Data Acquisition Program (DAP) and the Event Analysis Language (EVAL) files. The necessary CAMAC commands required by the branch driver (MBD) for crate initialisation, starting and stopping runs and for individual event reading were contained in the DAP file. Data were read event–by–event.

Event Analysis Language (EVAL)

The EVAL code controlled the incrementing of the histograms and operates by analysing the data on an event–by–event basis. Procedures such as gate setting requirements, simple arithmetic and logical manipulations (FORTRAN code may be called by the lower level EVAL) were included.

Results

Pulse height response in helix mode

Voltage settings with respect to the grounded wall of 480 V (anode) and −100 V (helix) produced the most promising time spectrum overall (see **Timing response in helix mode and voltage optimization**). To assess the feasibility of helix mode operation using this voltage combination, the resultant gas gain and pulse height resolution were examined in a high energy neutron beam.

Single event spectra were collected at the NAC neutron therapy facility where a well characterised source of fast neutrons was available (Binns and Hough, 1988). The pulse height information was recorded in single parameter form using the conventional data acquisition system. Figure 6.3 illustrates the similarity of dose distributions obtained with the TEPC when running at the optimum voltages in both helix (480 V/−100 V) and normal (590V/118V) modes. These lineal energy spectra were measured in–air and with full build–up and have not been extrapolated to lower lineal energies. To aid comparison the proton edges of the two spectra have been aligned and it can be seen that the dynamic ranges of the event sizes are comparable. Similar features associated with the different particle species emitted from the counter wall can be identified in both spectra but with the helix mode having a broader fast proton peak and less sharp edges associated with the slow proton and alpha components. In helix mode the active volume is restricted to an elongated cylinder concentric with the anode (Schrewe *et al.*, 1990) and contrasts in the character of the helix microdose spectrum are attributed to differences between the chord length distributions for an elongated cylinder and a sphere. The less pronounced cut–off edges for the proton and alpha components are in agreement with calculations for elongated or oblate cylinders (Birkoff *et al.*, 1970)

When measuring in helix mode at the chosen voltage settings, the data show that there is sufficient gas gain to provide the necessary charge amplification for the wide range of event sizes produced inside the sensitive volume . An adequate pulse height resolution is also realized over the extended range of lineal energies encountered in the 66 MeV proton generated neutron field.

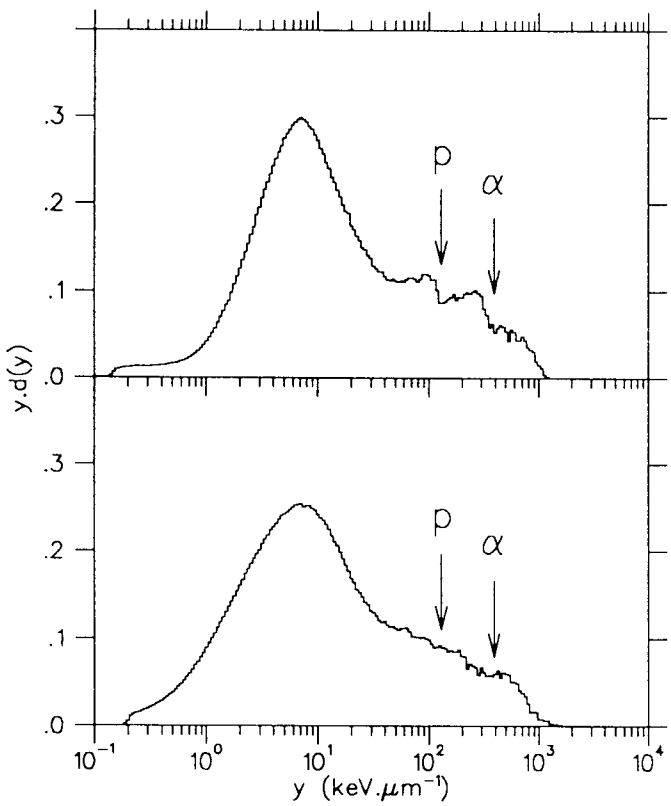

Figure 6.3 *Lineal energy spectra measured in–air with full build–up in the p(66)/Be(40) therapy beam. Normal mode (upper panel), helix mode (lower panel).*

Assessment of the sensitive volume

The negative bias on the helix in combination with the anode voltage govern the size of the sensitive volume when operating in helix mode. Verification of the exact size of the sensitive volume is needed to assess kerma from the single event spectra measured in helix mode, and in particular it was necessary to quantify the mass of gas (m) and the associated mean chord length ($\bar{\ell}$) for the assimilated volume. In a first approximation the active volume was assumed to be contained in an elongated

cylinder concentric with the anode, for which the mean chord length $\bar{\ell}$ is given by the Cauchy relationship

$$\bar{\ell} = \frac{2rh}{r+h} \tag{6.1}$$

where r is the radius and h the height of the cylinder (ICRU, 1983). This relationship assumes an isotropic irradiation of the cylinder within the spherical volume.

Figure 6.4 depicts equivalent spectra measured in the 2.3 MeV neutron beam with the TEPC operating in normal and helix modes. A correspondence between the distributions is again evident with the proton edge clearly discernible. This edge results from the maximum possible energy deposition by a proton inside the gas cavity of the counter and arises from a traversal of the longest chord length inside the sensitive volume of the detector. This path length and hence the energy loss is the same for both the sphere and cylinder (i.e. 2μm) and the correct position for the edge in terms of lineal energy depends only upon the effective mean chord lengths for the different geometries.

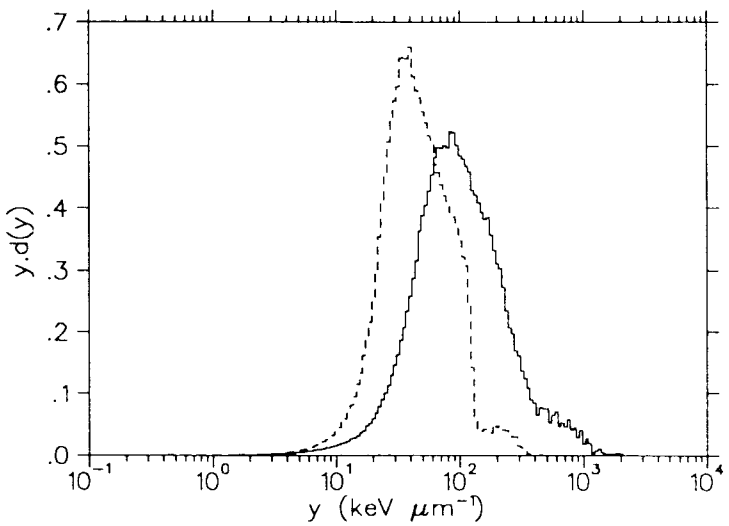

Figure 6.4 *Single event spectra measured with the TEPC in a 2.3 MeV monoenergetic neutron field with the counter operating in normal (– – –) and helix (——) modes. The proton edges are positioned according to the values detailed in Table 6.5.*

The dose per monitor count was determined from the normal mode measurement after positioning the proton edge of the single event spectrum at a lineal energy of 135 keV μm^{-1}. The spectrum measured in helix mode was then adjusted by adopting a particular elongation, keeping the length of maximum traversal constant, and then calculating the corresponding volume and mean chord length. By placing the proton edge in the appropriate lineal energy bin for each assumed elongation or volume, an absorbed dose per monitor count was obtained and compared with that determined in normal mode. The largest uncertainty associated with this procedure was positioning the proton edge in the designated lineal energy bin of finite width. Moving the edge of the normal mode spectrum by one bin induced a change in the measured absorbed dose of 5.6% and this figure was considered as a conservative estimate of the uncertainty in deducing the sensitive volume in helix mode. Table 6.4 lists the various values used to obtain the curve depicted in Figure 6.5 from which the unique mean chord length (and thus the cylinder volume) was determined.

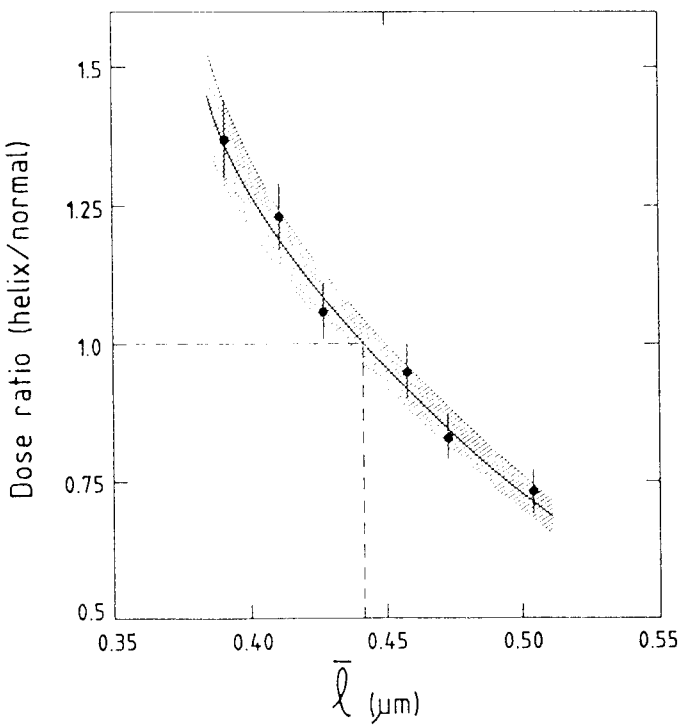

Figure 6.5 *Quotient of helix and normal mode doses as a function of the mean chord length* $\bar{l}$ *associated with cylinders of different elongation.*

Table 6.4 *Mean chord length ($\bar{\ell}$), volume (V) and maximum lineal energy for protons ($y_{p,max}$) calculated for cylinders with different elongation (ε) inside a 2 μm spherical cavity.*

ε	$\bar{\ell}$ (μm)	V (mm^3)	$y_{p,max}$ (keV μm^{-1})	$\frac{D_{helix}}{D_{normal}}$
4.50	0.391	74	460	1.37
4.25	0.411	82	438	1.23
4.00	0.427	92	422	1.06
3.75	0.458	104	393	0.95
3.50	0.473	116	381	0.83
3.25	0.504	133	357	0.73

Initial estimates of the radius and hence elongation (ratio of height to diameter) of the cylinder were based upon the reported diameter of 3.2 mm for the helical electrode (Oliver *et al.*, 1972). The effective diameter of the sensitive volume in helix mode was found to be 3.2 mm. An X–ray inspection of the counter and subsequent enquiry with the manufacturers confirmed that the actual diameter of the helix was only 0.8 mm. The extension of the sensitive volume beyond the physical boundary defined by the helix is attributed to a complex pattern of electric field potentials created between the anode, helix and wall. A summary of the parameters describing the assimilated volume is given in Table 6.5 together with that for the normal sphere. The correct positions on the lineal energy scale for the proton ($y_{p,max}$) and alpha ($y_{\alpha,max}$) edges were calculated using the accepted energy loss values ΔE_p (protons) and ΔE_α (alphas) for propane based TE gas (Pihet and Menzel, 1989; Schrewe *et al.*, 1988b). Calculations performed comparing the isobutane and propane

based mixtures indicated energy losses differing by only 0.6% which was not considered significant.

Table 6.5 *Definition of sensitive volumes in normal and helix modes.*

	NORMAL	HELIX
Geometry	Sphere	Cylinder
Volume (mm^3)	1033	97
Mass (mg)	162.7	15.3
Elongation	1	3.9
Mean chord length (μm)	1.33	0.44
Maximum traversal (μm)	2	2
ΔE_p (keV)	180	180
ΔE_α (keV)	526	526
$y_{p,max}$ (keVμm^{-1})	135	409
$y_{\alpha,max}$ (keVμm^{-1})	395	1195

Spectra calibration

To establish whether calibration of helix pulse height spectra was practicable in neutron beams where the cut–off edges are less pronounced, irradiations were performed in the therapy beam under strict dosimetric conditions. Figure 6.6 shows unextrapolated microdose distributions measured in the two different modes at the NAC neutron therapy facility. The measurements were carried out in a 10 x 10 cm^2 field at an SAD of 150 cm with the detector free in–air. As a further test of helix mode additional build–up was deliberately omitted in order to produce subtly different microdose spectra from those previously measured (Figure 6.3). The wall

thickness of 2.5 mm was sufficient to achieve 78% of the full dose build–up. Both dose normalised spectra exhibit reduced fast proton dose components compared with those measured at full build–up with the helix mode again reproducing the characteristic features of the normal mode measurement.

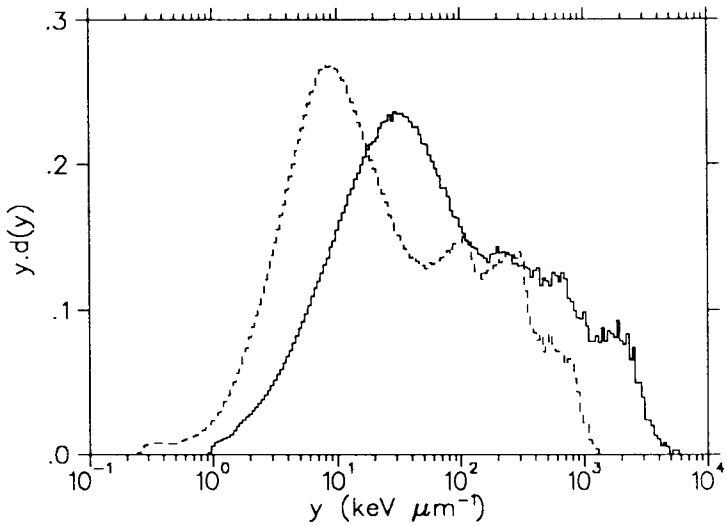

Figure 6.6 *Dose normalised microdose distributions obtained in the p(66)/Be(40) therapy beam with the TEPC operating in normal (– – –) and helix (——) modes. Irradiations were performed in–air without additional build–up and the spectra were calibrated using the proton edge method.*

Spectra were calibrated by positioning the respective proton edges according to the values detailed in Table 6.5 and the dose (in A–150 plastic) per monitor count was obtained with an overall uncertainty of approximately 8.2% (see Chapter 2). Prior to data collection the transmission chamber serving as beam monitor was calibrated against measurements using TE ionization chambers with full build–up. This practice is adopted at the NAC where the dosimetry protocol of Mijnheer *et al.* (1987b) is applied. The calibrated dose (in A–150 plastic) per monitor count was then corrected by 0.78 to allow for the lack of build–up during the microdose measurements. An uncertainty of 4.7% is associated with the absorbed dose determination to the A–150 wall of an ionization chamber when the tissue/A–150 kerma ratio is not applied (Broerse *et al.*, 1981).

Extrapolating the normal mode spectra to lower lineal energies increased the measured dose by 0.3% and gave a dose per monitor count that concurred with the

calibration value. The dose from the helix mode spectrum differed by only 1%, well within the estimated experimental uncertainties.

Table 6.6 *Comparison of average microdosimetric values obtained in normal and helix modes.*

	NORMAL	HELIX
$\bar{y}_F$ (keVμm^{-1})	7.24	16.40
$\bar{y}_D$ (keVμm^{-1})	90.9	262.6
$\bar{\varepsilon}_F$ (keV)	9.64	7.22
$\bar{\varepsilon}_D$ (keV)	120.9	115.5

Average values for the microdosimetric parameters $\bar{y}_F$ and $\bar{y}_D$ were determined for the two different volumes from the calibrated spectra and are presented in Table 6.6.

To facilitate a direct comparison between the two modes the average values were multiplied by the appropriate mean chord lengths to obtain the mean energy imparted per event $\bar{\varepsilon}_D$ and the frequency mean energy imparted, $\bar{\varepsilon}_F$. Assuming uncertainties of 10% and 6% in the experimental determination of $\bar{y}_F$ and $\bar{y}_D$ respectively (Waker, 1985), the $\bar{\varepsilon}_D$ values appear to correspond whereas the $\bar{\varepsilon}_F$ values differ significantly. This is in agreement with theory evaluating the equivalence of spherical and cylindrical volumes (Kellerer, 1981).

Time–of–flight

The TOF spectrum measured in the quasi–monoenergetic neutron beam with the NE213 liquid scintillator is presented in Figure 6.7. This detector is sensitive to both neutrons and photons and possesses good timing properties allowing distinct features to be discerned. Events in the time spectrum due to neutrons of nominal energy 62.6 MeV are identified by the sharp peak (FWHM = 3.8 ns) which predominates, followed by the continuous low energy tail resulting from nuclear break–up. During this measurement the pulse shape discrimination (n–γ identification) was set to allow a portion of the gamma events to be registered. The attendant gamma component is emitted in proton induced reactions in the Be target and precedes the primary neutron peak by 35 ns. The TOF spectrum was calibrated to a nanosecond scale by altering the delay between the start and stop pulses. The spectrum shift produced by the use of standard 50 and 100 ns delay line boxes yielded a time calibration of 0.38 ns per channel. In a TOF measurement the velocity v of a neutron of mass m is determined by the time t it takes to travel a distance L and can be calculated from the equation for kinetic energy

$$E_n = \frac{1}{2} mv^2 = \frac{1}{2} m(L/t)^2$$

which in the non–relativistic case simplifies to

$$t = 72.3\ L\ (E_n)^{-1/2} \qquad \text{(ns)}$$

where L is expressed in metres and E_n in MeV.

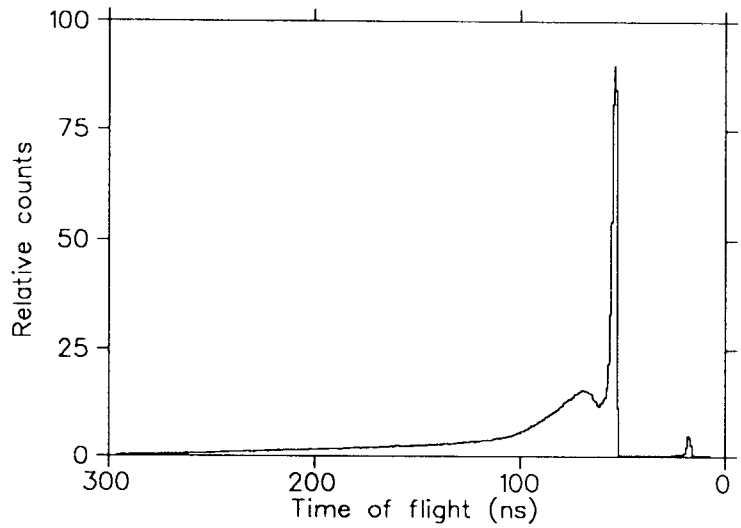

Figure 6.7 *TOF spectrum measured over a 6 m flight path for the NE 213 liquid scintillator in the 62.6 MeV quasi–monoenergetic neutron field. Events due to neutrons of the nominal energy are identified by the sharp peak (FWHM = 3.8 ns) which predominates. The attendant gamma component is seen preceding the primary peak by 35 ns.*

Timing response in helix mode and voltage optimization

When operating in helix mode an appropriate choice of voltages for the anode and helix was carefully considered. Arcing limited the voltage differential to 600 V and a series of voltage combinations was tested for timing resolution and gas gain. For the initial investigations of the timing response beamtime scheduling constraints did not permit setting up and tuning of the complete system (Fig. 6.1) and full multi-parameter data collection was not possible for the preliminary investigations of the timing response. Instead the TPHC output from the TAC was stored as single parameter data on an MCA and the detector pulses observed on an oscilloscope. As the pulse height information was not being retained in this instance, the rise time reject discriminator (a 0 to 10 turn potentiometer) on the ARC timer was set at 4.0. This excluded from the TOF spectra those small pulse height events expected to cause time slewing that would mask the true timing response from the TPHC output.

Figure 6.8 shows the results of TOF spectra measured with the TEPC operating at various applied bias settings. Initially the counter was operated with no voltage

applied to the helix and the anode voltage reduced to 528 V with respect to the grounded wall (Fig. 6.8a). This provided the same gas gain, measured with the internal calibration source, as when operating in normal mode. The TOF spectrum for this voltage setting is a broad single peak (FWHM = 61 ns) with no discernible detail. The slow inherent response is attributed to the time variations in pulse formation depending upon where the original ionization occurs within the spherical volume of the detector. Due to the different drift times required by the electrons to reach the collecting wire, events distant to the anode form pulses that are delayed in time relative to those occurring nearby which obscures the TOF information and produces a poorly resolved timing spectrum.

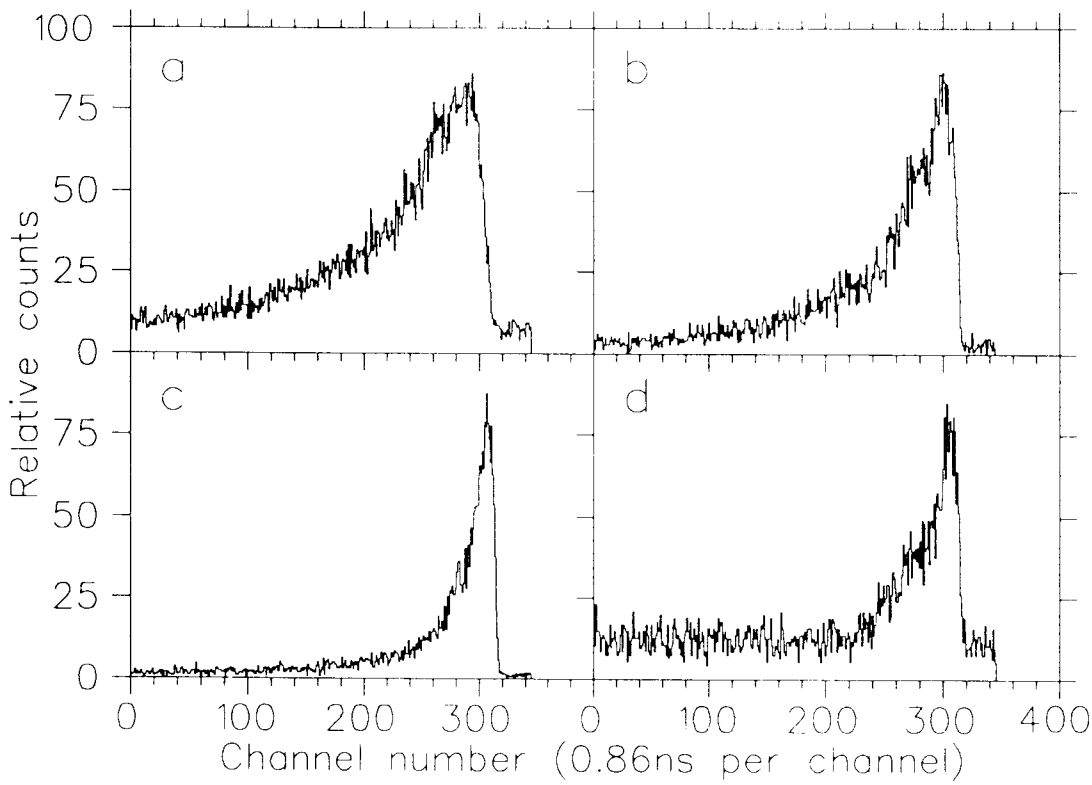

Figure 6.8 *TOF spectra measured over a 6 m flightpath with the TEPC operating at various applied bias settings in the 62.6 MeV quasi–monoenergetic neutron field. In this representation the abscissa scales are reversed. The voltages to the anode and helix were respectively (a) 528,0; (b) 480, −50; (c) 480, −100; (d) 380, −100.*

To reduce the size of the sensitive volume a negative voltage of –50 V was applied to the helix with the anode bias accordingly reduced to 480 V so as to maintain a similar differential of approximately 528 V with the wall again being held at ground potential. An improved timing response was apparent with the expected general form of a peak of nearly monoenergetic neutron events (FWHM = 21 ns) followed by a long low energy tail starting to become evident (Fig. 6.8b). Altering the helix voltage to –100 V appeared to improve still further the form of the TOF spectrum (Fig. 6.8c) although the actual width of the 'monoenergetic' peak appeared similar (FWHM = 22 ns). The combination used by Schrewe *et al.* (1990) of 280 V (anode) and –200 V (helix) was also applied but resulted in a very poor gas gain which was considered unacceptable. Measurements were however performed at a similar voltage differential (480 V) with settings of 380 V and –100 V for the anode and helix respectively but also resulted in a low gas gain (Fig. 6.8d).

The correlation between the timing performance of a TEPC and size of the detector has been demonstrated previously where a small cylindrical detector of 0.8 mm radius (Dicello, 1983) showed a measured timing response of 14 ns (FWHM) compared to that of 75 ns (FWHM) for a 6.4 mm radius sphere (Randers–Pehrson *et al.*, 1983).

TOF in helix mode

Timing characteristics of the 480 V (anode) and –100 V (helix) voltage combination were investigated in detail using multi–parameter data collection and without an artificially high setting on the discriminator of the time pick–off. The threshold was adjusted to include small pulse height events in the timing spectrum and was set just above the electronic noise level of the detection system (~ 0.6 mV). Figure 6.9 shows a comparison of TOF spectra obtained in the 62.6 MeV quasi–monoenergetic neutron

beam when operating the TEPC in normal and helix modes together with the spectrum from the NE213 detector. These TEPC distributions are composite TOF spectra encompassing the timing for the entire range of detector pulses.

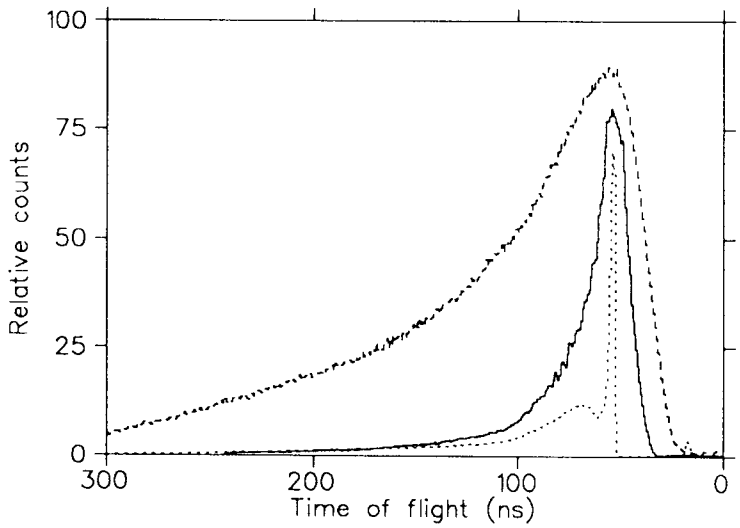

Figure 6.9 *Comparison of TOF spectra measured over a 6 m flightpath in the 62.6 MeV quasi–monoenergetic neutron field. TEPC operating in normal mode (– – –), FWHM = 73 ns; TEPC operating in helix mode (——), FWHM = 21 ns; NE213 liquid scintillator (· · ·), FWHM = 3.8 ns.*

The almost featureless asymmetric distribution (FWHM = 73 ns) for the conventionally operated TEPC is comparable in shape and width (FWHM = 75 ns) to that reported for a 20 MeV monoenergetic neutron beam (Randers–Pehrson *et al.*, 1983) and conveys little useful information about the character of the neutron beam. A distinctly narrower (FWHM = 21 ns) but still unstructured distribution was evident when operating the counter in helix mode where the assumed active volume is reduced to a cylinder surrounding the anode. The apparent loss of character for this helix measurement compared to the preliminary TOF spectrum obtained with the same voltage settings (Fig. 6.8c) is attributed to the lower discriminator setting on the ARC timer.

Amplitude walk (time slewing)

Following optimization of the intrinsic operation of the TEPC, the possible influence of external factors on the observed timing response was investigated. In particular

the effect of amplitude walk concomitant with time pick–off, derived from input pulses of variable amplitude as encountered in microdosimetry and hitherto ignored, was examined. The data for each amplifier stage were therefore inspected separately. Figure 6.10 depicts two–dimensional density plots of TOF relative to pulse height data collected in the three amplification stages (X10, X100, X1000). Scrutiny of the data in the medium gain amplifier (X100) showed two clusters or groups of data associated with photons and neutrons emanating from the target and properly separated in time. Clear separation between the two dose components has not been reported before in TOF studies with low pressure proportional counters and is indicative of the excellent overall performance of the counter. The characteristic curvature to the leading edge of each group becomes more pronounced at lower pulse heights and can be ascribed to amplitude walk or time slewing.

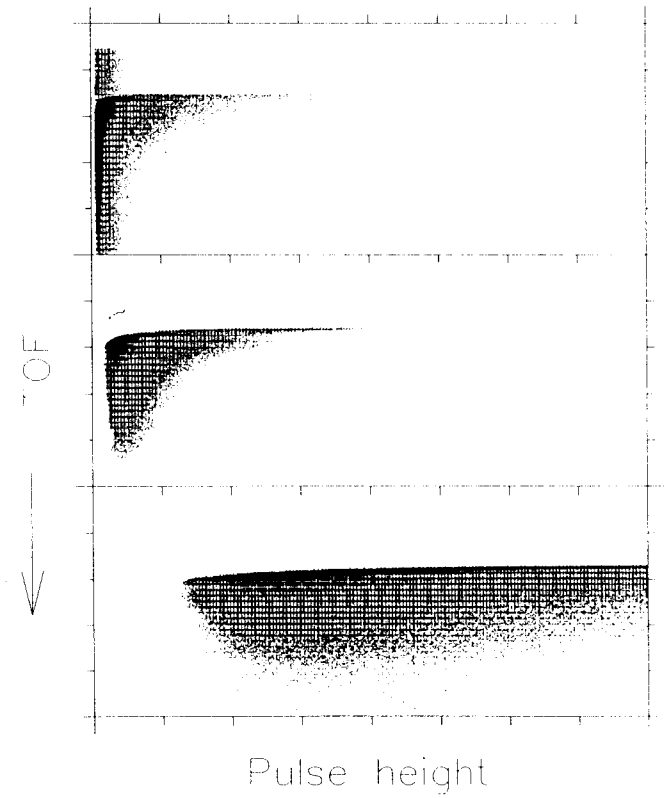

Figure 6.10 *Two–dimensional density plots correlating pulse height events processed by the low (upper panel), medium (middle panel) and high (lower panel) gain amplifiers with their flight times for the TEPC in helix mode.*

Other distinct features in the pulse height data were observed with increasing TOF and hence decreasing incident neutron energy. A reduction in the frequency of both small (high gain) and large (medium and low gains) pulse height events was evident.

This reflects a shift in the fast proton component towards higher values of lineal energy and smaller contributions from the heavy ion and alpha dose components as the neutron energy decreases.

When all pulse height events are projected onto the time axis, the observed timing resolution of the counter is adversely affected by time slewing. However, when a narrow band or window of pulse heights is selected at various positions on the pulse height scale and the data bound by the window then projected onto the time axis, the inherent timing capabilities of the TEPC are revealed. Two such projections made from the low (upper panel) and high (lower panel) gain data are shown in Figure 6.11.

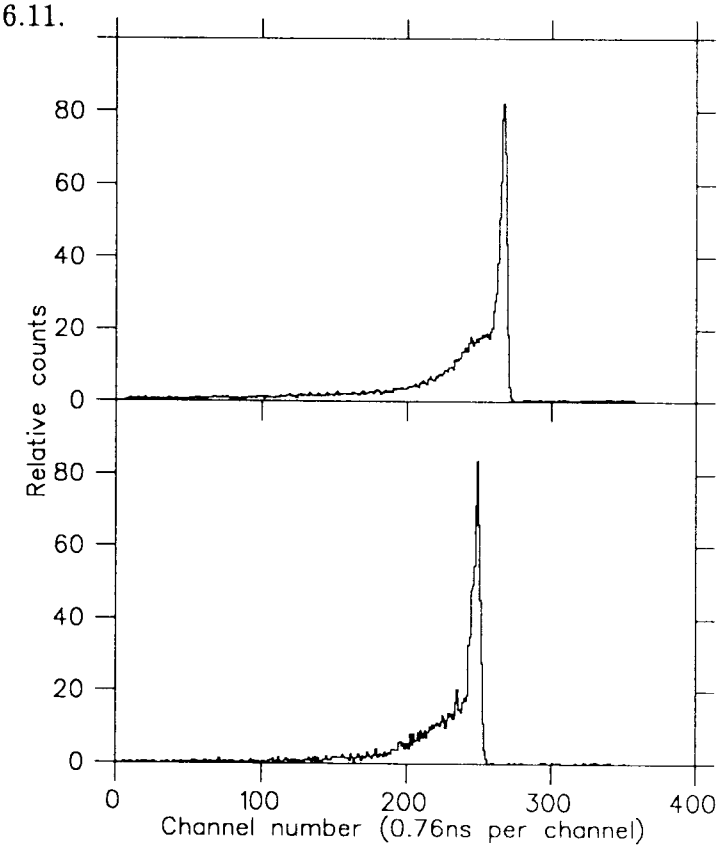

Figure 6.11 *Projections onto the time axis of thin slices of pulse height data detected by the TEPC in helix mode and registered in the low gain (upper panel) and high gain (lower panel) amplifiers. In this representation the abscissa scales are reversed. The measured resolutions (FWHM) of the monoenergetic peaks are 5.2 and 5.9 ns respectively.*

The respective FWHM of 5.2 ns and 5.9 ns are representative of what is found for the whole range of pulse heights. At smaller pulse heights there is an apparent deterioration in the shape of the TOF spectrum as illustrated in the lower panel where the projection was made just above the threshold of pulse height measurement.

The two cuts in Figure 6.11 exhibit structure comparable to that obtained with the NE213 detector and suggest that events can indeed be identified with a TEPC on a TOF basis.

Time slewing correction

Off–line compensation for time slewing was considered justified and the data for each gain setting separately adjusted according to the following procedure. At each gain the correct time position was ascertained by examining the time of arrival for the larger pulse height events. This provided different reference points in time depending upon the amplification stage. A smooth curve was then drawn by eye through loci given by the data points of first arrival for each pulse height bin and the time difference between the reference and slewed events determined. The data were then replayed, event–by–event, and each time slewed event corrected using the corresponding time increment. The spectra in Figure 6.12 show projections onto the time axis after correcting all the data points from the individual amplifiers for time slewing. Monoenergetic peak widths of between 7 and 8 time channels were obtained with a time calibration of 0.76 ns per channel giving a FWHM of less than 6 ns for each gain. Events associated with the nominal energy were now unambiguously identified and could be selected by setting a linear gate on these time spectra. The small peak in the panel of the high gain amplifier spectrum corresponds to the expected TOF for photons originating at the target.

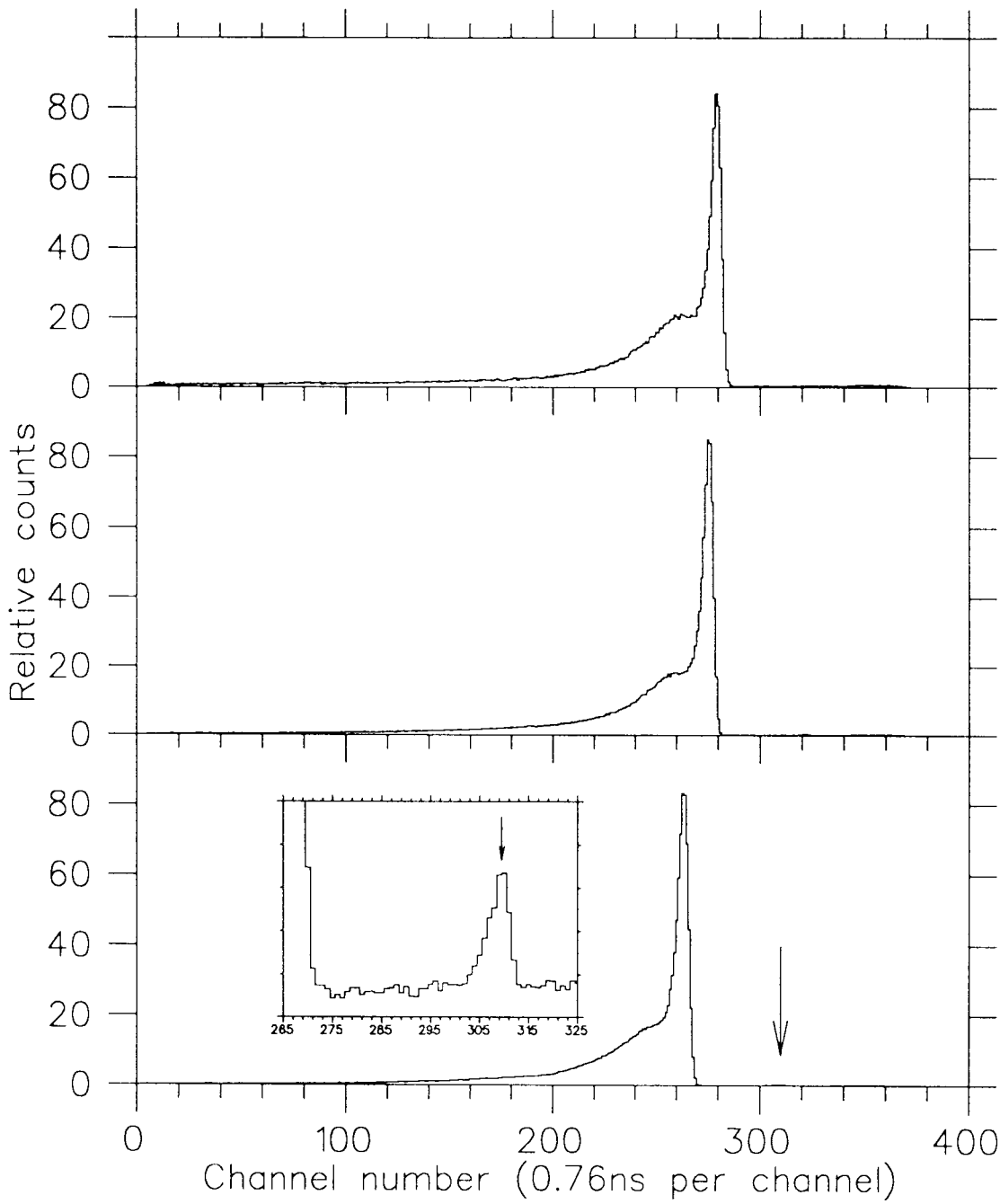

Figure 6.12 *Projections onto the time axis of all the pulse height data from the TEPC for the low (upper panel) medium (middle panel) and high (lower panel) gain amplifier after compensating for time slewing. The measured resolutions (FWHM) of the monoenergetic peaks are all less than 6 ns.*

Complementary CPC study

A complementary study under similar experimental conditions was performed with the CPC and comparable results obtained. The electrical characteristics of the CPC are nearly identical to the TEPC and the same voltage combination of 480 V (anode) and −100 V (helix) was applied. Using this counter electronic noise was slightly reduced and the discriminator on the ARC timer lowered accordingly (to ~0.4 mV). Figure 6.13 shows the composite TOF spectrum for the entire range of pulse heights and the two–dimensional density plots of TOF relative to pulse height for the individual amplifiers. Time slewing was again apparent on the well separated photon and neutron event clusters, and off–line correction was applied to give the TOF spectra for each gain stage depicted in Figure 6.14. The FWHM (<6 ns) of the monoenergetic peaks compare well with their TEPC counterparts but the low energy tails are less pronounced and do not extend to longer flight times. The lack of response of the CPC to lower energy neutrons (E_n<10 MeV) is ascribed to the various energy thresholds which need to be exceeded before the nuclear reactions can proceed (Del Guerra, 1976).

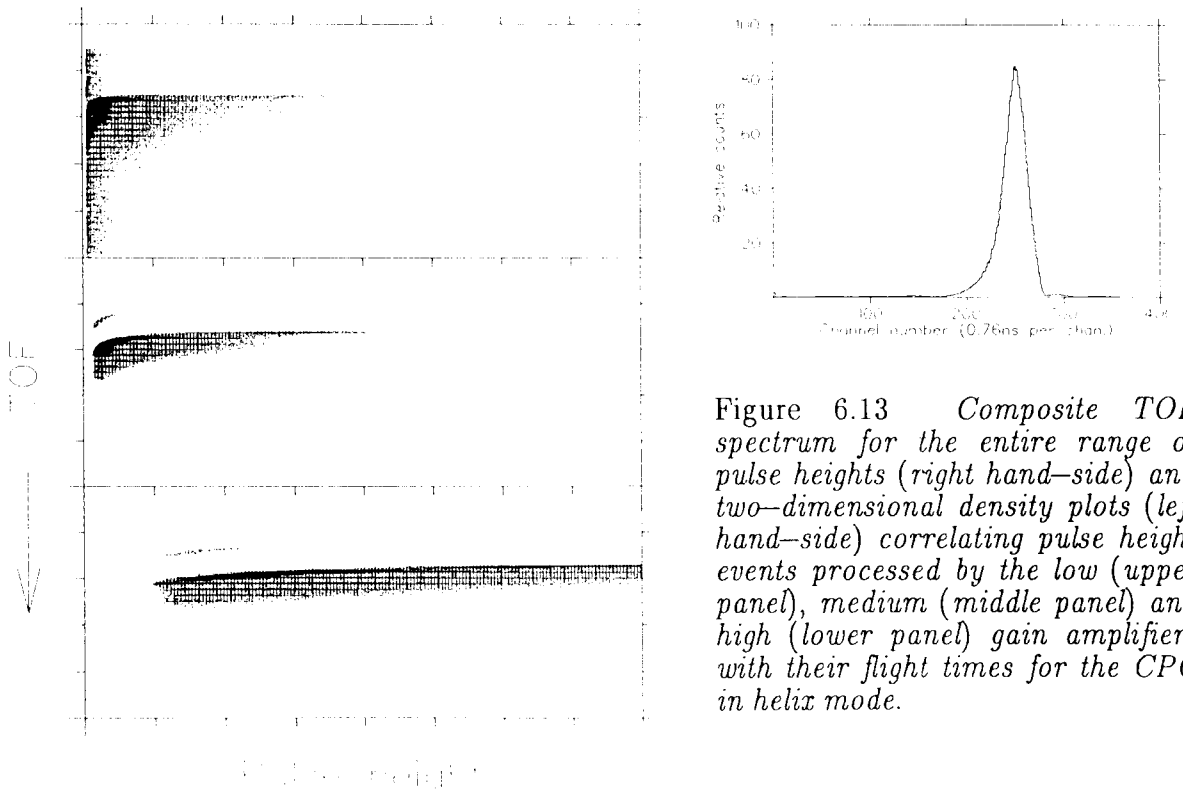

Figure 6.13 *Composite TOF spectrum for the entire range of pulse heights (right hand–side) and two–dimensional density plots (left hand–side) correlating pulse height events processed by the low (upper panel), medium (middle panel) and high (lower panel) gain amplifiers with their flight times for the CPC in helix mode.*

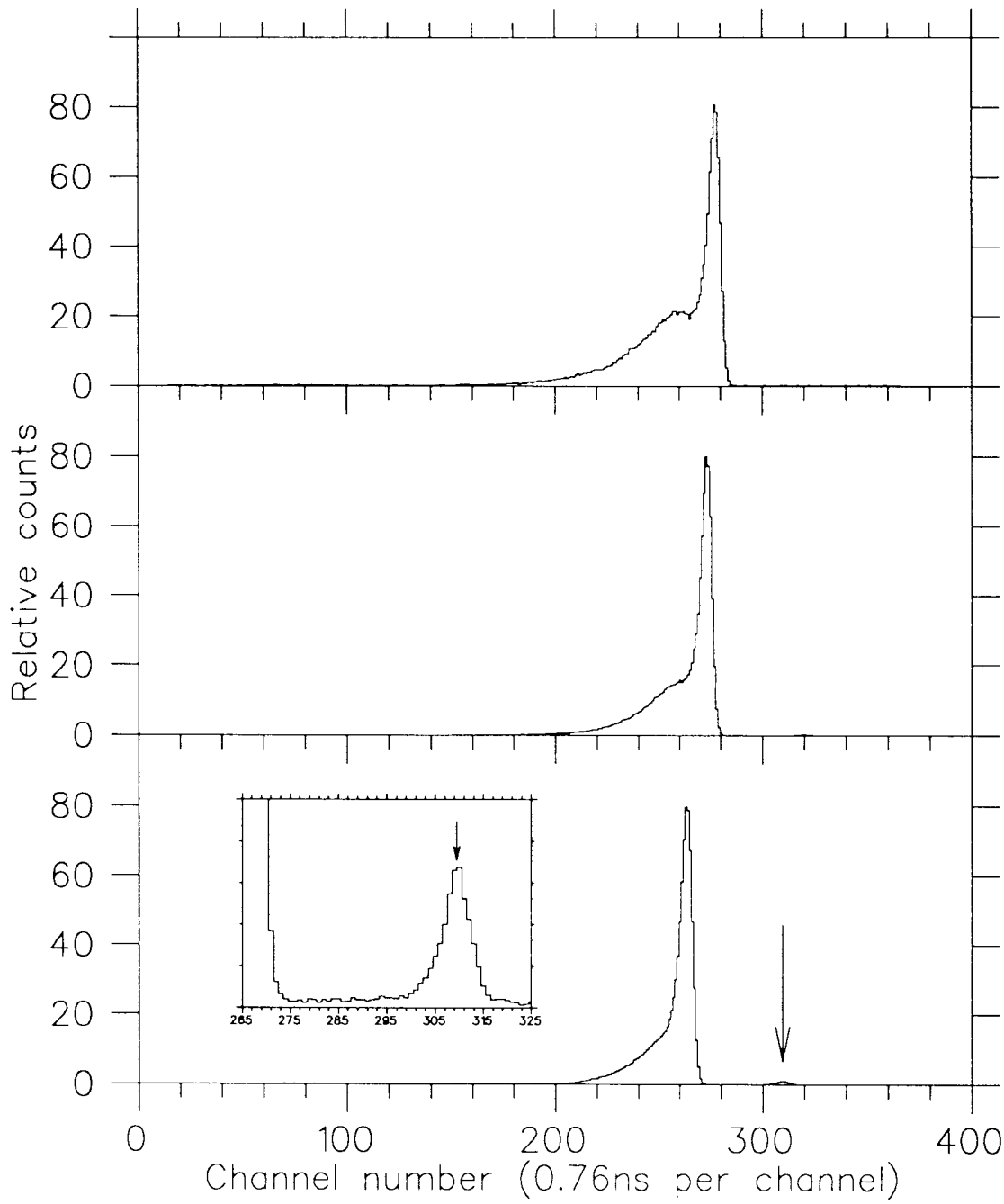

Figure 6.14 *Projections onto the reversed time axis of all pulse height data from the CPC for the low (upper panel) medium (middle panel) and high (lower panel) gain amplifiers after compensating for time slewing. The measured resolutions (FWHM) of the monoenergetics peaks are all less than 6 ns.*

A distinct change in shape of the low energy tail was also observed between the low and high gain time spectra of the CPC. This is because the high gain amplifier primarily registers events associated with the fast proton component of the microdose distribution that result from neutron interactions in the carbon wall of the counter. The principal $^{12}C(n,p)^{12}B$ reaction requires the least energy (Q–value –12.59 MeV) of all proton releasing reactions (Ajzenberg–Selove, 1985) and the diminished tail of the high gain TOF spectrum is attributed to the high energy threshold (13.63 MeV in the centre of mass frame) for proton events in the counter.

Discussion

In a high energy neutron field, spectrometry using TOF requires a detector which generates a fast signal that ideally varies little in shape and amplitude. The signals from commercial 1/2–inch diameter Rossi counters exhibit none of these traits as they usually produce slow pulses of variable shape spanning a wide dynamic range. The inferior timing characteristics observed with these counters are due to both intrinsic and extrinsic effects. Previous attempts to attain a practicable time response have concentrated on reducing the size of the sensitive volume without necessarily considering how best to derive the time pick–off and how related timing artefacts could impair the performance. (Randers–Pehrson *et al.*, 1983; Schrewe *et al.*, 1989). Whilst smaller detectors promise faster timing the problems of pulse shape and amplitude variations will still be apparent as these are related to the nature of the single event distributions in lineal energy.

The purportedly improved timing responses of low pressure proportional counters need to be viewed with some circumspection because of uncertainties associated with the measured microdose distributions. Randers–Pehrson *et al.* (1983) presented

time–correlated single event spectra which did not correspond well with conventional measurements and could not be satisfactorily calibrated. Similarly the description and subsequent use of a Rossi counter in helix mode (Schrewe *et al.*, 1989; Schuhmacher *et al.*, 1992) devote little attention to the actual microdose distributions obtained (in helix mode) and none are shown explicitly, nor are any TOF spectra given for high energy neutrons.

The present work however, has conclusively shown that major improvements in the timing performance of commercial microdosimeters can be achieved whilst still preserving adequate pulse height resolution. A different voltage combination from that originally described for helix mode (Schrewe *et al.*, 1989) was necessary to realize sufficient gas gain and pulse height resolution over the full range of lineal energies encountered in 66 MeV proton generated neutron fields. The optimised voltage settings allow reliable dosimetric data to be obtained from single event spectra measured in helix mode which are presented and shown to be equivalent to their counterparts measured in normal mode.

The smaller size of the sensitive volume in conjunction with the new cylindrical geometry prohibits those events originating at distant ionization sites from being registered and provides an inherently faster time response for the detector. This allows the use of an appropriate timing discriminator such as an ARC timer to provide genuine TOF information. This time pick–off device reduces timing uncertainties due to variations in pulse rise times and minimizes amplitude walk utilizing the technique of constant fraction timing. Time triggers derived by leading edge methods (Schrewe *et al.*, 1988a) are not suited to the large dynamic range of pulse heights common in microdosimetry and cannot accommodate a change in pulse rise–times without introducing an additional uncertainty in the measurement (Knoll, 1979).

A proper combination of detector volume, timing discriminator and multi–parameter data acquisition are essential for true time–resolved microdosimetry. Two–dimensional data displays of TOF relative to pulse height show the photon and neutron events generated at the target clearly separated in time for the most stringent TOF example envisaged, namely that of a 63 MeV generated neutron field. Previous studies in high energy neutron fields have failed to show photon and neutron related events resolved in time, even though the measurements were performed in beams of lower neutron energy where the difference in flight times between the two components was greater per unit distance travelled than those used in this study. In all instances amplitude walk cannot be eliminated completely but can be easily identified, as shown by the presented data where off–line compensation for time slewing is demonstrated for the first time.

The true timing capabilities of the helix mode configuration once revealed, enabled distinct structure associated with the incident energy spectrum to be discerned at all measurable pulse heights. Neutrons of nominal energy 62.6 MeV were identified in a peak of width 5.9 ns (FWHM). This compares favourably to the best timing response of 14 ns reported with a miniature TEPC in a 25 MeV neutron field (Randers-Pehrson *et al.*, 1983). Only with a comprehensive appreciation of the helix mode of operation and related pulse processing can single event spectra be reliably correlated in time. Direct assessment of the kerma associated with a high energy neutron of specified energy is now realizable for the first time and measurements performed at three different energies spanning the 20–65 MeV energy range are described in the following chapter.

CHAPTER 7

KERMA ASSOCIATED WITH HIGH ENERGY NEUTRONS

Introduction

In the energy range 20–65 MeV uncertainties still exist in the experimental values obtained for neutron kerma factors in the materials and elements of dosimetric interest (White *et al.*, 1992). Two experimental assessments using independent methods have been made but were unable to provide a direct measurement of the total kerma for selected monoenergetic neutrons. Adjustments to the data of between 40–50% were required to accommodate experimental inadequacies resulting from either an incomplete data set (Romero *et al.*, 1985) or contamination of the kerma measurement by extraneous contributions from low energy neutrons (Schuhmacher *et al.*, 1992; Schrewe *et al.*, 1992a).

The present study utilizing a TEPC and CPC operating in helix mode shows how the total kerma associated with a high energy monoenergetic neutron can be measured directly without the application of large correction factors. Optimization of the timing response of the detectors enables genuine energy spectrometry of the kerma related events on the basis of TOF. This overcomes the difficulties previously experienced in quasi–monoenergetic neutron distributions where kerma events due to neutrons other than those of the nominal energy are registered and extends the useful range of kerma assessments at specific neutron energies with low pressure proportional counters. The present data are the first reported microdose distributions measured for truly monoenergetic neutrons in the energy range 20–65 MeV.

The evaluation of kerma from a measurement with an ionization chamber or proportional counter requires knowledge of the energy dependent parameter $r_{m,g}$, the gas–to–wall dose conversion factor. A value of unity is usually appropriate for a homogeneous detector system where the gas filling has the same elemental composition as the wall material of the counter. Whilst a TEPC with TE gas is considered homogeneous, values of $r_{m,g}$ for the heterogeneous combination of a graphite walled proportional counter filled with TE gas need to be determined. Comparison of the measured monoenergetic microdose spectra obtained under identical irradiation conditions with the TEPC/CPC pair of detectors provides such an evaluation. Similarly the kerma ratio of carbon to A–150 was assessed and compared with other reported values to demonstrate the viability of this method for future neutron kerma factor evaluations.

Materials and Methods

To augment the measurements already described at 62.6 ±0.9 MeV (Chapter 6) additional irradiations at two different energies were carried out at the neutron TOF facility. Collimated neutron fields with monoenergetic peak energies of 25.5 ±1.8 MeV and 42.0 ±1.2 MeV were generated by bombarding the 1.1 mm thick Be target with protons of incident energy 29.1 ±0.1 MeV and 45.0 ±0.2 MeV respectively. Heat dissipation in the solid target restricted the maximum proton beam intensities in each instance to 2.5 μA (25.5 MeV), 3.5 μA (45.0 MeV) and 5μA (62.6 MeV). Dose assessments were determined with the TEPC and CPC under the same experimental conditions described in Chapter 6.

The build–up cap wall thicknesses used in the 25.5 and 42.0 MeV beams were respectively 6 and 13 mm for the TEPC, and 1.5 and 5.5 mm for the CPC. These

cap thicknesses ensured secondary charged particle equilibrium for each irradiation. Single event spectra were measured with each counter operated in the two different modes. Conventional single parameter pulse height data were obtained for the different energies with the counter wall maintained at ground potential and voltages of 590V and 118V applied to the anode and helix. Thereafter measurements were performed with the counters operating in helix mode by changing the voltage settings to 480V (anode) and –100V (helix). TOF information was recorded only in helix mode using multi–parameter data acquisition on an event–by–event basis. This permitted replay of the data to correct for time slewing caused by the ARC timer and allowed the imposition of software gates as desired.

The measured microdose distributions were calibrated by identifying the cut–off edges associated with the proton and alpha components. Spectra were adjusted until the most prominent edge was in the correct position on the lineal energy scale calculated from the maximum possible energy loss and mean chord length values (Table 6.5). The photon fraction of the total measured kerma was evaluated from the normal mode spectra and subsequently subtracted to give the neutron only kerma for each measurement. In normal mode the duration of a run was approximately 1 hour whereas time correlated helix mode measurements required continuous run times of between 11 and 20 hours. Temperature control of the experimental vault ensured a constant temperature (22 ±2° C) throughout. Gas gain stability was monitored using the internal alpha source by operating the counters in normal mode before and after each helix run.

Results

Data extrapolation (helix mode)

In helix mode the gas gain was sufficient to measure event sizes as small as approximately 0.5 keV (see Figure 6.6). The time–correlated measurements however, were subject to a higher pulse height threshold imposed by the discriminator setting on the ARC timer which was adjusted to eliminate electronic noise. This threshold was highest for the 62.6 MeV run with the TEPC where the smallest event size recorded was approximately 3 keV. To compensate for the loss of pulse height information, spectra acquired in multi–parameter mode were extrapolated to lower event sizes by fitting pulse height data measured under similar irradiation conditions in helix mode but using the conventional single parameter acquisition system. Pulse height data measured by the high gain amplifier with the TEPC in the 62.6 MeV quasi–monoenergetic neutron field are illustated in Figure 7.1. The solid curve shows a projection onto the pulse height axis of all registered events in the TOF spectrum recorded in multi–parameter mode. The spectrum extending to smaller pulse heights (broken curve) was obtained from an independent single parameter measurement. Depending upon experimental conditions the dose accommodated by the extrapolation procedure varied between 0% (CPC at 25.5 MeV) and 26% (TEPC at 62.6 MeV) of the total evaluated. In the most extreme instance matching of the

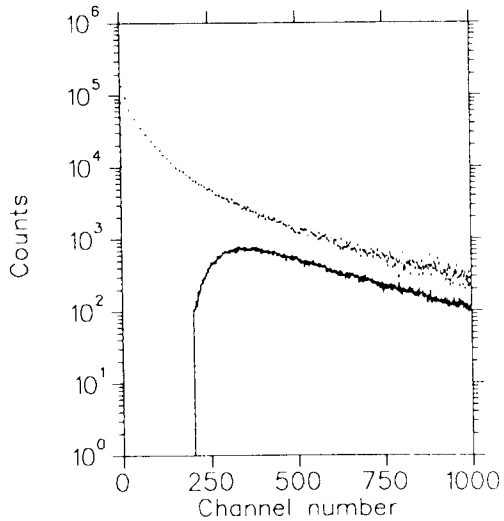

Figure 7.1 *Pulse height information registered by the high gain amplifier with the TEPC in the 62.6 MeV quasi-monoenergetic neutron field using the multi–parameter* (——) *and conventional* (· · ·) *data acquisition systems. The conventionally acquired data is displaced by a decade for clarity and was used to extrapolate the multi-parameter data acquired in helix mode.*

single parameter and time–correlated spectra was estimated to introduce an overall uncertainty of less than 2.6% to the total dose determinations.

TEPC microdose distributions

Microdose distributions for the three quasi–monoenergetic neutron fields measured with the TEPC operating in both normal (upper panel) and helix (lower panel) modes are shown in Figure 7.2. The helix mode spectra were obtained from projections onto the pulse height axis of all registered events in the TOF spectrum and have been extrapolated to lower event sizes as described above.

The calibrated spectra have been normalised to unit dose and exhibit the same changes with energy, irrespective of the operating mode. The distributions are dominated by large fast proton components that migrate to lower lineal energies as the incident neutron energy increases. At the lower beam energies where a greater proportion of the incident proton energy is lost in the target, the microdose spectra have more slow protons per unit dose. Above the proton edge the alpha and heavy ion contributions appear to differ little in shape. These findings are consistent with those previously reported where thicker Be targets were bombarded with protons of incident energies 35, 45 and 65 MeV (Heintz *et al.*, 1977; Amols *et al.*, 1977).

Fractional photon dose contributions of 2.9 ±0.3% were assessed for the 25.5 MeV and 42.0 MeV beams with a slightly smaller value of 2.2 ±0.2% for the 62.6 MeV beam.

CPC microdose distributions

Dose normalized microdose distributions measured with the CPC in the three different quasi-monoenergetic neutron fields are shown in Figure 7.3. A good correspondence between the normal (upper panel) and helix (lower panel) mode spectra is apparent with more dramatic changes noted in the character of the

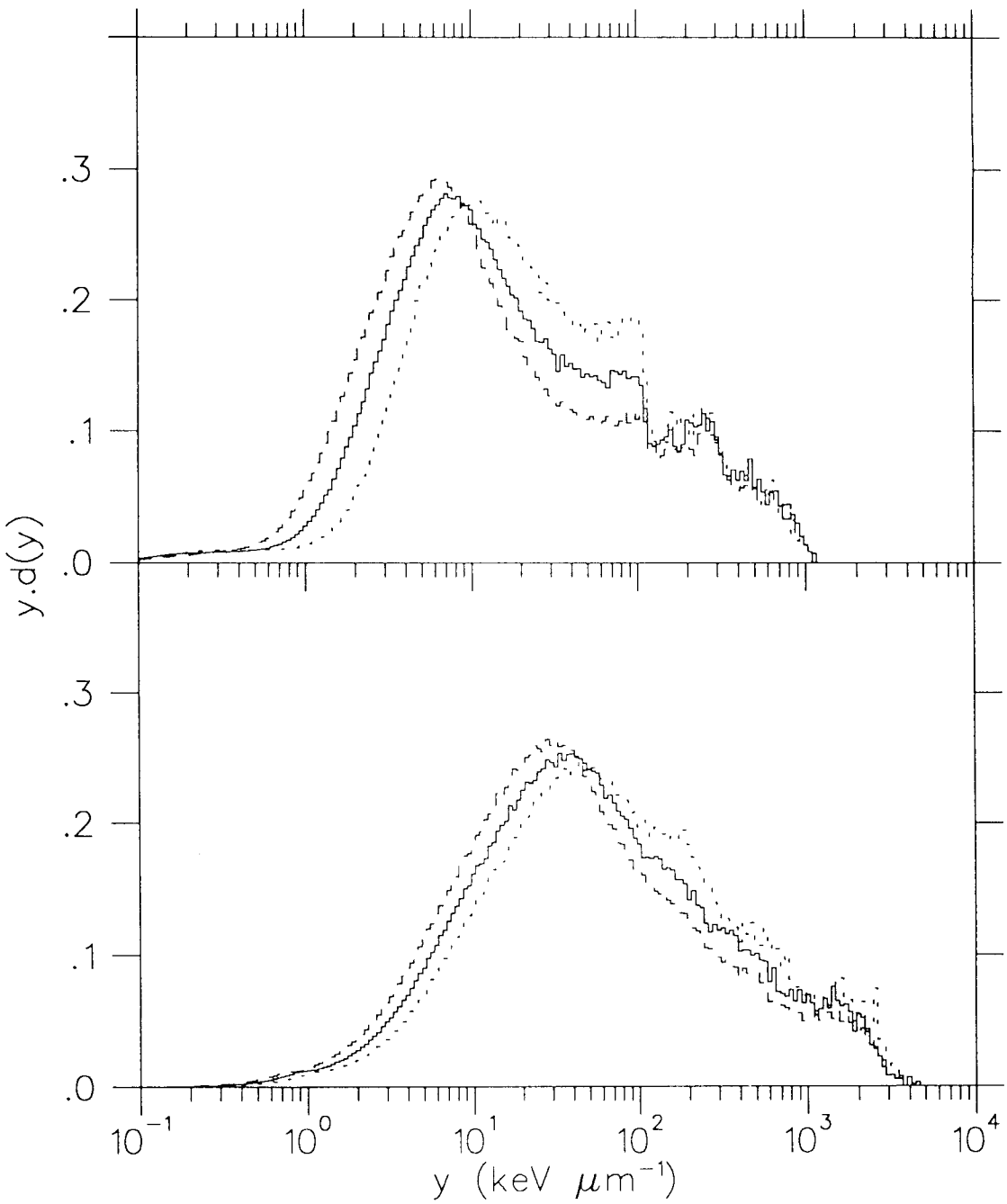

Figure 7.2 *Normalised microdose distributions measured with the TEPC in normal (upper panel) and helix (lower panel) modes for three different quasi-monoenergetic neutron fields of nominal peak energies 25.5 (···), 42.0 (——) and 62.6 (- - -) MeV.*

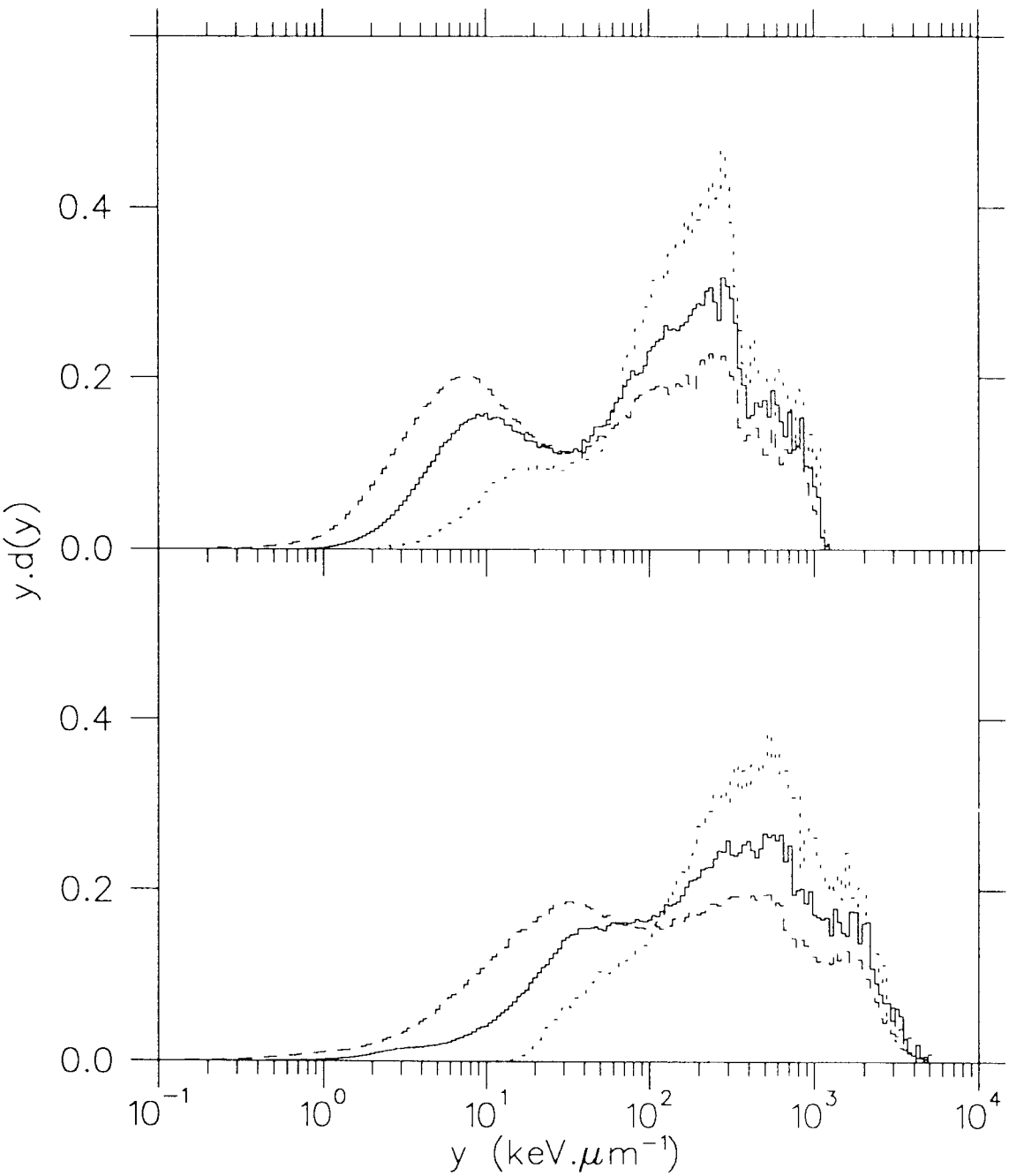

Figure 7.3 *Normalised microdose distributions measured with the CPC in normal (upper panel) and helix (lower panel) modes for three different quasi-monoenergetic neutron fields of nominal peak energies 25.5 (···), 42.0 (——) and 62.6 (- - -) MeV.*

distributions with varying energy than those observed for the TEPC. At all energies the alpha particle and heavy ion dose components can be clearly identified. The most striking feature is the presence of a marked contribution resulting from (n,p) reactions in the carbon wall at higher neutron energies. The fast proton peak is seen to increase in magnitude and migrates to lower values of lineal energy as the incident neutron energy increases. These spectra concur with those measured in similar neutron fields (Menzel *et al.*, 1988).

Measured absorbed dose for high energy neutrons

Off–line compensation for the observed time slewing was applied to the time–correlated data which were replayed event–by–event with software gates set to embrace the principal energy for each TOF spectrum. Pulse height data with a TOF falling within the window were selected and modified dose distributions obtained. Figure 7.4 (upper panel) shows the full ungated TOF spectrum for the quasi–monoenergetic beam using the CPC in the 25.5 MeV beam with the gated monoenergetic events identified by the hatched area. In this representation the abscissa scale is reversed. The corresponding dose distributions are also depicted (lower panel) and are normalised to provide the neutron kerma per monitor count for the gated monoenergetic neutrons relative to the ungated quasi-monoenergetics. Similarly Figure 7.5 shows spectra measured with the TEPC in the 42.0 MeV beam and Figure 7.6 those obtained in the 62.6 MeV beam with the CPC.

The TOF spectra are all consistent with those measured using the NE213 liquid scintillator and reflect the change in character of the generated quasi–monoenergetic neutron energy distributions with the principal peak becoming narrower as the

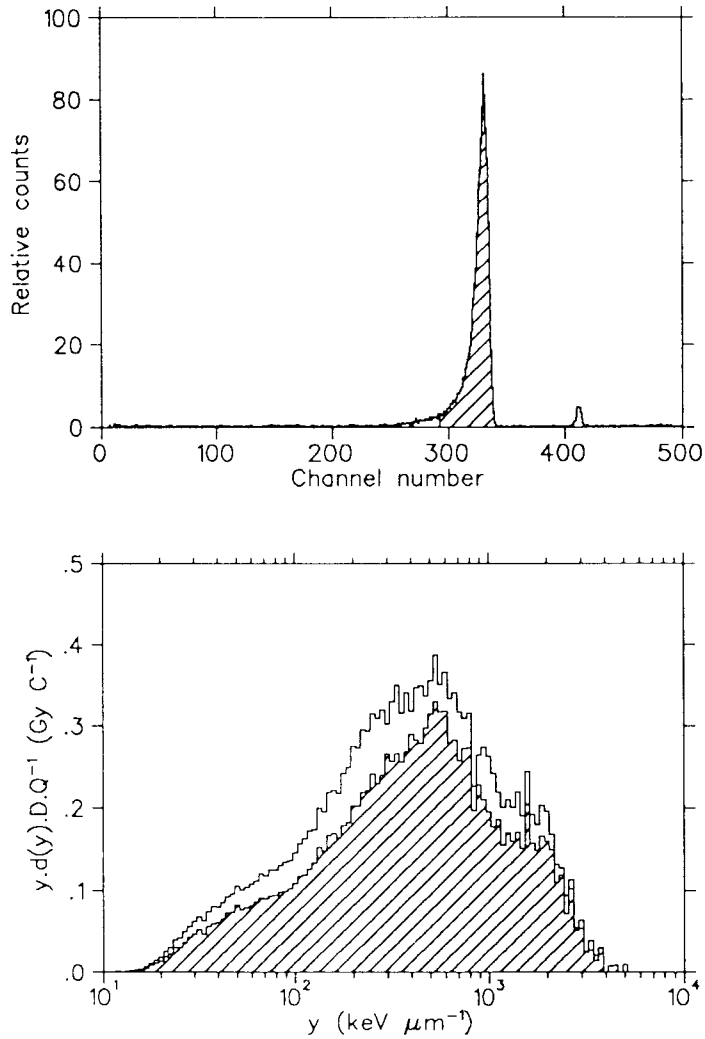

Figure 7.4 *TOF spectrum corrected for time slewing (upper panel) and microdose distributions normalised to relative neutron fluence obtained in helix mode (lower panel) with the CPC in the 25.5 MeV quasi–monoenergetic neutron field. The hatched areas delineate selected events of the nominal neutron energy.*

incident proton energy increases. Differences between the ungated and gated microdose distributions in both area (dose) and shape also become more apparent with increasing neutron energy. The gated monoenergetic 62.6 MeV microdose distribution measured with the CPC (Figure 7.6) exhibits a prominent fast proton contribution such that the characteristic shape of the spectrum more closely resembles that which might be expected of a TEPC rather than a CPC. This again illustrates the importance of the (n,p) reaction on carbon for dose assessments at higher neutron energies.

Calibration of each of the quasi–monoenergetic dose distributions was performed prior to the setting of TOF gates. Comparison of the measured doses expressed per monitor count for the normal and helix mode distributions (Figs 7.2 and 7.3) showed

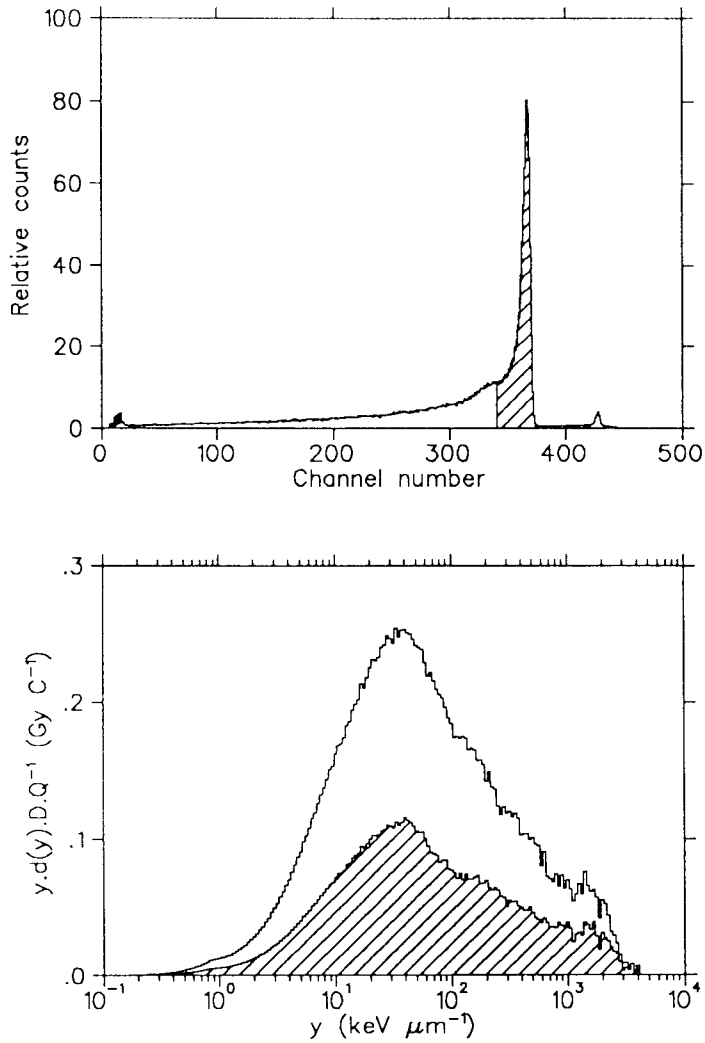

Figure 7.5 *TOF spectrum corrected for time slewing (upper panel) and microdose distributions normalised to relative neutron fluence obtained in helix mode (lower panel) with the TEPC in the 42.0 MeV quasi-monoenergetic neutron field. The hatched areas delineate selected events of the nominal neutron energy.*

good agreement and corresponded within 2% for each energy. Table 7.1 lists the neutron dose per monitor count obtained in helix mode for the ungated quasi–monoenergetic and gated monoenergetic distributions. The lower energy limit (threshold) for each gate setting spanning the principal neutron peak is also included together with the fractional neutron dose contribution from the peak relative to that for the entire quasi–monoenergetic distribution. This fractional proportion of the dose is always greater for the CPC than the TEPC as the carbon counter is insensitive to the lower energy neutrons in the quasi–monoenergetic distributions. The results also indicate a smaller fractional dose contained within the principal energy peak of the quasi–monoenergetic distributions as the bombarding proton energy is increased. This is consistent with the recent findings of Schuhmacher *et al.*, (1992) and Schrewe *et al.* (1992a), performed in quasi-monoenergetic neutron beams

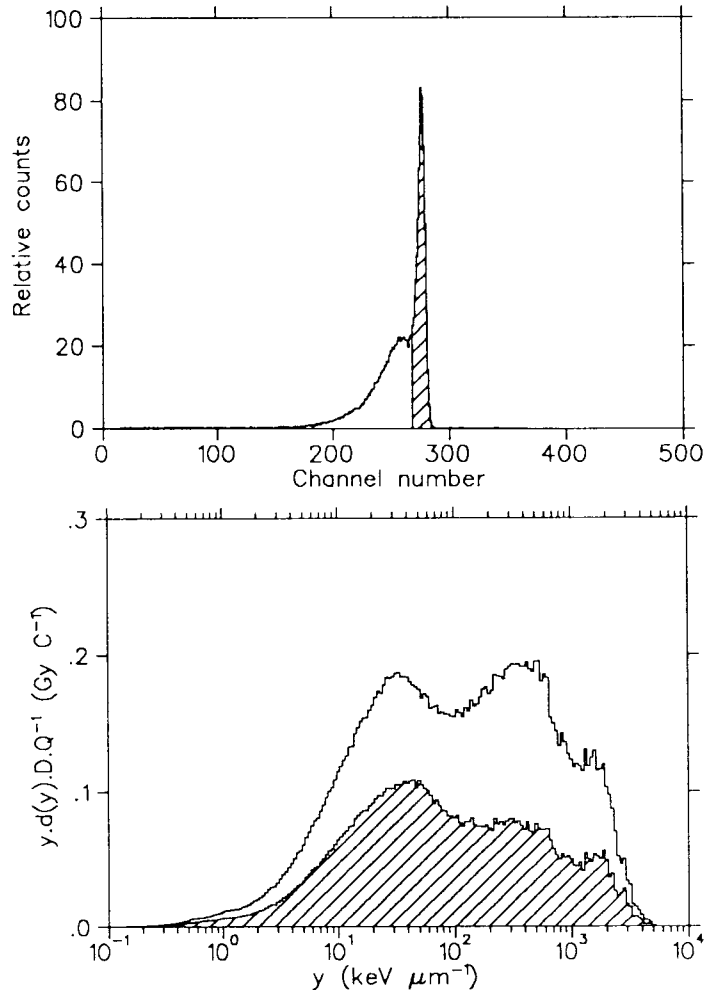

Figure 7.6 *TOF spectrum corrected for time slewing (upper panel) and microdose distributions normalised to relative neutron fluence obtained in helix mode (lower panel) with the CPC in the 62.6 MeV quasi–monoenergetic neutron field. The hatched areas delineate selected events of the nominal neutron energy.*

Table 7.1 *Neutron doses measured in the sensitive volume and expressed per monitor count for the TEPC and CPC under indentical irradiation conditions in three quasi–monoenergetic neutron fields.*

TEPC				
E (MeV)	Gate threshold (MeV)	D_{quasi} ($cGyC^{-1}$)	D_{mono} ($cGyC^{-1}$)	D_{mono}/D_{quasi} (%)
25.5	16	128.19	72.72	57
42.0	33	129.71	58.68	45
62.6	50	141.62	60.95	43
CPC				
E_n (MeV)	Gate threshold (MeV)	D_{quasi} ($cGyC^{-1}$)	D_{mono} ($cGyC^{-1}$)	D_{mono}/D_{quasi} (%)
25.5	16	56.26	43.26	77
42.0	33	67.01	40.32	60
62.6	50	93.12	45.31	49

similarly generated by bombarding a 2 mm thick Be target with protons of various incident energies ranging from 31.9 to 71.2 MeV.

Gas–to–wall dose conversion factor, $r_{m,g}$

Gas–to–wall dose conversion factors for a TE gas filled CPC have previously been determined using the ionization yield spectra measured with both a TEPC and CPC under identical irradiation conditions (Menzel *et al.*, 1988). The method assumes that the dose contribution above the proton edge in the TEPC distribution results only from neutron interactions with carbon atoms in the A–150 plastic and that the $r_{m,g}$ for the TEPC with TE gas filling is unity.

Spectra were normalised to relative neutron fluence using the beam monitor counts and the CPC measurements scaled down to the percentage of elemental carbon in A–150 plastic (0.776). The ratio (TEPC/CPC) of the dose integrals above the proton edge for each pair of measurements then gave the $r_{m,g}$ value for the CPC in that particular neutron field. Values were determined at each of the three nominal energies employing identically gated paired microdose spectra. To aid comparison with published data, values were also obtained using ungated helix and normal mode quasi–monoenergetic spectra. These are presented in Table 7.2 where an overall uncertainty of ±6% is assumed (Pihet and Menzel, 1989). Utilizing data for quasi–monoenergetic neutron beams over the energy range 25.5 to 62.6 MeV yields a constant $r_{m,g}$ for the CPC with the isobutane based TE gas filling and is in agreement with those previously reported using propane based TE gas (Menzel *et al.*, 1988).

Table 7.2 *Gas–to–wall dose conversion factors for the graphite counter with a TE gas filling. Values determined by Menzel et al., (1988) at similar energies have been included.*

E_n	$r_{m,g}$			E_n	$r_{m,g}$
(MeV)	Normal	Helix	Monoenergetic	(MeV)	(Menzel *et al.*)
25.5	0.84	0.83	0.80	27.8	0.85
42.0	0.85	0.83	0.80	39.7	0.83
62.6	0.84	0.83	0.88	60.3	0.84

Values determined with gated monoenergetic spectra, whilst consistent with these findings up to 42 MeV, appear to increase at higher neutron energies. In this energy range calculations of $r_{m,g}$ using stopping power data in conjunction with measured microdose spectra also indicate this trend (Pihet *et al.*, 1992b). The values from the monoenergetic data are consistent with those of 0.794 ±0.036 at 27 MeV and 0.802 ±0.045 at 39 MeV recently deduced by Schuhmacher *et al.* (1992).

Ratio of carbon to A–150 kerma

The kerma per monitor count was determined for each gated monoenergetic spectrum by multiplying the measured dose by the appropriate $r_{m,g}$ value given in Table 7.2. An $r_{m,g}$ value of unity was assumed for the TEPC for each energy (Pihet *et al.*, 1992b). The kerma per monitor count measured with the CPC relative to that of the TEPC was then calculated for each of the three energies. No corrections for neutron scattering and attenuation in the walls of the build–up caps were applied. Overall uncertainties associated with the results are considerably reduced when examining kerma ratios, with the major source of error being calibration of the microdose

distribution. This uncertainty was conservatively estimated as 5.6% for each spectrum.

The kerma ratios are plotted as a function of neutron energy in Figure 7.7 together with other experimental values (Romero *et al.*, 1985; Schuhmacher *et al.*, 1992, Schrewe *et al.*, 1992a) and three theoretical curves for E_n>20 MeV. Carbon, nitrogen and oxygen kerma factors calculated by Alsmiller and Barish (1977), Dimbylow (1982) and Brenner (1983) were used together with published hydrogen kerma factors (Fleming, 1974; Bassel and Herling, 1977) to obtain the theoretical curves. Romero *et al.* (1985) have quoted typical uncertainties of 2–3% for their results, but this only accounts for the fraction of kerma that was measured in the experiment. The uncertainties associated with their total kerma values are undoubtedly larger and the errors surrounding their corresponding kerma ratios are probably more comparable with those reported in this study. As the true uncertainties for the Romero data

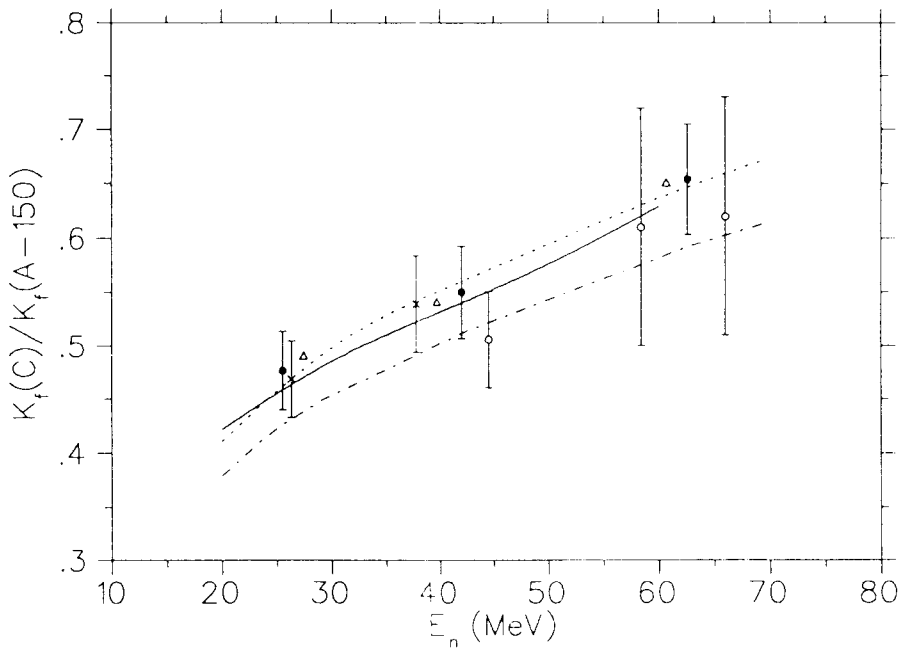

Figure 7.7 *Kerma ratio of carbon to A–150 plastic as a function of neutron energy. Values from this work* (•) *are presented with the experimental data of Romero et al., 1985* (Δ); *Schuhmacher et al., 1992* (x); *and Schrewe et al., 1992a* (o). *Theoretical curves are also shown from Alsmiller and Barish, 1977* (---), *Dimbylow, 1982* (——) *and Brenner, 1983* (—·—).

remain speculative, error bars for their plotted values have been omitted from the figure.

The kerma ratios derived from the time gated microdose spectra in conjunction with the determined $r_{m,g}$ values concur with other published data using different techniques. The results exhibit the same general trend as predicted by calculations and most closely approximate the curve of Alsmiller and Barish.

Discussion

Whilst neutron kerma factors can be predicted theoretically, large uncertanties exist in the nuclear model calculations because of incomplete data sets used as input for the energy range above 20 MeV. Experimental determination of kerma factors has been undertaken but the methods employed have been far from ideal as the actual kerma assessments were either incomplete or suspect due to contamination by low energy neutrons.

Romero *et al.* (1985) selecting monoenergetic neutron events measured only the partial kerma from secondaries with masses $A \leq 4$. The heavy ion contribution was estimated by applying sum rules relating the double differential cross sections, obtained from the inclusive measurements of the separate charge particle spectra, to the total non–elastic cross sections. Depending upon the element and neutron energy, corrections of between 13 and 40% were necessary. These corrections also accommodated the energy threshold of the experiment (4 MeV) below which no cross section data were measured.

Schuhmacher *et al.* (1992) were able to measure the total kerma for A–150 plastic

and carbon using proportional counters but were nevertheless obliged to make corrections of 30–50% because the assessments were contaminated by a large low energy neutron component. In their evaluation it was not possible to identify the kerma from either the contaminating neutrons or the neutrons of interest. To account for the ensuing kerma contamination corrections were principally derived using known kerma factor values in the 10–20 MeV region in combination with measurements of the spectral neutron fluence. The expressed uncertainty for the applied kerma factors was between 5.1 and 7.5% (Pihet *et al.*, 1992b) but the spectral fluence obtained with the liquid scintillator NE213 was considerably influenced (±30%) by the experimental threshold employed which did not extend to low neutron energies. The kerma for neutrons of energy less than 10 MeV was determined by TOF spectrometry with the TEPC and CPC operating in normal mode. The actual timing resolution obtained is not stated, nor are TOF spectra shown and the ability to unambiguously identify neutron events of a specific energy is considered questionable. At a distance of 9 m the times of arrival for neutrons with energies 39 and 10 MeV are 104 ns and 182 ns respectively. The time difference of 78 ns between the two energies is comparable to the 77 ns time interval between the high energy neutrons and a photon emanating from the target. Schuhmacher *et al.*, (1992) do not show photons separately resolved from the neutrons which, if indicative of the timing resolution that prevailed, suggests there is no justification for assuming that 10 MeV neutron events were distinguished from 39 MeV events on the basis of neutron TOF. In view of these potentially large sources of error the stated overall uncertainties for the assessed kerma per monitor count of between 4.3 and 7.2% appear highly optimistic and the agreement with Romero *et al.* (1985) possibly fortuitous.

Similar measurements were performed by Schrewe *et al.* (1992a) at neutron energies between 44.5 and 66.0 MeV. The reported value at 58.4 MeV is from the work of

Menzel *et al.* (1988) where no account of spectral neutron fluence was made. Moreover the cap material used in the measurement by Menzel *et al.*, (1988) was not A–150 plastic but polyethylene, which can be expected to provide a markedly higher kerma response (see **Build–up**, Chapter 4). The correction for low energy contamination at 66.0 MeV is dependent upon the kerma factor derived at 58.4 MeV and needs therefore to be viewed with caution. This probably explains the large quoted uncertainty for the 66 MeV data point and emphasises the shortcomings in this approach at higher neutron energies.

Verification of the reported kerma factors is essential if these values are to be accepted with the confidence required by clinical neutron dosimetry. The advantages of integral kerma measurements in kerma factor assessments with low pressure proportional counters manufactured from different wall materials was recognised (DeLuca *et al.*, 1984; Menzel *et al.*, 1984, Bühler *et al.*, 1985) and has contributed to a revised set of carbon kerma factors below 20 MeV which differ significantly from the previously accepted values (Caswell *et al.*, 1988). Whilst there are inherent uncertainties associated with the use of gas filled proportional counters such as knowledge of the $\overline{W}_n/W_c$ value for the counter gas and values for the gas–to–wall dose conversion factors $r_{m,g}$, the principal constraint on the method at higher energies is the absence of pure monoenergetic neutron sources.

Energy spectrometry of kerma related events on the basis of TOF overcomes this difficulty and enables a direct assessment of $r_{m,g}$ for the heterogeneous combination of graphite counter filled with isobutane based TE gas. Values of $r_{m,g}$ are energy dependent and essential for accurate kerma determinations. Utilizing quasi–monoenergetic neutron beams the present data yielded a constant $r_{m,g}$ whereas values obtained with gated monoenergetic spectra indicate an increase at higher

neutron energies. Calculations using various nuclear models predict an increase in the ratio of carbon to A–150 kerma factors for increasing neutron energy (Schrewe *et al.*, 1992a) with differences becoming less between the total responses of the CPC and TEPC. This then implies that the CPC acts more "tissue equivalent like" at higher incident neutron energies and that $r_{m,g}$ should approach unity. The gated monoenergetic microdose distribution measured with the CPC at 62.6 MeV with its pronounced proton dose component appears consistent with this premise as the characteristic shape resembles what might be expected from a TEPC. An analysis of the overall uncertainties associated with $r_{m,g}$ was not considered here, as the initial aim was to illustrate the value of true monoenergetic microdose data. In particular an oversimplification may be the assumption that the dose contribution above the proton edge in the TEPC measured distributions results only from neutron interactions with carbon atoms. The A–150 plastic also contains 5.2% oxygen and 3.5% nitrogen by weight and neutron interactions with these atoms can be expected to contribute to the measured response of the TEPC at higher energies. Calculations show the significance of the kerma factors for the respective elements (Behrooz and Watt, 1981) and recent measurements have illustrated the similarity in the ionization yield spectra measured for oxygen and carbon (Schrewe *et al.*, 1992b). In gated high energy monoenergetic beams a more suitable approximation might be to incorporate the nitrogen and oxygen by summing the proportions of carbon, nitrogen and oxygen in A–150 plastic with their respective percentage weights multiplied by an assumed kerma factor for each element relative to that of carbon. Neutron interactions with carbon atoms in the TEPC spectra would then be responsible for the fraction of the measured dose above the proton edge given by 0.776 divided by the weighted sum. If equal kerma factors for the three elements are chosen as an extreme example then the evaluated $r_{m,g}$ values would be reduced by approximately 11%. This would directly affect the kerma ratios obtained in this study by placing them close to the prediction of Brenner.

Nevertheless the feasibility of time–resolved microdosimetry using commercial Rossi–type proportional counters has been demonstrated. Direct measurement of kerma associated with high energy neutrons is possible with a single detector and microdose spectra associated with truly monoenergetic neutrons can be used to derive carbon to A–150 plastic kerma ratios that concur with theoretical predictions and other experimental values. By eliminating those procedures and methods that are needed to account for events registered by the detector other than those of interest will help to improve the overall accuracy with which integral kerma measurements can be performed with low pressure proportional counters at selected neutron energies.

CHAPTER 8

SUMMARY

Clinical dosimetry demands that the delivered absorbed dose to the target volume be specified with an accuracy of ± 3.5% regardless of the radiation modality used. In the hope of enhancing the efficacy of fast neutron therapy this work investigates the two largest obstacles confronting this objective for a p(66)/Be(40) beam. Firstly the problem of heterogeneous beam quality was addressed using microdose distributions which revealed changes in beam potency that were considered clinically significant. In the second half of the study TOF techniques were successfully applied employing commercial Rossi counters to enable a direct assessment of the total kerma associated with neutrons of a specific energy in the interval 20–65 MeV.

A thorough microdosimetric investigation of the p(66)/Be(40) therapy beam was performed with a tissue equivalent proportional counter. The measured lineal energy spectra and derived averages were observed to change for different irradiation conditions pertinent to therapy. Using the parameter y* as an indicator of radiation quality, variations in the potency of the beam were quantified with spatial position and field size in a water phantom, and in the dose build–up region measured in–air.

A 6% decrease in y* when moving to greater depths in–phantom was attributed solely to changes in character of the neutron component and appears independent of field size. The slight increase in the photon dose fraction does not play a role in the observed changes. Conversely increasing field size leads to an overall enhancement of 3% in beam effectiveness where an amelioration of the neutron component following scattering is tempered by the growing photon dose fraction. A similar interplay

between the high and low LET components was also evident in the penumbral region when moving across the lateral plane of a collimated field. Studies in the build–up region demonstrated the value of identifying individual components that contribute to the total absorbed dose. Reduced doses in the build–up region are shown to result from a smaller proton dose relative to the high LET ($y>140$ keV μm^{-1}) component. Compared to a position at full build–up the beam is 24% more effective at a depth of 1.3 mm.

To accommodate these quality changes in the prescription of absorbed dose, the concept of effective dose was invoked and elementary expressions proposed to assess this quantity. The measured y^*–values are employed to calculate a range of weighting factors which were normalised to unity at a selected reference position. Effective dose D_{eff} was then derived in terms of the conventionally measured total dose D_t as a function of depth, field size and lateral position. Whilst the discrepancy between D_{eff} and D_t was of little clinical consequence when moving across the lateral plane of the field and through the penumbra, changes with depth and field size appeared to merit further consideration. As illustration a conventional 4–field treatment plan to irradiate a symmetrically located $10 \times 10 \times 10$ cm^3 tumour in the pelvic region was prepared and compared to that obtained when the total dose input data was replaced by effective dose. A 4% reduction in the dose to the tumour volume was apparent for the effective dose calculation. In the clinical situation where fractionated doses are delivered this discrepancy could be accentuated. If the noted variations in beam quality are ignored they will undermine attempts at achieving the desired clinical accuracy in the physical specification of absorbed dose.

To facilitate a direct assessment of the total kerma associated with high energy neutrons investigations were performed in pulsed beams of quasi–monoenergetic

neutrons. The timing characteristics of commercial proportional counters routinely used in microdosimetry were studied to allow energy spectrometry of the recorded events utilizing the technique of TOF. A proper combination of detector volume, timing discriminator and multi–parameter data acquisition proved essential. After accounting for amplitude walk significant improvements were achieved whilst maintaining an adequate pulse height resolution over the extended range of lineal energies encountered in a high energy neutron field. Operating in helix mode the tissue equivalent and carbon proportional counters exhibit inherent timing responses (FWHM<6 ns) that compare favourably with that of an NE213 liquid scintillator (FWHM=3.8 ns). Distinct structure associated with the incident energy spectrum is discernible and enabled the unambiguous selection of energy deposition events resulting from neutrons of the nominal energy.

Time–correlated microdose spectra were measured in three different quasi-monoenergetic neutron fields with principal peak energies of 25.5, 42.0 and 62.6 MeV. The time gated spectra are the first reported microdose distributions for truly monoenergetic neutrons in this energy range. The gas–to–wall dose conversion factor for the TE gas filled carbon counter was evaluated from the data so obtained and appeared to increased from 0.8 to 0.88 in the energy range investigated. Subsequently the kerma ratio of carbon to A–150 plastic was determined and the results found to concur with other published data using different techniques.

REFERENCES

Ajzenberg–Selove F. (1984). Energy levels of light nuclei A = 5–10. Nuclear Physics **A413**, 1–168.

Ajzenberg–Selove F. (1985). Energy levels of light nuclei A = 11–12. Nuclear Physics **A433**, 1–158.

Alsmiller R.G. and Barish J. (1977). Neutron kerma factors for H, C, N, O and tissue in the energy range 20–70 MeV. Health Phys. **33**, 98–100.

Amols H.I., Dicello J.F., Awschalom M., Coulson L., Johnsen S.W. and Theus R.B. (1977). Physical characterization of neutron beams produced by protons and deuterons of various energies bombarding beryllium and lithium targets of several thicknesses. Med. Phys. **4** (6), 486–493.

Andersen H.H. and Ziegler J.F. (1977). Hydrogen stopping powers and ranges in all elements. In: The stopping and ranges of ions in matter Vol. 3 (J.F.Ziegler, Ed.) Pergamon Press, New York, U.S.A.

Barendsen G. W., Walter H.M.D., Fowler J.F. and Bewley D.K. (1963). Effects of different ionizing radiation on human cells in tissue culture. III. Experiments with cyclotron accelerated alpha–particles and deuterons. Radiat. Res. **18**, 106–119.

Bassel R.H. and Herling G.H. (1977). Energy transfer to hydrogen by neutrons from 30 to 100 MeV. Radiat. Res. **69**, 210–212.

Beach J.L. and Milavickas L.R. (1982). Microdosimetric measurements of radiation quality variation in homogeneous phantoms irradiated by fast neutron beams. Med. Phys. **9**, 52–59.

Beauduin M., Gueulette J., De Coster B.M., Gregoire V., Octave–Prignot M., Vynckier S. and Wambersie A. (1989). Radiobiological intercomparisons of fast neutron beams used in therapy. Proceedings of the EORTC–Heavy Particles Therapy Group Meeting, Munich, October 1987. Strahlenther. Onkol. **165**, 263–267.

Behrooz M.A. and Watt D.E. (1981). Kerma factors for neutrons of 14 MeV to 60 MeV in elemental H, C, N and O. Radiat. Prot. Dosim. **1** (4), 291–297.

Bewley D.K., McNally N J and Page B.C. (1974). Effect of the secondary charged–particle spectrum on cellular response for fast neutrons. Radiat. Res. **58**, 111–121.

Bewley D.K. (1989). The physics and radiobiology of fast neutron beams. Adam Hilger, Bristol, England.

Binns P.J. and Hough J.H. (1987). Spectral energy measurements in a fast neutron therapy field. Nucl. Inst. Meth. **A255**, 330–333.

Binns P.J. and Hough J.H. (1988). Lineal energy measurements in two fast neutron beams: d(16)+Be and p(66)+Be. Radiat. Proc. Dosim. **23**, 385–388.

Binns P.J. and Hough J.H. (1992). Consideration of radiation quality in treatment planning with p(66)/Be(40) neutrons. Int. J. Radiat. Oncol. Biol. Phys. **24**, 975–981.

Binns P.J., Hough J.H. and Simpson B.R.S. (1992). Time–resolved microdosimetry in a quasi–monoenergetic neutron beam. Radiat. Prot. Dosim. **44**, 67–71.

Birkhoff, R.D., Turner J.E., Anderson V.E., Feola J.M. and Hamm R.N. (1970). The determination of LET spectra from energy–proportional pulse–height measurements. I. Track–length distributions in cavities. Health Phys. **18**, 1–14.

Böhm L., Gueulette J., Jones D.T.L., Beauduin M., Vynckier S., De Roubaix S., Yudelev M., Slabbert J.P. and Wambersie A. (1990). Radiobiological intercomparison of two clinical neutron beams using the regeneration of mouse intestinal crypts. Strahlenther. Onkol. **166**, 242–245.

Botha A.H., Conradie J.L., Roels L.M.M., Fourie D.T., Kritzinger J.J., Reitmann D., Cronje P.M., Celliers P.J., Fenemore R E., Carstens J.W., Kriel J.E., Nel W.A.G., Burger S.J., Van Rooyen D.M., Weehuizen H.F., Rohwer P., Cornell J.C., Jungwirth H.N. and Molteno P.G. (1991). Operation and development of the NAC accelerator facilities. In: Proceedings of the Twelfth International Conference on Cyclotrons and their Applications (B. Martin and K Ziegler, Eds.) Springer, Berlin, pp 80–83.

Booz J. and Fidorra J. (1981). Microdosimetric investigations on collimated fast neutron beams for radiation therapy: II. The problem of radiation quality and RBE. Phys. Med. Biol. **26** (1), 43–45.

Brenner D.J. (1983). Neutron kerma values above 15 MeV calculated with a nuclear model applicable to light nuclei. Phys. Med. Biol. **29** (4), 437–441.

Broerse J.J., Barendsen G.W. and Kersen G.R. (1968). Survival of cultured human cells after irradiation with fast neutrons of different energies in hypoxic and oxygenated conditions. Int. J. Radiat. Biol. **13**, 559–572.

Broerse J.J., Mijnheer B.J. and Williams J.R. (1981). European protocol for neutron dosimetry for external beam therapy. Brit. J. Radiol. **54**, 882–898.

Budach V. (1991). The role of fast neutrons in radio–oncology – A critical appraisal. Strahlenther. Onkol. **167**, 677–692.

Bühler G., Menzel H.G., Schuhmacher H., Dietze G. and Guldbakke S. (1986). Neutron kerma factors for magnesium and aluminium measured with low pressure proportional counters. Phys. Med. Biol. **31** (6), 601–611.

Burger G., Maier. E and Morhart A (1978). Radiation quality and its relevance in neutron radiotherapy. In: Proceedings of the Sixth Symposium on Microdosimetry J. Booz and H.G. Ebert Eds.) CEC, Brussels, pp 451–468.

Caswell R.S., Coyne J.J. and Randolph M.L. (1980). Kerma factors for neutron energies below 30 MeV. Radiat. Res. **83**, 217–54.

Caswell R.S., Coyne J.J., Gerstenberg H.M. and Axton E.J. (1988). Basic data necessary for neutron dosimetry. Radiat. Prot. Dosim. **23**, 11–17.

Catterall M. (1974a). The treatment of advanced cancer by Fast Neutrons from the Medical Research Council's Cyclotron at Hammersmith Hospital, London. Europ. J. Cancer **10**, 343–347.

Catterall M. (1974b). A report on three years' fast neutron therapy from the Medical Research Council's Cyclotron at Hammersmith Hospital, London. Cancer **34**, 91–95.

Chase R.L., (1968). Pulse timing system for use with gamma rays in Ge(Li) detectors. Rev. Sci. Instrum. **39**, 1318–1326.

Cornell J.C., Lloyd G.C.W. and Fourie D.T. (1991). A neutron beam facility at NAC. In: Proceedings of the Twelfth International Conference on Cyclotrons and their Applications (B. Martin and K Ziegler, Eds.) Springer, Berlin, pp 594–597.

DeLuca P.M. Jr., Barschall H.H., Haight R.C. and McDonald J.C. (1984). Kerma factor of carbon for 14.1 MeV neutrons. Rad. Res. **100**, 78–86.

DeLuca P.M. Jr., Barschall H.H., Burhoe M. and Haight R.C. (1986). Carbon kerma factor for 18– and 20–MeV Neutrons. Nucl. Sci. Eng. **94(2)**, 192–198.

Del Guerra A. (1976). A compilation of n–p and n–C cross sections and their use in a Monte Carlo program to calculate the neutron detection efficiency in a plastic scintillator in the energy range 1–300 MeV. Nucl Inst. Meth. **135**, 337–352.

Dicello J.F. (1983). The contribution of secondary electrons to radiation fields produced by pion beams. In: Proceedings of the Eighth Symposium on Microdosimetry (J Booz and H G Ebert, Eds.) CEC, Brussels, pp 223–230.

Dimbylow P.J. (1982). Neutron cross–section and kerma value calculations for C, N, O, Mg, Al, P, S, Ar and Ca from 20 to 50 MeV. Phys. Med. Biol. **27** (8), 989–1001.

Duncan W., Arnot S.J., Batterman J.J., Orr J.A., Schmitt G. and Kerr G.R. (1984). Fast neutrons in the treatment of head and neck cancers: The results of a multi–centre randomly controlled trial. Radiother. Oncol. **2**, 293–300.

Duncan W., Arnott S.J., MacDougall R.H., Quilty P.M., Rodger A., Kerr G.E. and Williams J.R. (1985). A report of a randomized trial of d(15)+Be neutron compared with megavoltage X–ray therapy of bladder cancer. Int. J. Radiat. Oncol. Biol. Phys. **11**, 2043–2049.

Du Toit Z.B., Celliers P.J., Roels L.M.M., Conard, E.P., Kritzinger J.J. and Burger S.J. (1987). Operating experience with the light–ion injector of the NAC. In: Proceedings of the Eleventh International Conference on Cyclotrons and their Applications (M. Sekiguchi, Y. Yano and K. Hatanaka Eds.) Ionics, Tokyo, pp 109–112.

Fidorra J., Poli A. and Booz J. (1981). Experimental microdosimetric spectra and parameters of collimated fast neutron beams in a water phantom for different field sizes. In: Proceedings of the Seventh Symposium on Microdosimetry (J Booz, H G Ebert and H D Hartfiel, Eds.) CEC, Brussels, pp 1169–1179.

Fidorra J. and Booz J. (1981). Microdosimetric investigations on collimated fast–neutron beams for radiation therapy: I. Measurements of microdosimetric spectra and particle dose fractions in a water phantom for fast neutrons from 14 MeV deuterons on beryllium. Phys. Med. Biol. **26** (1), 27–41.

Field S.B. and Joiner M.C. (1990). Expression of dose in neutron therapy. Radiother. Oncol. **17**, 73–80.

Fleming R.F. (1974). Energy transfer to hydrogen by neutrons up to 30 MeV. Radiat. Res. **60**, 347–349.

Goodhead D.T. (1982). An assessment of the role of microdosimetry in radiobiology. Radiat. Res. **9**, 45–76.

Goodhead D.T., Charlton D.E., Wilson W.E. and Paretzke H.G. (1985). Current biophysical approaches to the understanding of biological effects of radiation in terms of local energy deposition. In: Proceedings of the Fifth Symposium on Neutron Dosimetry (H. Schraube, G. Burger and J. Booz, Eds.) CEC, Brussels, 57–68.

Goodman L.J. and Coyne J.J.(1980). W_n and neutron kerma for methane based tissue equivalent gas. Radiat. Res. **82**, 13–26.

Hall E.J., Withers H.R., Geraci J.P., Meyn R.E., Rasey J., Todd P. and Sheline G.E. (1979). Radiobiological intercomparison of fast neutron beams used in therapy. Strahlenther. Onkol. **165**, 263–267.

Hall E.J., Zaider M., Bird R. and Astor M. (1982) Radiobiological studies with therapeutic neutron beams generated by p⁺¬Be or d⁺¬Be. Brit. J. Radiol. **55**, 640–644.

Hall E.J., Astor. M and Brenner D.J. (1992). Biological intercomparisons of neutron beams used for radiotherapy generated by p⁺ ¬ Be in hospital based cyclotrons. Brit. J. Radiol. **65**, 66–71.

Hartman G., Menzel H.G., Schuhmacher H., Höver K.H. and Granzow G. (1981). Radiobiological intercomparison of two fast neutron therapy units using CHO cell survival and its correlation to microdosimetry. In: Proceedings of the Seventh Symposium on Microdosimetry (J. Booz, H.G. Ebert and H.D. Hartfiel, Eds.) CEC, Brussels, pp 1181–1190.

Heintz P.H., Johnsen S.W. and Peek N.F. (1977). Neutron energy spectra and dose–distribution spectra of cyclotron–produced neutron beams. Med. Phys. **4** (3), 250–254.

Hill C.K., Ten Haken R.K. and Awshalom M. (1991). The lethal effects of Fermilab fast neutrons vary with the depth of cells in a water phantom. Int. J. Radiat. Oncol. Biol. Phys. **20**, 1341–1345.

Hogeweg B., Zoetelief J. and Broerse J.J. (1978). RBE for cell survival at different positions in collimated neutron beams in relation to differences in lineal energy spectra. In: Proceedings of the Sixth Symposium on Microdosimetry (J. Booz and H.G. Ebert Eds.) CEC, Brussels, pp 507–516.

Hornsey S., Myers R., Parnel C.J., Bonnett D.E., Blake S.W. and Bewley D.K. (1988). Changes in relative biological effectiveness with depth of the Clatterbridge neutron therapy beam. Brit. J. Radiol. **61**, 1058–1062.

Hough J.H. and Binns P.J. (1990). Radiation quality in the penumbral region of neutron therapy beams. In: Proceedings of the International Heavy Particle Therapy Workshop (PTCOG/EORTC/ECNEU), Villigen PSI, September 1989. Paul Scherrer Institute Report 69, pp. 105–107.

ICRU, Report 26 (1977). Neutron dosimetry for biology and medicine. International Commission on Radiation Units and Measurements, Bethesda, MD, USA.

ICRU Report 29 (1978). Dose specification for reporting external beam therapy with photons and electrons. International Commission on Radiation Units and Measurements, Bethesda, MD, USA.

ICRU Report 33 (1980). Radiation quantities and units. International Commission on Radiation Units and Measurements, Bethesda, MD, USA.

ICRU, Report 36 (1983). Microdosimetry. International Commission on Radiation Units and Measurements, Bethesda, MD, USA.

ICRU, Report 45 (1989). Clinical neutron dosimetry. Part 1: Determination of absorbed dose in a patient treated by external beams of fast neutrons. International Commission on Radiation Units and Measurements, Bethesda, MD, USA.

Jones D.T.L., Yudelev M. and Hendrikse W.L.J. (1988). Physical characteristics of the South African high energy neutron therapy facility. Radiat. Prot. Dosim. **23**, 365–368.

Jones D.T.L. and Yudelev M. (1988). The effects of various filters on a p(66)/Be neutron beam. In: Proceedings of the World Congress on Medical Physics and Biomedical Engineering (J.W. Clark, P.I. Horner, A.R. Smith and K. Strum Eds.) Phys. Med. Biol. **33** (Supplement I) pp 133.

Kellerer A.M. (1971). An assessment of wall effects in microdosimetric measurements. Radiat. Res. **47**, 377–386.

Kellerer A.M. and Rossi H.H. (1972). The theory of dual radiation action. Curr. Top. Radiat. Res. Q. **8**, 85–158.

Kellerer A.M. and Chmelevsky D. (1975). Criteria for the applicability of LET. Radiat. Res. **63**, 226–234.

Kellerer A.M. and Rassow J. (1980). The correction for the gamma–ray component in neutron therapy Med. Phys. **7** (5), 503–506.

Kellerer, A.M. (1981). Criteria for the equivalence of spherical and cylindrical proportional counters in microdosimetry. Rad. Res. **86**, 277–286.

Kliauga P., Horton J. and Stafford P. (1989). Microdosimetry of a 42 MeV therapy beam. Int. J. Radiat. Oncol. Biol. Phys. **16**, 845–848.

Knoll G.F. (1979). Radiation detection and measurement. John Wiley and Sons, New York, USA.

Kritzinger J.J., Fenemore R.E.F. and Van Niekerk M.J. (1991). Performance of the NAC RF systems. In: Proceedings of the Twelfth International Conference on Cyclotrons and their Applications (B. Martin and K Ziegler Eds.) Springer, Berlin, pp 208–211.

Marquardt D.W. (1963). An algorithm for least–squares estimation of nonlinear parameters. J. Soc. Indust. Appl. Math. **11** (2), 431–441.

Menzel H.H. and Waker A.J. (1976). Gamma dose contributions derived from energy deposition spectra. In: Monograph on Basic Physical Data for Neutron Dosimetry (J J Broerse, Ed.) CEC, Luxembourg, pp 179–184.

Menzel H.G. (1984). Proportional counter measurements in neutron beams. In: Advances in dosimetry for fast neutrons and heavy charged particles for therapy applications. IAEA, Vienna, pp 102–126.

Menzel H.G., Bühler G., Schuhmacher H., Muth G., Dietze G. and Guldbakke S. (1984). Ionisation distributions and A–150 plastic kerma for neutrons between 13.9 and 19 MeV measured with a low pressure proportional counter. Phys. Med. Biol. **29** (12), 1537–1554.

Menzel H.G., Pihet P., Folkerts K.H., Dahmen P. and Grillmaier R.E. (1988). Dosimetry research using low pressure proportional counters for neutrons with energies up to 60 MeV. Radiat. Prot. Dosim. **23**, 389–392.

Menzel H.G., Pihet P. and Wambersie A. (1990). Microdosimetric specification of radiation quality in neutron radiation therapy. Int. J. Biol. **57**, 865–883.

Mijnheer B.J., Battermann J.J. and Wambersie A. (1987a). What degree of accuracy is required and can be achieved in photon and neutron therapy? Radiother. Oncol. **8**, 237–252.

Mijnheer B.J., Wootton P., Williams J.R., Eenmaa J. and Parnell C.J. (1987b). Uniformity in dosimetry protocols for therapeutic applications of fast neutron beams. Med. Phys. **14** (6), 1020–1026.

Milan J. and Bentley R.E. (1974). The storage and manipulation of radiation dose data in a small digital computer. Brit. J. Radiol. **47**, 113–121.

Oliver G.D., Quam W.M. and Wilde W.O. (1972). Empirical dose quality distributions of californium–252. Health Phys. **22**, 341–349.

O'Neill J. and Laughlin J.S. (1975). A biological determination of the variation of fast neutron field quality with depth, RBE and OER. Radiat. Res. **63**, 211–225.

Pihet P., Gueulette J., Menzel H.G., Grillmaier R.E. and Wambersie A. (1988). Use of microdosimetric data of clinical relevance in neutron therapy planning. Radiat. Proc. Dosim. **23**, 471–474.

Pihet P. (1989). Etude microdismetrique de faisceaux de neutrons de haute energie. Applications dosimetriques et radiobiologiques, Thesis (Louvain–la–Neuve: Universite Catholique de Louvain).

Pihet P. and Menzel H.G. (1989). Atomic and molecular data for radiotherapy. IAEA–TECDOC–506, Vienna, pp 102–126.

Pihet P., Menzel H.G., Schmidt R., Beauduin M. and Wambersie A. (1990a). Biological weighting function for RBE specification of neutron therapy beams. Intercomparison of 9 European centres. Radiat. Prot. Dosim. **31**, 437–442.

Pihet P., Menzel H.G., Wambersie A. and Grillmaier R.E. (1990b). Specification of radiation quality for high–LET particle therapy – Microdosimetric approach. In: The 2nd European Particle Accelerator Conference (P Marin and M Mandrillon, Eds.) Editions Frontières, France, pp538–539.

Pihet P., Gerdung S., Grillmaier R.E., Kunz A. and Menzel H.G. (1992a). Critical assessment of calibration techniques for low pressure proportional counters used in radiation dosimetry. Radiat. Prot. Dosim. **44**, 115–120.

Pihet P., Guldbakke S., Menzel H.G. and Schuhmacher H. (1992b). Measurement of kerma factors for carbon and A–150 plastic: neutron energies from 13.9 to 20.0 MeV. Phys. Med. Biol. **37** (10), 1957–1975.

Pilcher J.V. (1989). Coincident Proton Decay of the Continuum Induced by 200 MeV Protons on ^{12}C. Ph.D Thesis, University of Cape Town.

Posny F., Chary J. and Nguyen V.D. (1987). $\overline{W}$ values for heavy particles in propane and in TE gas. Phys. Med. Biol. **32** (4), 509–515.

Randers–Pehrson G., Finlay R.W., Dicello J.F. and McDonald J.C. (1982). A technique for time–resolved microdosimetric spectroscopy. In: Proceedings of the Eighth Symposium on Microdosimetry (J Booz and H G Ebert, Eds.) CEC, Brussels, pp 1169–1177.

Rassow J., Baumhoer W., Olthoff K., and Bamberg M. (1990). Treatment planning for neutron therapy of high–grade astrocytomas and pencil gliomas. Radiother. Oncol. **19**, 179–185.

Romero J.L., Brady F.P. and Subramanian T.S. (1985). Neutron induced charged particle spectra and kerma from 25 to 60 MeV. Proc. Int. Conf. on Nuclear Data for Basic and Applied Science. Gordon and Breach Science Publishers. Santa Fe, New Mexico, pp 687–99.

Rossi H.H. and Rosenzweig W. (1955a). A device for the measurement of dose as a function of specific ionization. Radiology **64**, 404–411.

Rossi H.H. and Rosenzweig W. (1955b). Measurements of neutron dose as a function of linear energy transfer. Radiat. Res. **2**, 417–425.

Rossi H.H. (1968). Microscopic energy distribution in irradiated matter. In: Radiation dosimetry Volume I, Fundamentals. (F.H. Attix, W.C. Roesch and E. Tochilin, Eds.) Academic Press, New York, USA.

Schmidt R. and Hess A. (1988). Component evaluation of event size spectra for a clinical 14 MeV neutron beam. Med. Phys. **15** (3), 343–347.

Schrewe U.J., Brede H.J. and Dietze G. (1988a). Investigation of tissue–equivalent proportional counters in mixed neutron–photon fields also applying time–of–flight techniques. Radiat. Dosim. Prot. **23**, 239–243.

Schrewe U.J., Brede H.J., Pihet P and Menzel H.G. (1988b). On the calibration of tissue equivalent proportional counters with built–in α particle sources. Radiat. Prot. Dos. **23** 249–252.

Schrewe U.J., Brede H.J. and Dietze G. (1989). Dosimetry in mixed neutron–photon fields with tissue–equivalent proportional counters. Radiat. Dosim. Prot. **29**, 41–45.

Schrewe U.J., Brede H.J., Langner F. and Schuhmacher H. (1990). The use of microdosimetric detectors combined with time–of–flight techniques. Nucl. Inst. Meth. **A299**, 226–230.

Schrewe U.J., Brede H.J., Gerdung S., Nolte R., Pihet P., Schmelzbach P. and Schuhmacher H. (1992a). Determination of kerma factors of A–150 plastic and carbon at neutron energies between 45 and 66 MeV. Radiat. Prot. Dosim. **44**, 21–24.

Schrewe U.J., de Aro A.C.A., Brede H.J., Dangendorf V., DeLuca P.M. Jr., Gerdung S., Lim T., Newhauser W., Nolte R., Schmelzbach P., Schuhmacher H. and Scott M.C. (1992b). Ionization yield spectra in nitrogen and oxygen for neutron energies of 17 MeV, 45 MeV and 66 MeV. Presented at The Eleventh Symposium on Microdosimetry, 13–18 September, 1992, Gatlinburg, Tenessee, USA.

Schuhmacher H., Brede H.J., Henneck R., Kunz A., Meulders J.P., Pihet P. and Schrewe U.J. (1992). Measurement of neutron kerma factors for carbon and A–150 plastic at neutron energies of 26.3 and 37.8 MeV. Phys. Med. Biol. **37** (6), 1265–1281.

Slabbert J.P., Binns P.J., Jones H.L. and Hough J.H. (1989). A quality assessment of the effects of a hydrogenous filter on a p(66)Be(40) neutron beam. Brit. J. Radiol. **62**, 989–994.

Slabbert J.P., Hough J.H., Jones H.L., Schreuder A.N. and Jones D.T.L. (1991). Cellular damage in response to variations in the secondary charged–particle spectrum of a p(66)/Be neutron beam. National Accelerator Centre Report (NAC/AR/91–01), pp 99.

Smathers J.B., Otte V.A., Smith A.R., Almond P.R., Attix F.J., Spokas J.J., Quam W.M., Goodman L.F. (1977). Composition of A150 tissue equivalent plastic. Med. Phys. **4**, 74–77.

Srdoc D. (1970). Experimental technique of measurement of microscopic energy distribution in irradiated matter using Rossi counters. Radiat. Res. **43**, 302–319.

Stafford P., Horton J.L. and Almond P.R. (1987). A microdosimetric characterization of a cyclotron–produced therapeutic neutron beam. Med. Phys. **14**, 1015–1019.

Stinchcomb T.G., Kuchner F.T. and Skaggs L.S. (1980). Comparison of the microdosimetric event size–method and twin–chamber method of separating dose into neutron and gamma components. Phys. Med. Biol. **25**, 51–64.

Stinchcomb T.G., Kuchnir F.T., Myrianthopoulos L.C., Horton J.L. and Roberts W.K. (1986). Correlation of microdosimetric measurements with relative biological effectiveness from clinical experience for two neutron therapy beams. Med. Phys. **13**, 201–206.

Stone R.S. (1948). Neutron therapy and specific ionization. Am. J. Roentgol. **59**, 771–785.

Svensson H. (1984). Quality assurance in radiation therapy: Physical Aspects. Int. J. Radiat. Oncol. Biol. Phys. **10**, (Suppl.) 59–65.

Taylor G.C., Scott M.C. and Fletcher J.G. (1990). Microdosimetric measurements on the Clatterbridge neutron cancer therapy cyclotron. Radiat. Prot. Dosim. **31**, 443–447.

Vynckier S., Vanneste F., Richard F. and Wambersie A. (1988). Treatment planning for neutron therapy. Radiat. Proc. Dosim. **23**, 463–469.

Waibel E. and Willems G. (1987). Stopping power and ranges of low–energy protons in tissue–equivalent gas. Phys. Med. Biol. **32** (3), 365–370.

Waker A.J. (1985). Experimental uncertainties in microdosimetric measurements and an examination of the performance of three commercially produced proportional counters. Nucl. Instru. and Meth. **A234**, 354–360.

Wambersie A. and Gueulette J. (1984). Accuracy required in radiotherapy and in neutron therapy. In: Advances in dosimetry for neutrons and heavy charged particles for therapy applications, Vienna 1982. IAEA, Vienna, pp 11–26.

Wambersie A. and Battermann J.J.(1987). Practical problems related to RBE in neutron therapy. In: Progress in Radio–Oncology III (K.H.Kärcher, H.D. Kogelnik and T. Szeipesi, Eds.) Vienna, ICRO, pp 155–162.

Wambersie A. (1990). Fast neutron therapy at the end of 1988 – a summary of clinical data. Strahlenther. Onkol. **166**, 52–60.

Wambersie A and Mijnheer B.J. (1990). Expression of dose in neutron therapy. Radiother. Oncol. **17**, 261–266

Wambersie A., Pihet P. and Menzel H.G. (1990). The role of microdosimetry in radiotherapy. Radiat. Proc. Dosim. **31**, 421–432.

Weaver K., Bichsel H., Eenmaa J. and Wootton P. (1977). Measurement of photon dose fraction in a neutron radiotherapy beam. Med. Phys. **4**, 379–386.

White R.M., Broerse J.J., DeLuca P.M. Jr., Dietze G., Haight R.C., Kawashima K., Menzel H.G., Olsson N. and Wambersie A. (1992). Status of nuclear data for use in neutron therapy. Radiat. Prot. Dosim. **44**, 11–20.

Wuu C.S. and Milavickas L.R. (1987). Determination of the kerma factors in tissue–equivalent plastic, C, M and Fe for 14.7 MeV neutrons. Med. Phys. **14** (6), 1007–1014.

Zeitz L., Canada T.R., Djordjevic B., Dymbort G, Freeman R., McDonald J.C., O'Neill J. and Laughlin J.S. (1975). A biological determination of the variation of fast neutron field quality with depth, RBE and OER. Radiat. Res. **63**, 211–225.